Patient-Derived Induced Pluripotent Stem Cell Models for Drug Identification in *SCN2A*-Related Epilepsy

Ji Hun Kim

The Graduate School
Yonsei University
Department of Medicine

Patient-Derived Induced Pluripotent Stem Cell Models for Drug Identification in *SCN2A*-Related Epilepsy

A Dissertation Submitted
to the Department of Medicine
and the Graduate School of Yonsei University
in partial fulfillment of the
requirements for the degree of
Doctor of Philosophy in Medical Science

Ji Hun Kim

December 2024

This certifies that the Dissertation of Ji Hun Kim is approved

Thesis Supervisor	Hoon-Chul Kang
Thesis Committee Member	Chul Hoon Kim
Thesis Committee Member	Se Hoon Kim
Thesis Committee Member	Hyong Bum Kim
Thesis Committee Member	Eun Ji Cheong

The Graduate School
Yonsei University
December 2024

ACKNOWLEDGEMENTS

"Your beginnings will seem humble, so prosperous will your future be. - Job 8:7"

During my time at Yonsei University Graduate School, and the 10 years I spent studying at the Department of Pediatric Neurology at Severance Hospital before that, I have had the privilege of learning and growing immensely. None of this would have been possible without the support and guidance of so many people, and I would like to take this opportunity to express my deepest gratitude to all of them.

First and foremost, I would like to extend my heartfelt thanks to Professor Kang Hoon-Chul, who has guided me throughout my graduate studies. Whenever I felt lost or inadequate, Professor Kang Hoon-Chul's invaluable advice and mentorship kept me on track, and it is because of his unwavering support that I was able to persevere through the many challenges I faced. I truly believe that I would not have been able to complete this thesis without his guidance. Thank you, Professor Kang Hoon-Chul, for always investing in my growth and success. I would also like to express my sincere gratitude to my family, who have supported and waited for me patiently throughout my academic journey. My father(Kim Hyung-Joon), my mother(Cho Soon-Ok), and my brothers, Kim Sang-Hoon and Kim Jung-Hoon, have always stood by my side, offering encouragement when I needed it most. Their faith in me gave me the strength to keep going, and I am incredibly grateful for their love and support. Thanks to the support, encouragement, and love of my family, I was able to successfully complete my academic journey. Having them as my family is the greatest blessing in my life, and I will carry my deep gratitude and love for my father, mother, and my two younger brothers with me always. Furthermore, I would like to extend my thanks to all the professors, colleagues, and staff members who have helped me along the way. First and foremost, Professor Kim Heung Dong (I am deeply honored to have experienced your kindness and to have accompanied you through the latter part of your distinguished journey), Professor Lee Joon Soo, Professor Kim Se-hee, Teacher Ko Ara, Teacher Na Ji-hoon, Teacher Koo Cheong-mo, Teacher Youn Song Ee (I am thankful for having been able to share the final stage of my journey with you), and the nurses (Lee Min Jeong, Ryu Seon Ae, Kim Na Hyun, and the nurses of Ward 37), and the PhD students in our lab, including PhD. Zhejiu Quan, PhD. Kim Hyunwoo, PhD. Hong Eunhwa, and Yoo Seonggon, Oh Hae-Joo, Shin Hee-Jin, and Lee Sang-Bo, Kang Jeong-In have all played a significant role in my research journey. Their collaboration, insights, and encouragement helped me overcome numerous challenges, and for that, I am deeply grateful. I would also like to express my sincere gratitude to Professor Kim Dae-Sung from Korea University and the members of his lab, Yeon Kyu-Beom, Yoo Seo-Hyun, Kim Dong-Yoon, Oh Seung-Soo, and Lee Chan-Young, for their invaluable support. My heartfelt thanks go out to my university friends from the PCR team: Jeong Jin-Hwa, Heo Jeong-Hyun, Shin Sang-Hoon, Kim Seok-Jin, Lee Sang-Hoon, Moon Jin-Woo, Byun Boo-Kyung, and Shin Jeong-Soo. I also want to thank my middle school friends—Kim Jong-Gyu, Song Ki-Hoon, Shim Yoon-Seok, Lee Hong-Gi, and Choi Hyung-Seok—and my high school friends—Min Sang-Woo, Park Sun-Young, Yoo Soo-Ho(K-Haaland), Shin In-Chul, Lee Choong-Hwan, Kim Young-Sik, and Lee Sang-Won, Lee Seung-Hoon—for their unwavering support and encouragement. Additionally, I extend my gratitude to You Young-Rang, Hong Won-Jun, Lim Hun, Hui-Wen Liu, Choi Seo-

Jin(Kate), Jin Sol, Lee Sohyoung, Park Sungwoo, Han Hye-Rim, Kim Jung-Yeop, Kim Song-Kang and Lee Jin-Woo for their care and kindness. My thanks also go to all the students from Ewha Womans University(Thank you to Professor Kim Jaesang and the students in Professor Kim Jaesang's lab Lee Sebin. Sung Seoyoung). Thank you to my friends from the Yonsei University fencing team as well. Thank you so much to Professor Kim Hyungbum and the students in Professor Kim Hyungbum's lab, as well as to Professor Cho Seungwoo and the students in Professor Cho Seungwoo's lab. I am especially thankful to my university colleagues Park No-Eul, Son Kwan-Cheol, Son Seung-Beom, Yeo Chang-Hyun, Oh Se-Hee, Lee Byung-Hoon, Lee Yeong-Rok, and Kang Jung-Won, with whom I studied and collaborated during my undergraduate years. I would like to express my heartfelt gratitude to Lim Hyun-Tae, my close friend, whose music has been a constant source of strength and inspiration to me. Lastly, I would also like to express my heartfelt gratitude to my church friends and everyone at the church for their support and encouragement. I give infinite glory to God. Thank you all from the bottom of my heart. I am sincerely thankful for all of his help in enabling me to graduate. In addition, I want to thank my middle and high school friends, as well as everyone who has been a source of strength throughout this journey. A special note of thanks goes to Professor Na Dokyun from Chung-Ang University, whose support was instrumental in helping me complete my graduate studies. Professor Na Dokyun’s guidance, both academically and in terms of practical research advice, was crucial to my progress. His encouragement and collaboration allowed me to gain new perspectives and finish my research successfully. Each of you has supported me in your own way, and I appreciate the care and kindness you've shown me over the years.

Lastly, I wish to express my deepest gratitude, love, and apology to my future wife, Hong Min-Ah. Despite the long hours and time apart due to my studies and research, you have always stood by me with patience and understanding. My love, Hong Min-Ah, it was because of you that I was able to overcome the most difficult times in my life. Meeting you gave me the strength and support I needed to complete this thesis. Your love and unwavering support have been my anchor, and for that, I am eternally grateful. I dedicate this thesis to you, as it contains all the gratitude and love I have for you. Once again, I would like to thank everyone who has supported me throughout my graduate journey.

My favorite football team, Liverpool FC, has the iconic motto "You'll Never Walk Alone." This powerful phrase resonates deeply with me. I have always walked my journey not alone but together with others, which has given me the strength to complete it to the very end. I dedicate all this glory to everyone I love.

Charity suffereth long, and is kind; charity envieth not; charity vaunteth not itself, is not puffed up; doth not behave itself unseemly, seeketh not her own, is not easily provoked, thinketh no evil; rejoiceth not in iniquity, but rejoiceth in the truth; beareth all things, believeth all things, hopeth all things, endureth all things. -Corinthians 13:4-7-

Sincerely,

Ji Hun Kim

TABLE OF CONTENTS

LIST OF FIGURES

LIST OF TABLES

ABSTRACT

Patient-Derived Induced Pluripotent Stem Cell Models for Drug Identification in *SCN2A*-Related Epilepsy

SCN2A-related epilepsy is a severe neurological disorder caused by mutations in the *SCN2A* gene, which encodes NaV1.2 voltage-gated sodium channels. These mutations lead to neuronal hyperexcitability, resulting in diverse neurodevelopmental disorders such as epilepsy, intellectual disabilities, and autism spectrum disorders. Due to the variability in clinical symptoms, understanding the pathological mechanisms of *SCN2A*-related epilepsy is critical for developing targeted therapies. In this study, patient-derived induced pluripotent stem cells (iPSCs) were generated from peripheral blood mononuclear cells (PBMCs) to model *SCN2A*-related epilepsy and investigate its cellular and molecular characteristics. Using CRISPR/Cas9 gene-editing technology, *SCN2A* mutations were corrected, enabling direct comparisons of physiological and molecular properties between mutated and corrected neurons.

Electrophysiological analyses, including micro-electrode array (MEA) recordings, revealed that *SCN2A* mutations significantly increased neuronal firing rates and caused disruptions in network synchronization, which are key contributors to hyperexcitability. To identify potential therapeutic interventions, high-throughput drug screening was performed on patient-specific neurons, focusing on sodium channel blockers. Among the tested compounds, phenytoin, a widely used sodium channel blocker, validated the experimental model by demonstrating dose-dependent reductions in hyperexcitability. Additionally, five candidate compounds were evaluated, with several exhibiting enhanced efficacy at lower concentrations compared to phenytoin.

This study presents a robust platform for modeling *SCN2A*-related epilepsy, integrating patient-derived iPSC models, CRISPR/Cas9 gene editing, and advanced electrophysiological techniques. By combining high-throughput drug screening with computational drug discovery approaches, the research highlights promising pathways for personalized treatments targeting the specific molecular mechanisms of *SCN2A* mutations. These findings provide critical insights into the pathophysiology of *SCN2A*-related epilepsy and pave the way for future validation of these compounds in preclinical and clinical settings, advancing the development of precision medicine for drug-resistant epilepsy.

Key words : *SCN2A* mutation, epilepsy, neurodevelopmental disorders, induced pluripotent stem cells (iPSCs), CRISPR/Cas9, gene-editing, sodium channel blocker, electrophysiology, drug screening, precision medicine

1. Introduction

Epilepsy is broadly defined as a neurological disorder characterized by recurrent, unprovoked seizures. According to the International League Against Epilepsy (ILAE), a diagnosis of epilepsy is made when an individual experiences two or more unprovoked seizures within 24 hours.[1-5] The hallmark feature of epilepsy is the recurrent, abnormal neuronal activity that manifests as seizures, which can vary widely in their presentation and impact. Seizures are caused by excessive, synchronized electrical discharges in the brain, leading to temporary dysfunction of neural circuits.[6] These seizures are classified based on their onset into focal seizures (arising from one hemisphere), generalized seizures (affecting both hemispheres simultaneously), or seizures of unknown etiology.[7,8] globally, epilepsy affects approximately 0.5-1% of the population, making it one of the most common chronic neurological conditions.[9] In Korea alone, more than 500,000 individuals are estimated to suffer from epilepsy, with a significant proportion being children and adolescents.[10,11] Despite the availability of around 30 antiepileptic drugs (AEDs), 30-40% of patients continue to experience drug-resistant epilepsy, underscoring the need for new therapeutic strategies. The primary aim of current epilepsy treatments is symptomatic relief rather than targeting the underlying pathology. While many cases of epilepsy are idiopathic (without a clear cause), others are symptomatic, resulting from identifiable brain abnormalities or genetic mutations. There are many factors that cause epilepsy, which can be divided into idiopathic and symptomatic categories. Genetic mutations are known to contribute to the development of epilepsy, often leading to brain malformations and other genetic abnormalities.[12,13]

Among the more than 40 known types of epilepsy[3], several are linked to specific genetic mutations, indicating that genetic factors play a critical role in the pathogenesis of idiopathic epilepsy.[3,14] Historically, these mutations were identified using Sanger sequencing, a method that, while reliable, was time-consuming and lacked the resolution needed to uncover subtle genetic variations.[15,16] However, advancements in genomic technologies, particularly Next Generation Sequencing (NGS), have enabled more precise identification of mutations associated with epilepsy, especially in patients with drug-resistant forms or accompanying neurodevelopmental disorders.[15-17] Whole Exome Sequencing (WES) has further enhanced the ability to detect rare and novel genetic variants, shedding light on the complex genetic landscape of epilepsy.

Voltage-gated sodium channels (VGSCs) are major ion channels involving both excitatory and inhibitory neurons and have an important role in generating and transmitting neuronal activity.[18-21] They have been found to accompany various types of epilepsy, including 'generalized epilepsy with febrile seizures plus (GEFS+)' and 'severe myoclonic epilepsy of infancy (SMEI)'.[22] The voltage-gated sodium channel alpha subunit is encoded by a tissue-specific gene family, *SCN1A* to *SCN11A*, located on four paralogous chromosome segments.[23] Among them, *SCN2A* encodes the Voltage-

Gated Sodium Channel Subunit 1.2 (Nav 1.2), and mutations in this gene are known to cause epilepsy spectrum or neurodevelopmental disorders.[21]

Mutations in *SCN2A*, encoding the Voltage-Gated Sodium Channel Subunit 1.2 (Nav 1.2), are linked to a wide range of epilepsy phenotypes and neurodevelopmental disorders.[19,21,24-31] initially associated with benign familial neonatal and infantile seizures (BFNIS), these mutations have also been identified in severe encephalopathies such as Epilepsy of Infancy with Migratory Focal Seizures (EIMFS), Otahara syndrome, and West Syndrome.[19,21,24-31] Additionally, *SCN2A* mutations have been found in patients with intellectual disability and autistic features without epilepsy, suggesting its role in autism spectrum disorders.[19,21-39] the type of mutation often correlates with seizure onset age. Missense mutations are typically linked to early-onset epilepsy (<3 months), causing benign seizures, while truncation mutations are more common in late-onset epilepsy (≥3 months), often associated with intractable epilepsies.[21] This age-dependent variation significantly influences both clinical severity and drug responsiveness, making mutation type a critical factor in tailoring treatment strategies.[21] *SCN2A* mutations are also implicated in benign infantile seizures, autism spectrum disorder/intellectual disability (ASD/ID), childhood-onset epileptic encephalopathy, schizophrenia, and other neurodevelopmental conditions such as ataxia and hypotonia.[21,24,27,30,32-39]

Mutations in the *SCN2A* gene are associated with idiopathic epilepsy and various neurological disorders, showing significant variability in clinical outcomes and drug responses. Identical mutations can lead to different effects depending on individual pathological characteristics. For example, medications effective in early-onset epilepsy (< 3 months) may worsen symptoms or be ineffective in late-onset cases (≥3 months).[21] This highlights the necessity of constructing personalized models to study *SCN2A*-related mechanisms and develop tailored therapies.

To address this, this study focuses on generating induced Pluripotent Stem Cells (iPSCs) from patients with *SCN2A* mutations. These iPSCs are reprogrammed from patient-derived fibroblasts or monocytes using Oct4, Sox2, c-MYc, and Klf4 transcription factors, based on well-established heterozygous germline mutations.[40,41] The iPSCs are then differentiated into GABAergic and glutamatergic neurons—key neuronal types involved in epilepsy—through optimized culture environments.[42-48] These neurons serve as a platform for analyzing *SCN2A* mutations' effects on seizure pathways and neuronal channel activity, using electrophysiological studies with inhibitors such as 4-AP, TTX, CNQX, and gabazine.[49,50]

SCN2A is predominantly expressed in the central nervous system, particularly in excitatory pyramidal neurons, and is absent in peripheral tissues.[39] During early development, *SCN2A* is the sole sodium channel homolog expressed in the Axon Initial Segment (AIS), a critical site for action potential initiation near the soma.[51-53] As neurons mature, *SCN2A* transitions to the terminal AIS, maintaining its essential role in excitatory signaling. These functional transitions provide valuable insights into *SCN2A*-related disorders and support innovative therapeutic strategies.[54] Furthermore,

SCN2A is co-expressed with SCN8A in excitatory glutamatergic neurons, whereas *SCN1A* predominates in inhibitory interneurons, highlighting *SCN2A*'s distinct functional role in neuronal networks.[32,55-57]

By integrating iPSC technology and advanced electrophysiological methods, this study aims to create patient-specific models to investigate *SCN2A* pathologies. These models will facilitate the analysis of *SCN2A* mutations' effects on neuronal activity and contribute to personalized treatment strategies, including drug screening and targeted therapies.[54]

In this study, I focus on generating induced Pluripotent Stem Cells (iPSCs) from patients with specific *SCN2A* mutations, differentiating them into neural cells, and analyzing their electrophysiological properties. The patient under investigation has a missense mutation at c.4886G>T (p.Arg1629Leu), which can be corrected using CRISPR/Cas9, a revolutionary third-generation gene-editing technology.[58-62] CRISPR/Cas9 enables precise genomic modifications by delivering a Cas9 nuclease complexed with synthetic guide RNA (gRNA) to the cell, allowing us to remove existing genes or add new ones at the target site.[58-63] Furthermore, using Homology Directed Repair (HDR) with a single-stranded oligonucleotide donor (ssODN), pathogenic mutations can be reverted to normal, generating isogenic controls.[60] These isogenic cell lines provide a robust platform for comparative analyses to understand the cellular consequences of *SCN2A* mutations and perform high-throughput genetic and pharmacological screens.[64,65]

Neurons derived from patient-specific iPSCs and isogenic controls are differentiated into GABAergic (inhibitory) and Glutamatergic (excitatory) neurons using Lenti-Virus-mediated expression of ASCL1/DLX2 and NGN2, respectively.[42-48] To replicate the forebrain cortical environment, these neurons are co-cultured with glial cells.[66,67] *In-vitro*, a simplified ratio of 5:5 between neurons and glial cells is used for electrophysiological measurements, while maintaining inhibitory and excitatory neurons at a 3:7 ratio to replicate normal neuronal balance.[68,69] This balance is critical as disruptions in excitatory and inhibitory signaling are a hallmark of epilepsy.

Using these patient-derived and CRISPR/Cas9-corrected isogenic cell lines, comparative analysis at the cellular level can be performed. When differentiated into *SCN2A*-specific neurons, the physiological activity of Glutamatergic and GABAergic neurons can be evaluated to understand the functional impact of *SCN2A* mutations. Electrophysiological recordings, including micro-electrode array (MEA) techniques, enable precise measurements of synaptic activity, neuronal excitability, and network dynamics, providing critical insights into how *SCN2A* mutations contribute to neuronal dysfunction and epilepsy pathophysiology.[70-75]

Finally, using the generated neurons, I identified a sodium channel blocker, Phenytoin, and five novel compounds to evaluate their therapeutic efficacy in *SCN2A*-related epilepsy. Phenytoin was selected based on previous studies confirming its effectiveness in *SCN2A* mutation patients.[76,77] The

five novel compounds, identified through high-throughput screening, were assessed for their potential as targeted therapies for epilepsy.

This study aims to screen patients with voltage-gated sodium channel alpha subunit 1.2 (*SCN2A*) mutations and create gene-specific, differentiated stem cell-derived neurons. By generating patient-specific neurons and isogenic controls, I aim to understand the underlying pathology of *SCN2A*-related disorders and evaluate the electrophysiological activity at the neuronal level. Furthermore, CRISPR/Cas9 technology is utilized to precisely correct pathogenic mutations, enabling comparative analyses between mutant and corrected neurons.

By integrating iPSC differentiation, advanced gene-editing, and electrophysiological assays, this research seeks to address the limitations of conventional epilepsy treatments, which often target symptoms without considering the underlying genetic and pathological causes. This study is expected to contribute to the field of personalized precision medicine by identifying the mutational causes of individualized epilepsy and developing effective treatments that target intermediate pathologies. This study also provides a foundation for advancing our understanding of human brain development and genetically driven epilepsy, offering novel insights for future therapeutic strategies.

2. MATERIALS AND METHODS

2.1. Subjects and Research Design

Patients with epilepsy underwent genetic testing from 2015 to 2023. The specific target gene panel was ordered by the attending physician based on the clinical diagnosis. Specifically, I conducted a study focusing on genes that cause epilepsy due to mutations in ion channel genes. Among these, I targeted patients with mutations in voltage-gated sodium channels. *SCN1A* mutations account for 41% of these cases, and previous research has already been conducted on *SCN1A*. Therefore, I chose to focus my research on *SCN2A*, the second most common sodium ion channelopathy, which accounts for approximately 14% of cases worldwide. Despite this, *SCN2A* remains under-researched, prompting my targeted study.

First, I performed next-generation sequencing (NGS) on patients who consented to additional genetic testing using previously collected DNA samples. NGS was conducted through a live library established by the Department of Diagnostic Laboratories, and all patients had positive NGS results. I summarized the results and their developmental relationships (Table 3). Among the patients with positive NGS results for channelopathies, I obtained blood samples from those with *SCN2A* mutations, with their consent.

2.2. Next Generation Sequencing (NGS)

Genomic DNA (gDNA) from patients was obtained from the Department of Diagnostic Laboratory Medicine and sequenced using the NextSeq 550Dx system or NovaSeq 6000 instrument (Illumina, San Diego, California, United States), with libraries constructed through DNA enrichment (Figure 2). This method has been validated in previous studies[78]. As part of a preliminary study, I conducted targeted gene panel sequencing in children with developmental and epileptic encephalopathy (DEE) and assessed the clinical implications of genotype-phenotype correlations. I evaluated 278 children with DEE using a customized gene panel, and extensively reviewed clinical characteristics, including treatment efficacy according to genotype. Patients with *SCN2A* mutations were identified, and sodium channel blockers were anticipated to be effective in their treatment.

2.3. Genome DNA Extraction from Blood

DNA was extracted from the nuclei of white blood cells (WBCs) in patient blood using the FavorPrep™ Blood / Cultured Cell Genomic DNA Extraction Mini Kit (Favorgen, Ping Tung, Taiwan), following the manufacturer's instructions. Blood samples of up to 6 mL were collected in EDTA tubes and mixed thoroughly by gentle inversion to prevent clotting. Samples were processed immediately or stored at 4°C for up to 3 days. Blood was initially centrifuged at 100 g for 10 minutes to separate the plasma, which was removed, and the remaining blood cells were mixed with eBioscience™ 1X RBC Lysis Buffer (Invitrogen, Middlesex County, Massachusetts, United States) for further processing. The WBCs were then used for genomic DNA extraction.

2.4. Isolation of Human Peripheral Blood Mononuclear Cells (PBMC)

PBMCs were isolated using the Ficoll method. A preliminary study was conducted before the main study, during which 6 mL of blood was collected in an EDTA tube. Mononuclear cells were isolated using Lymphoprep™ (STEMCELL Technologies, Vancouver, Canada) in combination with SepMate™ (STEMCELL Technologies, Vancouver, Canada) (Figure 5). After centrifuging the mixture at 1500 g for 10 minutes, 5×10^6 cells were stored using CryoStor® CS10 (STEMCELL Technologies, Vancouver, Canada). For reprogramming, the cells were cultured in StemSpan™ SFEM II medium with StemSpan™ Erythroid Expansion Supplement (100×), allowing the cells to remain suspended in the medium.

2.5. Human Peripheral Blood Mononuclear Cell (PBMC) Culture

After PBMC isolation, if the cells were frozen, they were mixed with Dulbecco's Phosphate Buffered Saline (DPBS) at a ratio of 1:9, centrifuged at 1600 rpm for 3 minutes, and processed for culture. If proceeding directly after isolation, 5×10^6 PBMCs were cultured for 6 days in a combination of StemSpan™ SFEM II medium and StemSpan™ Erythroid Expansion Supplement (100×). The medium was changed every 2 days for a total of 6 days (Figure 5).

2.6. iPSCs Reprogramming

Reprogramming was conducted using the Epi5™ Episomal iPSC Reprogramming Kit (Invitrogen, Middlesex County, Massachusetts, United States), which includes an episomal vector encoding defined reprogramming factors. Monocytes from *SCN2A* patients were cultured in StemSpan™ SFEM II medium with StemSpan™ Erythroid Expansion Supplement (100×) for 6 days. After incubation, the cells were harvested and resuspended in 100 µL of Opti-MEM™ I Reduced Serum Medium (Invitrogen, Middlesex County, Massachusetts, United States). Subsequently, 1 µL each of the Epi5™ Reprogramming Vectors and p53 & EBNA Vectors were added, and electroporation was performed using the NEPA21 Super Electroporator (NEPA GENE, Shiba, Japan), following the Epi5™ Kit instructions. The study details are summarized in Table 1.

Table 1. NEPA21 Composition Table

#	Set Parameters Porting Pulse V	Length (ms)	Interval (ms)	No.	Drate (%)	Polarity
Control (with cells and DNA but no electroporation)						
1	100	5	50	2	10	+
2	125	2.5	50	2	10	+
3	125	5	50	2	10	+
4	125	7.5	50	2	10	+
5	150	2.5	50	2	10	+
6	150	5	50	2	10	+
7	150	7.5	50	2	10	+
8	175	5	50	2	10	+
9	200	5	50	2	10	+
10	225	2.5	50	2	10	+
11	275	1	50	2	10	+
#	Set Parameters Trans Pulse V	Length (ms)	Interval (ms)	No.	Drate (%)	Polarity
1	20	50	50	5	4	+/-
2	20	50	50	5	4	+/-
3	20	50	50	5	4	+/-
4	20	50	50	5	4	+/-
5	20	50	50	5	4	+/-
6	20	50	50	5	4	+/-

7	20	50	50	5	4	+/-
8	20	50	50	5	4	+/-
9	20	50	50	5	4	+/-
10	20	50	50	5	4	+/-
11	20	50	50	5	4	+/-

Among these parameters, the porting pulse had a voltage of 150V, a length of 5 ms, an interval of 50 ms, No. 2, and a duty rate of 10% with positive polarity. The transfer pulse had a voltage of 20V, a length of 50 ms, an interval of 50 ms, No. 5, and a duty rate of 40% with positive/negative polarity. Electroporation was then performed. The results indicated that the resistance value exceeded 0.5 kΩ, the porting pulse exceeded 3A and 5J, and the transfer pulse exceeded 0.5A and 1J.

Mix Corning® Matrigel® Basement Membrane Matrix, LDEV-free (Corning, Corning, New York, United States), and Dulbecco's Modified Eagle Medium F12 (DMEM F12) (Invitrogen, Middlesex County, Massachusetts, United States) in a 1:90 ratio, and pre-coat the cell culture dish one day in advance. In the culture dish, prepare a medium composed of Neurobasal™ Medium, N-2 Supplement (100×), and B-27™ Supplement (50×), all serum-free (Invitrogen, Middlesex County, Massachusetts, United States). At this point, add Y-27632 dihydrochloride (MedChemExpress, Monmouth Junction, New Jersey, United States) at a concentration of 10 nM to protect the cells from potential damage caused by electroporation. Next, add the electroporated PBMCs and incubate for a minimum of 6 to 15 days. Supplement the prepared medium with Basic Fibroblast Growth Factor (Merck, Darmstadt, Germany) to reach a final concentration of 100 ng/mL. Between days 6 and 15, iPSC colonies resembling human embryonic stem cells (hESCs) were visually inspected. These colonies were manually harvested and subsequently cultured for characterization (Figure 5).

2.7. iPSCs Culture

Human wild-type *SCN2A* induced pluripotent stem cells (iPSCs) derived from episomal vectors were maintained in mTeSR™1 medium (STEMCELL Technologies, Vancouver, Canada), which is a feeder-free medium specifically designed for the cultivation of human pluripotent stem cells. These iPSCs were cultured in MatriGel® Basement Membrane Matrix-coated culture dishes (Corning, Corning, New York, United States) to promote cell adhesion and growth.

To begin the culture, iPSCs were seeded at an initial density of 1×10^5 cells per 35π cell culture dish. The culture medium was changed daily to maintain optimal cell conditions. As iPSCs are

sensitive to mechanical stress and can lose pluripotency under suboptimal conditions, careful monitoring of cell growth and viability was conducted.

For thawing frozen cells and subsequent subcultures, the CEPT Cocktail (MedChemExpress, Monmouth Junction, New Jersey, United States) was used to minimize cell damage and to promote the survival and fitness of self-renewing pluripotent stem cells. The cocktail contains a combination of Chroman 1, Emricasan, Polyamine Supplement (1000×) (Sigma-Aldrich, St. Louis, Missouri, United States), and Trans-ISRIB (MedChemExpress, Monmouth Junction, New Jersey, United States), which was applied at a dilution of 1:1000 in the culture medium.[79] This combination has been shown to enhance the viability of iPSCs by protecting them from apoptosis and promoting their pluripotent properties.

When the cultured iPSCs reached 80% confluence, subculture was performed. The cells were split at a ratio of 1:10 into fresh MatriGel®-coated culture dishes. During subculturing, the following freezing medium was used to preserve the cells for future use: 40% mTeSR1, 50% KnockOut™ Serum Replacement (KOSR) (Invitrogen, Middlesex County, Massachusetts, United States), and 10% Dimethyl sulfoxide (DMSO) (Sigma-Aldrich, St. Louis, Missouri, United States). This freezing medium was carefully prepared to minimize damage during freezing and thawing processes. The cells were stored at -20°C for one day, then transferred to -70°C ~ -80°C for long-term storage. After long-term storage, the cells were further preserved in liquid nitrogen for indefinite storage.

Following thawing, the iPSCs were cultured for at least five passages to stabilize the cells. If the cell condition appeared poor or the growth rate was low, additional passages (up to 2-3 additional passages) were performed. ReLeSR™ (STEMCELL Technologies, Vancouver, Canada), a reagent designed to facilitate the gentle dissociation of cells, was used during subculturing. The culture medium was changed regularly, and cells were maintained at a density sufficient for optimal growth and cell division.

Excess cells that were not needed for immediate use were stored in a deep freezer at -70°C or lower, after being prepared with the freezing medium. When storing cells in liquid nitrogen, the freezing process was carried out carefully to avoid the formation of ice crystals within the cells, which can lead to cell damage. After the freezing process, cells were transferred to a liquid nitrogen storage tank for long-term preservation, ensuring the viability of the cells for future experiments.

2.8. Differentiation into Three Germ Layers

Patients with epilepsy underwent genetic testing from 2015 to 2023. The specific target gene panel was ordered by the attending physician based on the clinical diagnosis.

To assess *in-vitro* differentiation of iPSCs into the three germ layers, embryonic bodies (EBs) were formed by partial dissociation using AggreWell™800[80] (STEMCELL Technologies, Vancouver, Canada). First, 500 μL of Anti-Adherence Rinsing Solution (STEMCELL Technologies, Vancouver, Canada) was added and left at room temperature for 5 minutes, followed by centrifugation at 100 g for 3 minutes. After removing the solution, 500 μL of mTeSR™ and 0.5 μL of CEPT were added, along with 1×10^6 iPSCs. After one day of incubation, EBs were formed. Subsequently, 20% KOSR, 1% Penicillin-Streptomycin (10,000 U/mL) (Invitrogen, Middlesex County, Massachusetts, United States), 1% MEM Non-Essential Amino Acids Solution (100×) (Invitrogen, Middlesex County, Massachusetts, United States), and 1% 2-Mercaptoethanol (Sigma-Aldrich, St. Louis, Missouri, United States) were added to DMEM/F12 medium. The volume was maintained at 1 mL by removing and adding 0.5 mL of EB Media daily.

EBs were then transferred to Matrigel®-coated culture dishes and cultured for 14-21 days. Immunostaining with appropriate antibodies confirmed the spontaneous differentiation of EBs into three germ layers (Table 6).

2.9. Genome DNA Extraction in iPSCs and Identification of Variants

DNA extraction was performed from intracellular nuclei using the Blood & Cell Culture DNA Midi Kit (QIAGEN, Hilden, Germany), according to the manufacturer's instructions.

iPSCs were cultured for at least five passages, and genomic DNA (gDNA) extraction was performed when the cell population reached 1×10^6 cells (or 1×10^7 for monocytes). Cells were treated with Accutase® solution (Sigma-Aldrich, St. Louis, Missouri, United States) for 10 minutes before subculturing, turning them into single cells, and then counted using a hemocytometer.

PCR was performed using the following primers to determine the mutation location (Table 4). PCR was conducted with AccuPower® Taq PCR PreMix (Bioneer, Daejeon, Republic of Korea) using 10 pmol of previously defined primers and 500 ng/μL of gDNA, for 35 cycles. The cycles included: pre-denaturation at 95℃ for 5 minutes, denaturation at 95℃ for 30 seconds, annealing at 53℃ for 30 seconds, extension at 72℃ for 1 minute, and a final extension at 72℃ for 5 minutes.

2.10. Identify Sequencing Locations after Gel Extraction

A 2% agarose gel was prepared using 0.5x Tris-acetate-EDTA (TAE) (Sigma-Aldrich, St. Louis, Missouri, United States), and electrophoresis was performed at 135 volts for 35 minutes to determine DNA size. Once the DNA fragment size of 738 bp was confirmed, it was excised, and gel extraction was performed using DNA Fragment Purification Kits - Gel/PCR Purification & Clean-up (Favorgen, Ping Tung, Taiwan). The extracted DNA was sent for Sanger sequencing at BIONICS (Seoul, Republic of Korea) to confirm the mutation location and pattern.

2.11. Karyotyping

G-banding karyotyping was performed at passage 20 by DX&VX (Seoul, Republic of Korea), following a standard protocol for GTG banding. A total of 20 passages were analyzed at 550 band resolution.

2.12. Immunocytochemistry

iPSCs were fixed with 4% paraformaldehyde in PBS for 15 minutes, washed with PBS, and permeabilized with PBS containing 0.1% Triton X-100 for 15 minutes at room temperature. Samples were then incubated with blocking buffer (PBS containing 2% bovine serum albumin, Sigma-Aldrich, St. Louis, Missouri, United States) for 1 hour. Primary antibodies diluted in blocking buffer were applied overnight at 4°C. The next day, samples were washed three times with PBS and incubated with fluorescently tagged secondary antibodies for 2 hours at room temperature. Coverslips were washed three times with PBS and mounted using VECTASHIELD® Antifade Mounting Medium (VectorBuilder, Chicago, Illinois, United States) with DAPI or without DAPI (Table 6). Fluorescence imaging was performed using a pE-300lite LED fluorometer (Olympus, Tokyo, Japan) and an IX74 microscope with a DP74 digital camera (Olympus, Tokyo, Japan).

2.13. STR Analysis

Short tandem repeat (STR) analysis compares allelic repeats at specific loci in DNA between samples. STR analysis was performed by Cosmogentech Inc. (Seoul, Republic of Korea) on two samples. First, the gDNA from the patient's mononuclear cells was compared with the gDNA from the patient's iPSCs. Then, the gDNA from the calibrated iPSCs was compared with the original iPSCs. iPSCs were harvested at passage 10.

2.14. CRISPR/CAS9 Vector Design

The vector design was based on existing NGS data. First, guideRNA (gRNA) was designed using Merck CRISPR Design Tools (Merck Millipore, Burlington, Massachusetts, United States), and the gRNA and PAM sequences were verified using Benchling's CRISPR/CAS9 Tool (Benching, San Francisco, California, United States).

Based on the obtained data, a CRISPR/CAS9 vector was created using the Vector Design tool provided by VectorBuilder (VectorBuilder, Chicago, Illinois, United States) (Table 7, Figure 10). Importantly, the sgRNA was designed according to the mutation pattern at the mutation site, and ssODNs were created at the target location by BIONICS.

2.15. CRISPR/CAS9 Editing of *SCN2A*

Using CRISPR/Cas9 technology, I generated a heterozygous indel mutation in the *SCN2A* gene at c.4886 G>T in an iPSC line derived from a patient with an *SCN2A* mutation. An sgRNA targeting *SCN2A* (CCGAGTGATCCTTCTTGCC) was designed and cloned into the pRP(CRISPR)-EGFP/Puro-hCas9-U6>gRNA vector (VectorBuilder, Chicago, Illinois, United States).

The iPSCs were passaged approximately 10 times, and 1×10^6 cells were used for electroporation using NEPA21. Electroporation was performed using the following parameters: pulse voltage of 125V, pulse length of 5 ms, pulse interval of 5 ms, with No. 2, a duty rate of 10%, and positive polarity. Trans pulses were applied at 20V, with a pulse length of 50 ms, pulse interval of 50 ms, with No. 5, and a duty rate of 40%, using positive/negative polarity.

Post-electroporation, cells were treated with SCR7 pyrazine (Sigma-Aldrich, St. Louis, Missouri, United States) at a concentration of 10 μM for 3 days to facilitate HDR. Additionally, p53 inhibitor Pifithrin-alpha (Sigma-Aldrich, St. Louis, Missouri, United States) was added for 1 day to

prevent apoptosis. Cells were resuspended in mTeSR medium supplemented with CEPT and seeded onto Matrigel-coated plates.

One day after nucleation, cells expressing eGFP were sorted by FACs, and unsorted cells were further screened by adding puromycin dihydrochloride (1 μg/mL) (Sigma-Aldrich, St. Louis, Missouri, United States) for 3 days. Sanger sequencing was performed to confirm heterozygous editing at c.4887. Two positive clones were selected for further characterization. Cells were routinely tested for mycoplasma contamination. Immunocytochemistry was used to detect pluripotency markers OCT4, NANOG, SSEA4, and TRA1-81. Karyotyping was performed by Dx&Vx Inc. Off-target sites were identified using CAS-Offinder (http://www.rgenome.net/cas-offinder/) and Benchling, and sites with a score of 1 or higher were confirmed by Sanger sequencing (Table 9, Figure 16).

2.16. Isogenic Cell Culture

After CRISPR/CAS9 editing and puromycin selection, cells were transferred into 96-well plates and cultured for approximately 5 days. Subsequently, half of the cells were used for gDNA extraction without cell counting. After successful Sanger sequencing, edited cells were transferred to 6-well plates coated with Matrigel, and mTeSR1 medium supplemented with CEPT was added. Cells were cultured for an additional 6 days to obtain healthy cells.

2.17. Confirmation of OFF-Target

For off-target analysis, I identified potential off-target sites using CAS-Offinder and Benchling. Sites with a score of 1 or higher were selected for further analysis. Primers were designed for these sites, and Sanger sequencing was performed to confirm off-target effects (Table 9, Figure 16).

2.18. Lenti-Virus Design

To induce neuronal differentiation, transcription factors were expressed to direct differentiation into specific neuron types. Differentiation was aimed at generating both inhibitory neurons

(GABAergic neurons) and excitatory neurons (glutamatergic neurons) to simulate a forebrain cortex environment. A Lenti-virus was designed using the Tet-On system. For GABAergic neurons, ASCL1 and DLX2 were expressed, along with RFP for tracking virus infection via fluorescence, and Anti-Puro was added for selection. For glutamatergic neurons, Neurog2 (NGN2) was introduced into the Lenti-virus, with eGFP for fluorescence tracking, and Anti-Puro for selection. The rtTA was also produced in the same way, but without selection markers. The Lenti-virus design was created using VectorBuilder (Table 11-16).

2.19. Neuron Differentiation

Lenti-virus was used for neuronal differentiation. First, iPSCs were seeded at 1×10^7 in a 35π Matrigel-coated culture dish and grown for more than one day. Then, 1 titer of Lenti-virus containing transcription factors and 1 titer of Lenti-virus containing rtTA were added to induce differentiation into the desired neurons.

Sixteen hours after infection, the medium was changed to Neuronal Growth Media (NGM), consisting of Neurobasal Plus (Gibco, Grand Island, New York, United States), N2 Serum-Free Supplement, B-27™ Plus Supplement, L-Ascorbic acid (100 μM final concentration), Recombinant Human/Murine/Rat BDNF (10 ng/μL final concentration), Recombinant Human GDNF (10 ng/μL final concentration), Bucladesine sodium (dbcAMP) (250 μM final concentration), and GlutaMAX™ Supplement (x1 final concentration). Doxycycline monohydrate (1 μg/mL final concentration) was added to induce transcription factor expression. After 1 day, virus infection was confirmed by fluorescence.[81]

Following virus confirmation, puromycin was added at 1 μg/mL final concentration for 3 days to select infected cells. To prevent cell division, 1-β-D-Arabinofuranosylcytosine (Ara-C) was added at 1 μg/mL final concentration for 2 days, and Forskolin was added at 20 μM for 2 days to increase cyclin AMP activity.[82,83] Afterward, NGM Media was applied for 1 day before co-culture with astrocytes.

2.20. Neuron Culture

Neuron culture began on DAY 1, defined as the day Doxycycline was added. Cells were cultured for approximately one week, with the NGM Media replaced daily. The day before neurons

reached 1 week of age, astrocytes (1×10^5 cells) were seeded onto Matrigel-coated cover slips in 24-well plates.

Neurons were dissociated into single cells with Accutase and divided into 5×10^4 cells for patch-clamp measurements. Another set of neurons (5×10^4 cells) was cultured on cover slips in NGM Media mixed with 10% Mouse Astrocyte Conditioned Medium from C57BL/6 (ScienCell Research Laboratories, Carlsbad, California, United States). These cells were used for ICC and cDNA synthesis.

For Micro Electrode Array (MEA) recordings, Matrigel-coated cover slips with astrocytes (5×10^4 cells) were prepared. In the MEA plate, 1.5×10^4 GABAergic neurons and 3.5×10^4 glutamatergic neurons were added, bringing the total number of cultured cells to 1×10^5. Media changes were performed every 2 days, with 50% of the media replaced at each change.

2.21. Mouse Astrocyte Primary Culture

Mouse astrocyte primary cultures were prepared according to the guidelines of the Institutional Animal Care and Use Committee (IACUC, 2018-0187) at the Department of Experimental Animals, Severance Hospital, Yonsei University. The method for astrocyte isolation and culture was based on the protocol outlined by Schildge et al. in their 2013 publication in Journal of Visualized Experiments.[84]

2.22. mRNA Extraction and cDNA Synthesis

The mRNA was extracted from neurons cultured without astrocytes for 3 to 7 weeks. The extraction procedure involved adding 1 mL of TRIzol™ Reagent (Sigma-Aldrich, St. Louis, Missouri, United States) and 200 µL of chloroform, vortexing, and incubating the mixture on ice for 15 minutes. After centrifuging at 12,000 g for 10 minutes at 4°C, the supernatant was transferred, and 500 µL of 2-Propanol was added, followed by a 10-minute incubation on ice. After centrifugation, the supernatant was discarded, and the pellet was washed with 1 mL of 70% ethanol. After air-drying, the RNA pellet was resuspended in 50 µL of UltraPure™ DEPC-Treated Water (Invitrogen, Middlesex County, Massachusetts, United States) and stored at -20°C.

For cDNA synthesis, PrimeScript™ RT Master Mix (Takara, Shiga-ken, Japan) was used. The mRNA concentration was measured using a Nanodrop, and 500 ng of mRNA was adjusted with DEPC-treated water. The reaction mixture included 2 μL of 5X PrimeScript RT Master Mix, and the final volume was adjusted to 10 μL. The PCR conditions included reverse transcription at 37°C for 15 minutes, followed by heat inactivation at 85°C for 5 seconds.

2.23. Neuron Characterization (PCR)

PCR was performed using AccuPower® Taq PCR PreMix (Bioneer, Daejeon, Republic of Korea) with 10 pmol of primers and 500 ng/μL of cDNA. The PCR cycle included pre-denaturation at 95°C for 5 minutes (1 cycle), denaturation at 95°C for 30 seconds, annealing at 50°C for 30 seconds, extension at 72°C for 1 minute (35 cycles), and a final extension at 72°C for 5 minutes (1 cycle). The cDNA used in the PCR reactions was synthesized in previous steps (Table 17).

2.24. Pharmacological Experiment

Phenytoin-Na from SAMJIN Pharm (Seoul, Republic of Korea) and Phenytoin Sodium (SAMJIN Pharm, Seoul, Republic of Korea) were used in the pharmacological experiments. Other compounds are currently under development. Five new sodium blockers were provided by Prof. Dokyun Na's team at Chung-Ang University, named 4456-3635 (4456), 2786-4513 (2786), 4561-0590 (4561), 4333-1696 (4333), and 6466-0224 (6466).

2.25. Micro-Electrode Array (MEA) Recordings and Analysis

All recordings were performed using a 24-well MEA system with the Maestro Edge (Axion BioSystems, Atlanta, Georgia, United States). A total of 1.5×10^4 GABAergic neurons, 3.5×10^4 glutamatergic neurons, and 5×10^4 astrocytes were seeded into each MEA well for a total of 1×10^5 cells. Spontaneous electrophysiological activity of *SCN2A* iPSC-derived neural networks and calibrated *SCN2A* iPSC-derived neural networks was recorded for 15 minutes at 37°C in a chamber maintained with 95% O_2 and 5% CO_2.

Recordings were sampled at 10 kHz and filtered with a 100 Hz high-pass filter and a 3500 Hz low-pass filter. Spike detection was set at ± 4.5 standard deviations. Mean firing rate (MFR) was calculated as the average spike frequency of all channels in an MEA well. Burst detection identified channels with at least five spikes in a burst (threshold of 0.4 bursts/s, minimum inter-burst interval of 100 ms). A network burst was defined as synchronous bursts across more than 35% of the channels in a well. Data analysis was conducted using Axion's multiwell analyzer software (AxlS), following the user guidelines provided by Axion (Table 2).
Corrected *SCN2A* neurons and *SCN2A* neuron networks were compared and analyzed at DIV 21, DIV 28, and DIV 35. The *SCN2A* neuron networks on MEA were treated with Phenytoin-Na, 4456, 2786, 4561, 4333, and 6466 at DIV 42. For each drug, the concentration was gradually increased from low to high. Each drug was added and allowed to react for 10 minutes prior to measurement. Spontaneous activity was then measured for 15 minutes.

Table 2. MEA Define

Metric	Definition
Number of Spikes	The total number of spikes in the analysis period.
Mean Firing Rate	The total number of spikes divided by the duration of the analysis, in Hz.
ISI Coefficient of Variation	The coefficient of variation (standard deviation/mean) of the inter-spike interval or inter-spike time for electrodes with more activity than the minimum spike rate ("active electrodes"). This metric measures spike regularity, where 0 represents perfectly distributed spikes and 1 or higher represents bursting. When bursts are clearly distinguishable from interruptions, the standard deviation of the ISI will increase because spikes within one burst will have a small ISI, while the ISI between the last spike of one burst and the first spike of the next burst will be larger.
Network ISI Coefficient of Variation	The variation coefficient (standard deviation/mean) of the inter-spike interval for all spikes on all electrodes in the well. This is a measurement of spike regularities across the network. This metric captures the spread of spikes, with a value of 0 indicating spikes are perfectly distributed and a value above 1 indicative of network bursting.
Fano Factor	The Fano coefficient is a measure of spike count variation over time. The Fano coefficient is computed as the 6-second spike count variance split by the 6-second spike count mean. The Fano coefficient is computed independently for each active electrode or unit and then is averaged across active electrodes or units to calculate the well-wide Fano coefficient. An active electrode or unit is considered to be an electrode or unit with activity greater than the minimum spike rate. The triggered Fano coefficient is also available.
Number of Active Electrodes	The number of electrodes with activity greater than the minimum spike rate established in the assay parameters.
Weighted Mean Firing Rate	The average firing rate that is based only on electrodes with activity greater than the minimum spike rate ("active electrodes").
Number of Bursts	The total number of active single-electrode bursts during the analysis period. For wells, the total number of electrode bursts is reported across all electrodes in the well.
Number of Bursting Electrodes	The total number of electrodes in the well that have a burst count per minute that is greater than the burst electrode criterion.
Burst Duration	The average time from the first to last spike in a single electrode burst. For electrodes, the burst overall average is reported. For wells, the average across

	electrodes is reported. A longer burst indicates more excitation and less inhibition because it takes longer to end the burst.
Number of Spikes per Burst	The average number of spikes in a single electrode burst. For electrodes, the burst-wide average is reported. For the well, the average across electrodes is also reported.
Mean ISI within Burst	The average inter-spike interval, the time between spikes, for the spikes in a single electrode burst. For electrodes, the burst average mean is reported. For wells, the electrode average overall average is reported. This is a measure of burst strength, with smaller values indicating stronger bursts.
Median ISI within Burst	Median inter-spike interval, the amount of time between spikes, for spikes in a single electrode burst. For electrodes, the average of the burst median ISI is also reported. For wells, the average across electrodes gets reported.
Median/Mean ISI within Burst	Median/average inter-spike interval (ISI) within a single electrode burst. A value closer to 1 indicates that the distribution of ISI within the burst is more symmetrical. For electrodes, the average of the burst median/mean ISI is also reported. For wells, the average of the electrode median/average ISI is averaged.
Inter-Burst Interval	The average time between burst starts for a single electrode. For electrodes, the average across bursts are reported. For a well, the electrode overall average is reported.
Burst Frequency	The total number of Single Electrode Bursts in Hz divided by the analysis period. For a well, the average of the electrode burst frequencies are reported.
Normalized Duration IQR	Interquartile range of single-electrode burst-duration. This Metric measures the regularity of single electrode burst duration. This value is smaller if the middle 50% of single-electrode bursts are close to the same duration, and this range grows larger if the duration of single-electrode bursts are highly variable. For wells, the mean of the normalized duration IQR across electrodes is also reported.
IBI Coefficient of Variation	The coefficient of variation (standard deviation/mean) of the inter-burst interval, which is the time between single-electrode bursts. This is a measure of the regularity of single-electrode bursts. For wells, the average of the electrode IBI CoVs is also reported.
Burst Percentage	This is the number of spikes in a single electrode burst multiplied by 100, divided by the total number of spikes. For wells, the average of the electrode burst rate are reported.
Network Bursts Ignored Flag	A flag indicating whether network bursts were disregarded in this well. Ignore network bursts = 1, include network bursts = 0.
Number of Network Bursts	The total number of network bursts in the analysis time period.
Network Burst Frequency	The total number of network bursts divided by the analysis period in Hz.
Network Burst Duration	The average time from first spike to last spike of a network burst. Longer bursts indicate more excitement and less inhibition because it takes longer to end the burst.
Number of Spikes per Network Burst	The average number of spikes in a network burst.
Mean ISI within Network Burst	The average of the average ISIs within the network burst.
Median ISI within Network Burst	The average of the median ISIs within the network burst.
Median/Mean ISI within Network Burst	The average of the median/mean ISIs within the network burst. A value closer to 1 indicates that the distribution of ISIs within the burst is symmetrical.
ISI CoV within Network Burst	The network burst-wide average of the ISI CoV (standard deviation/mean of the inter-spike interval) within the network burst.

Number of Electrodes Participating in Burst	The average number of electrodes with activity during a network burst.
Number of Spikes per Network Burst per Channel	The network burst-wide average of the number of spikes in a network burst divided by the number of electrodes participating in that burst.
Network Burst Percentage	The number of spikes in a network burst divided by the total number of spikes, multiplied by 100.
Network IBI Coefficient of Variation	The coefficient of variation (standard deviation/mean) of the interval between network bursts, which is the time between network bursts. This is a measure of the rhythmicity of network bursts: bursts that occur at regular intervals have a small coefficient of variation, and bursts that occur sporadically have a large coefficient of variation.
Network Normalized Duration IQR	Interquartile range of network burst duration. This metric measures the regularity of network burst duration. This value is small if the middle 50% of network bursts are close to the same duration, and this range is large if the duration of network bursts is highly variable.
Area Under Normalized Cross-Correlation	The area under the cross-correlation between the pooled electrodes, normalized by the autocorrelation. A larger area indicates better synchronization.
Area Under Cross- Correlation	Area under the wide pooled inter-electrode cross-correlation.
Full Width at Half Height of Normalized Cross- Correlation	The distance (probability) along the x-axis (phase lag) from the height of the left half of the normalized cross-correlation plot to the height of the right half. This value is a measure of network synchronization, with a larger half width indicating a wider correlation (less synchronization) and a smaller half width indicating a larger correlation (more synchronization).
Full Width at Half Height of Cross-Correlation	The distance (probability) along the x-axis from the height of the left half of the cross-correlation graph to the height of the right half (phase lag). A larger overall width indicates a wider correlation graph (less synchronization), and a smaller overall width indicates a longer correlation graph (more synchronization).
Synchrony Index	A unitless measure of synchronization between 0 and 1, with values closer to 1 indicating higher synchronization.
Kreuz SPIKE Distance	The 1-Kreutz spike distance, where 1 represents perfect synchronization and 0 represents perfect desynchronization, is calculated using only one previous spike and one subsequent spike for each reference spike. The time window for each calculation depends on the local firing rate of each spike train. Tracks instantaneous changes in clustering that are not distorted by spike spacing between individual electrodes.
Number of Trials	The number of stimulus events used in the analysis.
Evoked Spike Count	The average of all trials of the number of spikes detected from the active electrode in the well over the time period specified in the Stimulation parameters section. Measures the magnitude of the stimulus response.
Evoked Response Probability	The probability of finding at least one spike in the well during the time window specified in the Stimulation Parameters section. Calculated as the number of stimulus events that triggered a response divided by the total number of stimulus events. A measure of the response to a stimulus.
Evoked First Spike Latency	The trial-wide average of the time between the stimulus event and the first post-stimulus spike detected in the well.
Evoked Jitter	The standard deviation across trials for the time between the stimulus event and the first post-stimulus spike detected in the well. This is a measure of response consistency, with lower values indicating a more consistent response.

Evoked CoV2	The square of the coefficient of variation (standard deviation/mean) of the inter-spike interval during the evoked response, averaged over multiple trials. This metric measures the regularity of spike timing during the evoked response.
Evoked Fano Factor	Fano's coefficient is a measure of spike count variability across trials, which is a measure of variability in evoked response size. The Fano coefficient is calculated as the variance of the number of spikes across trials divided by the mean of the number of spikes across trials and is calculated for each active electrode (or active unit). Spikes are counted for the evoked response time window entered in the Stimulus parameter. For well-wide evoked Fano coefficients, the Fano coefficient is calculated based on spikes pooled from all active electrodes (or active units) in the well during the evoked response time window.
Start Electrode	The electrode that most commonly contributes the first spike to a network burst.
Percent Bursts with Start Electrode	The percentage of network bursts that begin with a spike from the starting electrode.
Burst Peak (Max Spikes per sec)	The maximum number of spikes per second of the average network burst. This value is the peak of the average network burst histogram divided by the histogram bin size, which is equal to the number of spikes per second in Hz.
Time to Burst Peak (ms)	The time from the start to the peak of the average network burst. This value is equal to the time to the peak of the average network burst histogram.
Avg Network Burst CoV2	The square of the coefficient of variation (standard deviation/mean) of the inter-spike interval within the average network burst time window. This metric measures the regularity of spike timing during a network burst.
Avg Network Burst Fano Factor	The Fano coefficient is calculated as the variance of the number of spikes across the network burst divided by the mean of the number of spikes across the network burst, and is calculated for each active electrode (or active unit). Spikes are counted over the average network burst time window entered in the Average Network Burst parameter. The Fano coefficient measures the variability of the spike count across network bursts.
Resistance (kOhms)	Resistance is a measure of viable cell coverage for the electrodes: higher values indicate more intact cells attached to the electrodes. For wells, the average across electrodes is reported. (For more information, see the MEA viability chapter in the AxIS Navigator user guide.)
Number of Covered Electrodes	The total number of covered electrodes within the well. A covered electrode is defined as an electrode with a resistance greater than the covered electrode threshold (18 kOhm by default). Uncovered CytoView MEA microelectrodes in the medium exhibit a resistance of 8 to 12 kOhm. After neuronal death, debris can leave behind a slightly higher uncovered resistance of 15-18 kOhms.
Weighted Mean Resistance (kOhms)	Average resistance at the covered electrode only (resistance greater than the covered electrode threshold).

2.26. Electrophysiological Recording – Patch Clamp

The functionality of differentiated glutamatergic neurons was examined using whole-cell patch-clamp recordings. Electrophysiological recordings were performed at room temperature. Glass coverslips containing iPSC-derived neurons were transferred to a recording chamber

constantly perfused with an extracellular solution (in mM: 150 NaCl, 4 KCl, 2.5 $CaCl_2$, 10 glucose, 2 $MgCl_2$, and 10 HEPES; pH 7.4 with NaOH; 320–340 mOsm with sucrose).

Micropipettes (resistance 3-5 MΩ) were pulled from borosilicate glass capillaries using a microelectrode puller (P-97; Sutter Instrument Co., Novato, CA) and filled with intracellular solution (in mM: 140 K-gluconate, 10 HEPES, 2 $MgCl_2$, 2 $CaCl_2$, 11 EGTA, 4 K2-ATP, 0.3 Na2-GTP; pH 7.2–7.3 with KOH, 300–320 mOsm with sucrose).

Recording signals from iPSC-derived neurons were amplified using an Axoclamp-700A amplifier (bandwidth filter set at 10 kHz for current-clamp or 1 kHz for voltage-clamp recordings) and digitized using a Digidata 1440 (pClamp 10.3; Molecular Devices, Sunnyvale, CA). Electrophysiological data were analyzed using Clampfit (Molecular Devices) and presented as means ± SEM.

2.27. Quantification and Statistical Analysis

Statistical analysis was performed using GraphPad Prism 9 (GraphPad Software Inc., Boston, Massachusetts, United States). The Shapiro-Wilk normality test was used to confirm normal distribution. Analyses were conducted using unpaired Student's t-tests or one-way analysis of variance (ANOVA) with sequential post hoc Bonferroni correction for comparing two variables at a single time point. Results with p values less than 0.05 were considered statistically significant: $p < 0.05$ (*), $p < 0.01$ (**), $p < 0.001$ (***), $p < 0.0001$ (****). Data are presented as mean ± standard error of the mean (SEM). Basic statistical details can be found in the figure legends.

3. Results

This study identified the *SCN2A* mutation (c.4886G>T, p.Arg1629Leu) as a causative factor in a patient with developmental and epileptic encephalopathy (EE). This mutation, located in the 2q24.3 region, was confirmed through Next-Generation Sequencing (NGS)[78] and Sanger sequencing (Figure 2, Table 3). It was classified as "likely pathogenic" based on ACMG guidelines and has been associated with severe early-onset epilepsy.

Despite initial treatment using sodium channel blockers, which are commonly recommended for *SCN2A* mutations, the patient's symptoms did not improve. This highlighted the need for further investigation into the mutation's pathological effects. Peripheral blood mononuclear cells (PBMCs) from the patient were reprogrammed into induced pluripotent stem cells (iPSCs) to create a cellular model for detailed study (Figure 3). The generated iPSCs expressed key pluripotency markers, including NANOG, OCT4, and SSEA4, and retained the *SCN2A* mutation, as confirmed through Sanger sequencing.

To investigate the mutation's impact on neuronal function, gene editing was performed using CRISPR/Cas9 to create isogenic cell lines with corrected *SCN2A* alleles. These iPSCs were then differentiated into inhibitory GABAergic neurons and excitatory glutamatergic neurons, providing a robust platform to study the functional consequences of the mutation. This approach also enables pharmacological testing within a brain-like environment, paving the way for personalized therapeutic strategies.

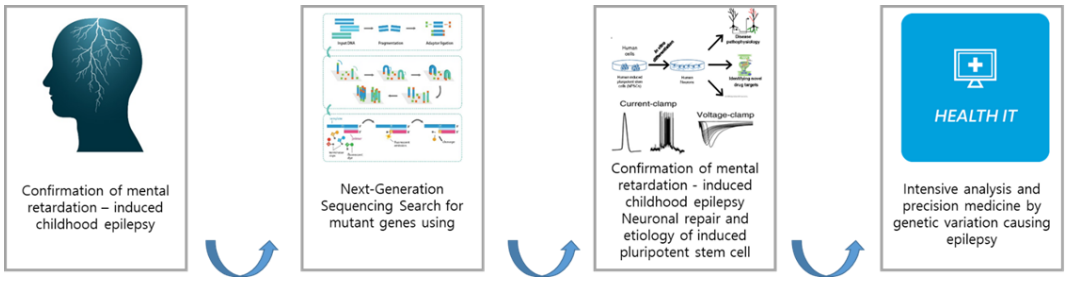

Figure 1. Research Goal/Process : The overall design of this study is structured to first identify a patient with epilepsy, then obtain the patient's genetic information and identify mutations using advanced research technologies such as Next-Generation Sequencing. After identifying the genetic mutations, in-vitro disease modeling is conducted by reprogramming mononuclear cells from the patient's blood to obtain patient-specific induced pluripotent stem cells (iPSCs). Using CRISPR/Cas9 technology, the patient's gene is corrected in-vitro to create an isogenic cell line. Subsequently, both inhibitory and excitatory neurons within the central nervous system (CNS) environment are differentiated from the iPSCs through the introduction of differentiation factors via Lenti-Virus. These neuronal cell lines are then compared and analyzed. Furthermore, drug screening is performed using new pharmaceutical candidates to assess the effects on these differentiated neurons. The final design of this study is aimed at intensive analysis and the development of customized precision medicine.

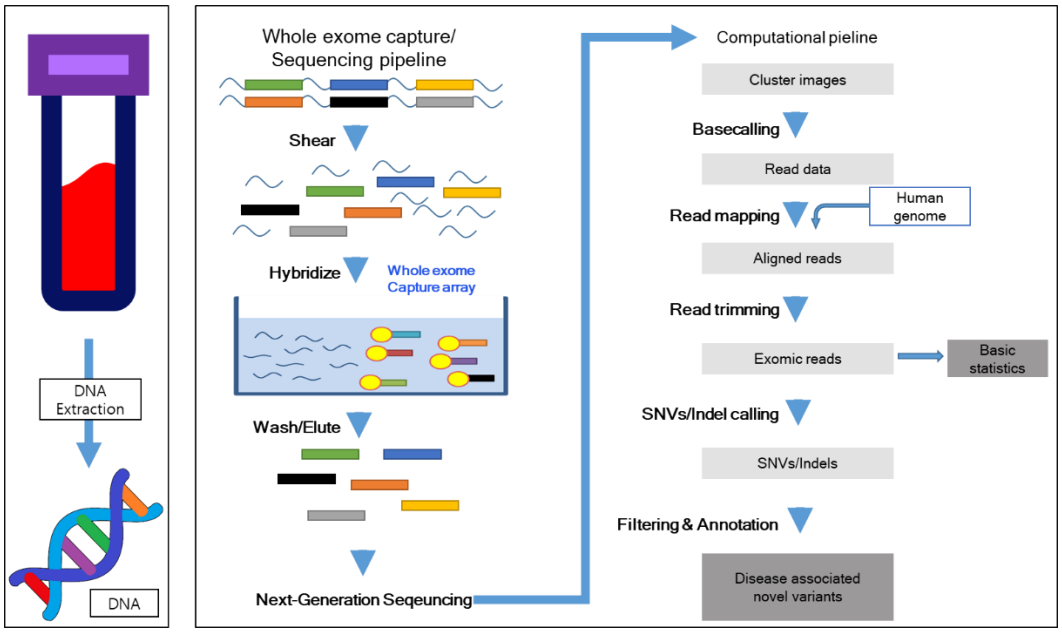

Figure 2. Schematic of NGS for patient genetic variant identification: DNA Extraction and NGS process. The NGS is based on the basic Whole Exome Sequencig, which was used for genotype-phenotype correlation with a gene panel of epilepsy patients previously studied. This allowed us to find genetic variants in patients with suspected *SCN2A*.

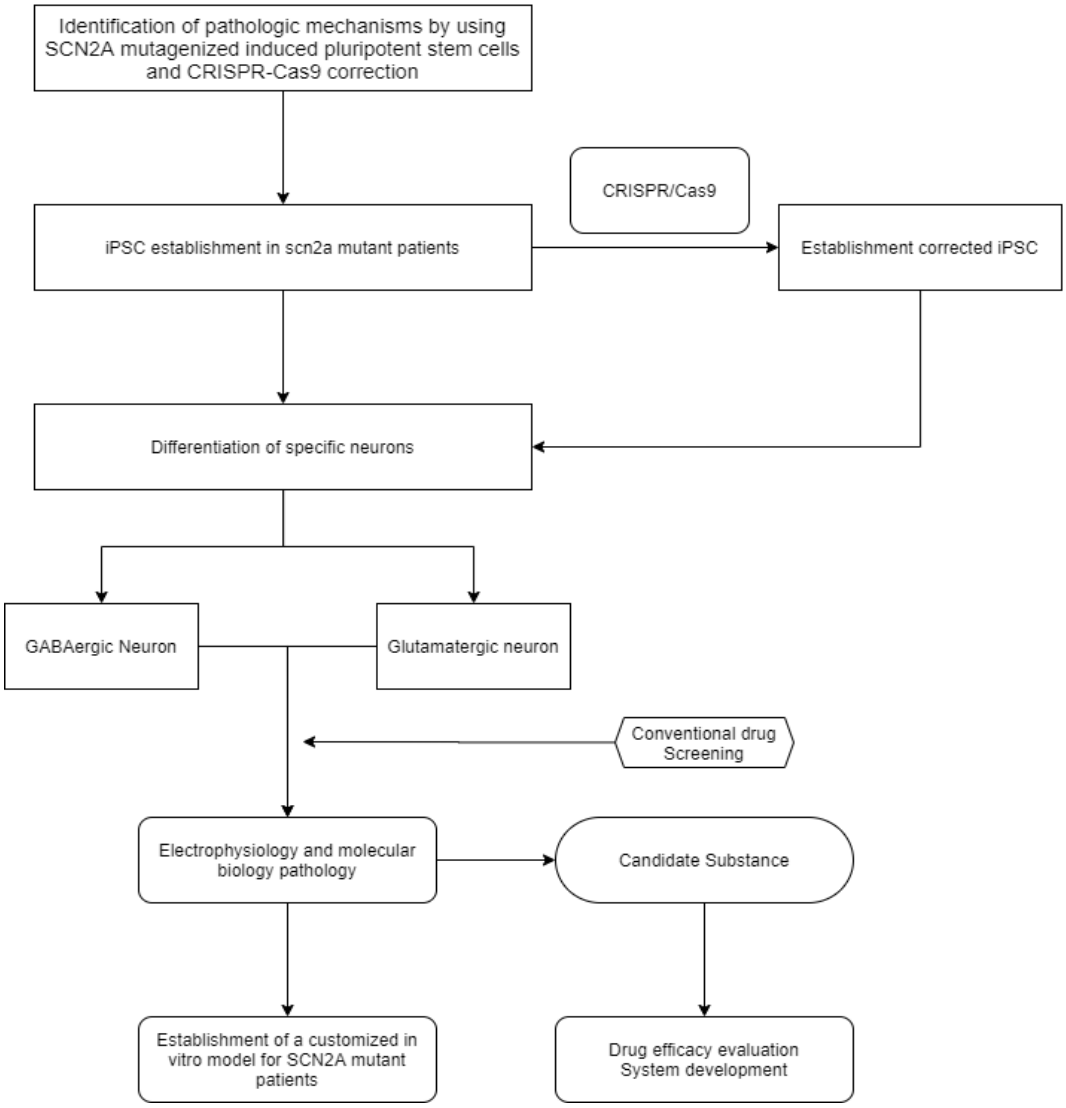

Figure 3. CRISPR/CAS9 usage mechanism schematic (applied to *SCN2A* patient iPSCs)

Table 3. *SCN2A* Patient information

Title	Information
Screening Number	2AMJH
Sex	Male
Gene Mutation	*SCN2A*
ACMG Classification	Likely pathogenic
Accession	NM_021007.2
Nucleotide	c.4886G>T
Amino Acid	p.Arg1629Leu
Seizure onset	4days
Zygosity	Hetero
Disorder (OMIM, HGMD)	Epileptic encenphalopathy, early infantile, 11, 613721 (3), Autosomal dominant; Seizures, benign familial infantile, 3, 607745 (3), Autosomal dominant
Seizure status	Very BAD
Developmental status	Very BAD
DX	OS, MPSI
Comment	Less effective against sodium channel blockers
Remark Comment	Denovo
Seizure Onset	4 Days

3.1. Confirmation of *SCN2A* Patient Genetic Variants, PBMC Culture, and Reprogramming of Induced Pluripotent Stem Cells

Patient DNA was extracted from blood samples collected in EDTA tubes and analyzed using Next-Generation Sequencing (NGS) to identify genetic variants (Table 3). Sanger sequencing was performed to confirm the mutation site, pinpointing a c.4886G>T substitution in the *SCN2A* gene, located at 2q24.3 in segment 4 of domain II (Figure 4A). At the amino acid level, this mutation resulted in the substitution of arginine with leucine at position 1629 (p.Arg1629Leu), a change confirmed by sequencing. The mutation was heterozygous, indicating one altered allele and one normal allele (Figure 4B). This missense mutation, while novel, aligns with mutations previously observed in patients with early-onset epileptic encephalopathy, affecting the voltage-gated sodium channel's function.

Peripheral blood mononuclear cells (PBMCs) were isolated from the patient's blood using the Ficoll-Hypaque method, a widely used technique for efficient PBMC separation. These cells were cultured and reprogrammed into induced pluripotent stem cells (iPSCs) using an episomal plasmid vector expressing pluripotency factors (Oct4, Sox2, Klf4, L-Myc, and Lin28), along with mp53DD and EBNA for enhanced efficiency. This method, originally established by Prof. Yamanaka, enabled integration-free reprogramming through electroporation (Figure 5)[40,41]. Several iPSC colonies resembling human embryonic stem cells (hESCs) were successfully generated.

The iPSCs were validated through immunocytochemistry, confirming the expression of pluripotency markers NANOG, OCT4, and SOX2, as well as surface markers TRA-1-60, SSEA4, and TRA-1-81 (Figure 6, Table 5). Short Tandem Repeat (STR) analysis confirmed genetic consistency between the iPSCs and the original mononuclear cells (Figure 7A). Sanger sequencing further verified that the mutation in the iPSCs matched the patient's original mutation (Figure 7B, Table 4).

The iPSC line was cultured for at least five passages and underwent karyotyping to confirm a normal 46XY karyotype (Figure 8A). To assess pluripotency, iPSCs were differentiated into embryoid bodies (EBs) and further into the three germ layers: ectoderm, mesoderm, and endoderm.[85] Marker analysis revealed the expression of TUJ1 and PAX6 (ectoderm), Brachyury and Alpha-Smooth Muscle Actin (mesoderm), and FOXA2 and alpha-Fetoprotein (endoderm), confirming the iPSCs' ability to generate cell types from all three germ layers (Figure 8B, Table 6).

This comprehensive validation established the *SCN2A* patient-derived iPSC line as a robust platform for studying the effects of *SCN2A* mutations in neuronal cells.

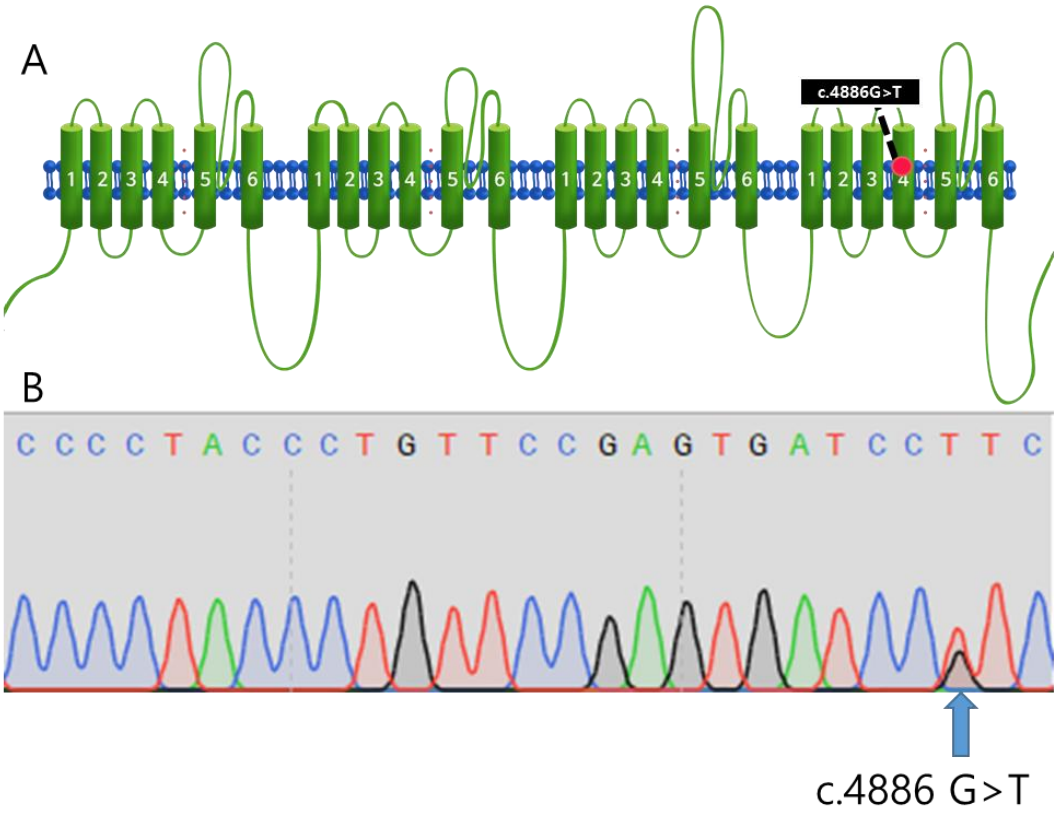

Figure 4. Amino acid sequence align map and location of the point mutation c.4886G>T (p.Arg1629Leu) on voltage-gated Sodium channel alpha Sub-unit 1.2(*SCN2A*). At S4DIV, positive Arginin residues are mutated to hydrophobic Leucine residues. When VSD4 is in its active form in the marine channel, R1 to R4 users appear to exist with minimal charge. (A) Cytogenetic location is 2q24.3 and p.Arg1629Leu is located in segment 4 of domain II (S4DII), S4DIII, and S4DIV, respectively. (B) Sanger Sequencing results, with the problem location identified by checking the data content.

Table 4. PCR Primer Seqeuncing of Mutation Locations of 2AMJH

Name	Primer Seqeunce (5` → 3`)	Tm(℃)	Base Pair (bp)
2AMJH 1 – F	TGT ACTTGG CCA CTG TAT GC	55.9	738 bp
2AMJH 1 – R	CCA ACA GAT GGG TTC CCA CA	58.8	

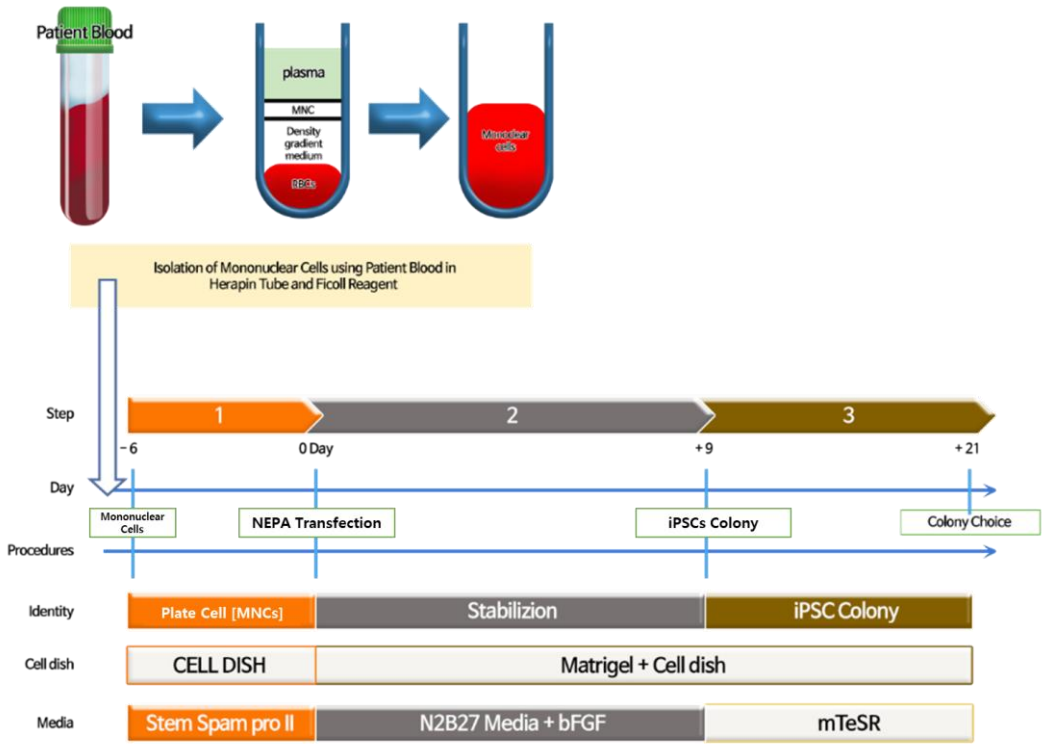

Figure 5 Timeline for building induced pluripotent stem cells using mononuclear cells obtained after Ficoll's taxonomy.

Table 5. Antibody of iPSCs Characterization

Antibody	Dilution	Company, Location, CAT No.
OCT4 Monoclonal Antibody	1:400	Invitrogen, Middlesex County, Massachusetts, United States #MA5-14845
Anti-Stage-Specific Embryonic Antigen-4 Antibody, clone MC-813-70	1:500	Merck Millipore, Burlington, Massachusetts, United States MAB4305
Anti-Nanog antibody	1:500	ABCAM, Cambridge, United Kingdom, #AB80892
Anti-TRA-1-81 Antibody, clone TRA-1-81	1:250	Merck Millipore, Burlington, Massachusetts, United States MAB4305
Anti-Sox2 Antibody	1:500	Merck Millipore, Burlington, Massachusetts, United States MAB4305
Anti-TRA-1-60 Antibody, clone TRA-1-60	1:250	Merck Millipore, Burlington, Massachusetts, United States MAB4360
Goat anti-Mouse IgG (H+L) Cross-Adsorbed Secondary Antibody, Alexa Fluor™ 568	1:500	Invitrogen, Middlesex County, Massachusetts, United States #A-11004
Goat anti-Rabbit IgG (H+L) Cross-Adsorbed Secondary Antibody, Alexa Fluor™ 488	1:500	Invitrogen, Middlesex County, Massachusetts, United States #A-11008

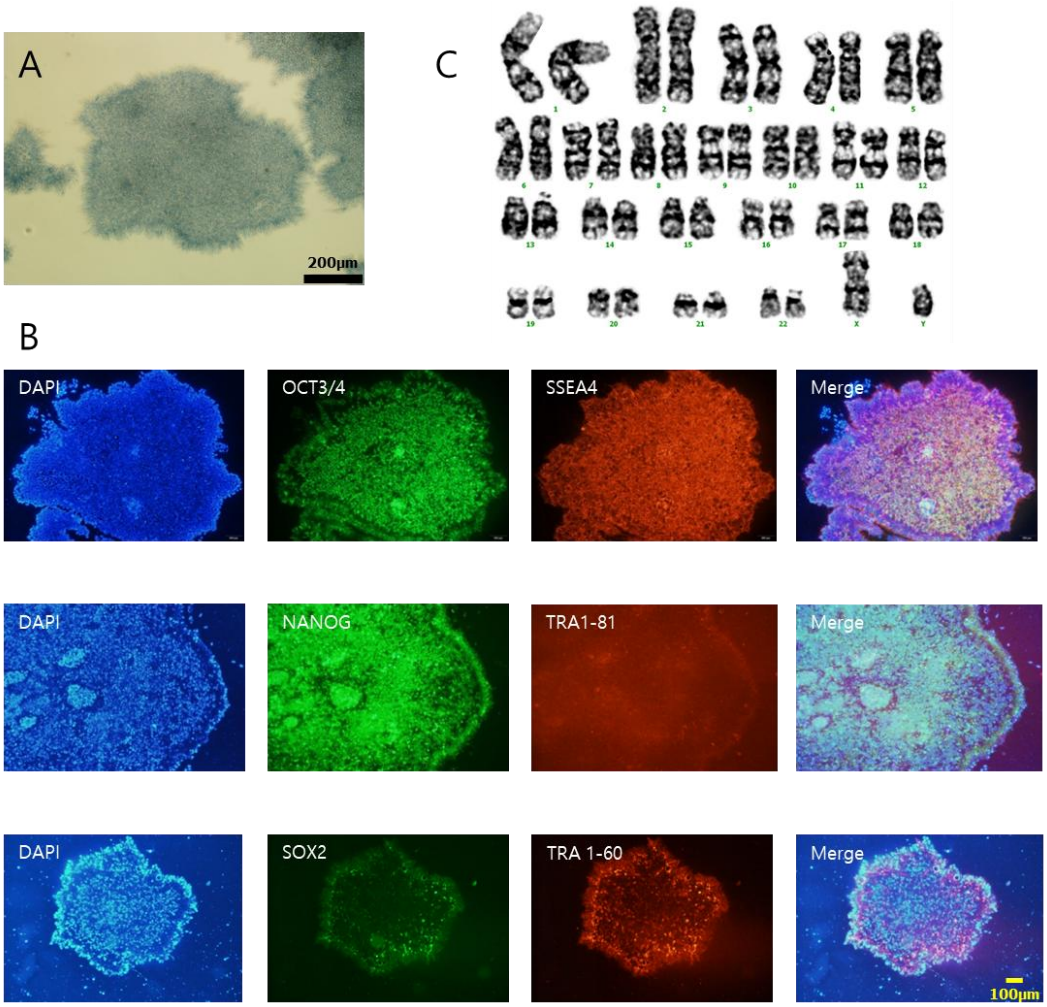

Figure 6. Induced pluripotent stem cells identity confirmed. (A) Phenotypic characterization of induced pluripotent stem cell differentiation was performed by measuring AP activity using Alkaline phosphatase staining. Scale Bar = 200 μm. (B) iPSC colonies from *SCN2A* patients expressed the pluripotency markers [OCT3/4, SSEA4], and [NANOG, TRA 1-81] and [SOX2, TRA 1-60]. Scale bar = 100μm. (C) Results of G-banding analysis of iPSCs karyotype.

A

Comparison	Reference				Sample				Number of Shared Alleles (Reference & Sample)
	P1-MNC				P1-A				
Marker	Allele 1	Allele 2	Allele 3	Allele 4	Allele 1	Allele 2	Allele 3	Allele 4	
AMEL	X	Y			X	Y			2
CSF1PO	10	12			10	12			2
D13S317	10	13			10	13			2
D16S539	11	12			11	12			2
D18S51	15				15				1
D19S433	14	14.2			14	14.2			2
D21S11	29	32.2			29	32.2			2
D2S1338	19	23			19	23			2
D3S1358	15				15				1
D5S818	9	12			9	12			2
D7S820	10	11			10	11			2
D8S1179	10	14			10	14			2
FGA	24	25			24	25			2
TH01	7	9			7	9			2
TPOX	11				11				1
vWA	14	19			14	19			2

Allele No.	Total # of Reference Allele (A)	Total # of Sample Allele (B)	Total # of Shared Allele (C)
	29	29	29

% Match	Match Algorithm = $\frac{C \times 2}{A + B}$	100.0%

Interpretation		
	(0-55 %)	This result is consistent with the two samples being unrelated (different donors)
	(56-79 %)	This result is indeterminant and may need further testing
	(80-100 %)	This result is consistent with the two samples being related (same donor)

Related (Same Donor)

B

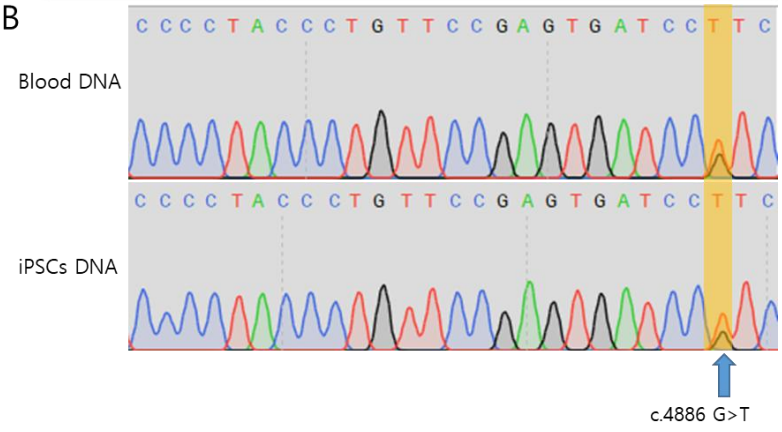

Figure 7. Results of STR analysis of *SCN2A* Patient's Mononuclear Cells and iPSCs derived *SCN2A* Patient. (A) Results of STR analysis of genes in *SCN2A* patient-derived iPSCs and *SCN2A* patient monocytes. (B) DNA from patient blood and DNA from patient-derived iPSCs were compared by Sanger Sequencing. They confirmed the presence of the same genetic mutations.

Table 6. Antibodies available for the three germ layers.

Antibody	Dilution	Company, Location, CAT No.
Recombinant Anti-PAX6 antibody	1:350	ABCAM, Cambridge, United Kingdom, #EPR15858
Anti-Tubulin Antibody, beta III isoform, CT, clone TU-20 (Similar to TUJ1)	1:500	Merck Millipore, Burlington, Massachusetts, United States MAB1637
Recombinant Anti-Brachyury / Bry antibody	1:1000	ABCAM, Cambridge, United Kingdom, #EPR18113
Alpha-Smooth Muscle Actin Monoclonal Antibody (1A4)	1:1000	Invitrogen, Middlesex County, Massachusetts, United States #14-9760-80
AFP Monoclonal Antibody (F1-6P2A8-P2B9A9)	1:200	Invitrogen, Middlesex County, Massachusetts, United States #MA5-14665
FOXA2 Recombinant Rabbit Monoclonal Antibody (9H5L7)	1:100	Invitrogen, Middlesex County, Massachusetts, United States #701698
Goat anti-Mouse IgG (H+L) Cross-Adsorbed Secondary Antibody, Alexa Fluor™ 568	1:500	Invitrogen, Middlesex County, Massachusetts, United States #A-11004
Goat anti-Rabbit IgG (H+L) Cross-Adsorbed Secondary Antibody, Alexa Fluor™ 488	1:500	Invitrogen, Middlesex County, Massachusetts, United States #A-11008

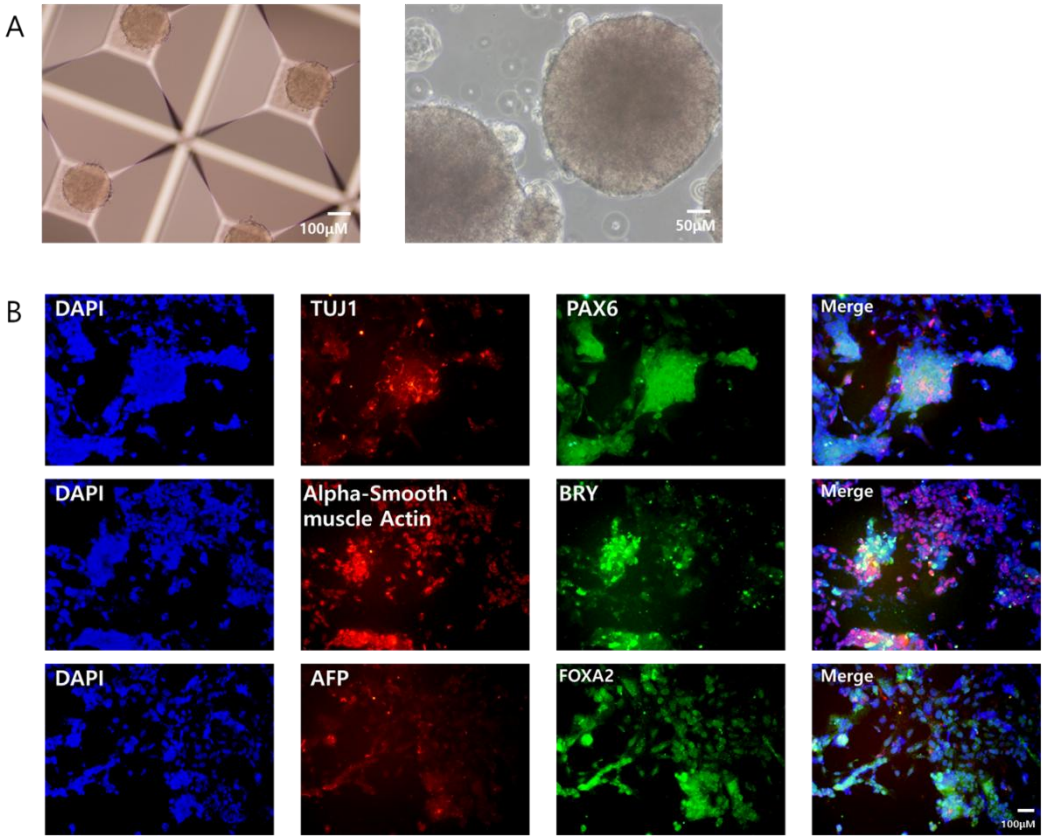

Figure 8. **Differentiation of *SCN2A* patient-derived iPSCs into derivatives of three germ layers.** (A) EB formation and morphology confirmed by microscopy.(Left Scale Bar =100μm,Right Scale Bar =50μm) (B) Immunochemistry results showed expression of three germ layer markers: TUJ1, PAX6 for ectoderm; alpha-SMA, brachyury for mesoderm; and FOXA2, AFP for endoderm. Scale bars = 100μm.

3.2. Identification of *SCN2A* Mutation and Gene Editing using CRISPR/Cas9 in iPSCs of *SCN2A* Patients

The *SCN2A* mutation in the current patient has been previously reported by several research teams, including the National Institutes of Health (NIH), which is one of the most reliable sources (https://www.ncbi.nlm.nih.gov/clinvar/RCV000818268.1/). This mutation has been documented as a missense mutation. The patient was reported to have experienced seizures starting at 4 days of age, which is consistent with the clinical presentation of early-onset epileptic encephalopathy (Table 3). According to previous studies, mutations with seizure onset earlier or later than 3 months are classified as gain-of-function or loss-of-function variants, though functional outcomes may vary depending on specific factors, as shown in Figure 9A.[32]

To investigate the mutation further, I used an ion channel mutation prediction system for sodium channels (https://funnc.shinyapps.io/shinyappweb/). The prediction indicated that the mutation caused a gain-of-function and was likely to affect excitatory neurons. The Receiver Operating Characteristic (ROC) score for the mutation's pathogenicity was 0.99, indicating a very high probability of being pathogenic, consistent with conventional NGS results. Other pathogenicity scores for the mutation included CADD = 28.9, PolyPhen = 0.92, and a gain-of-function probability of 0.55 (Figure 9C).

Given that the NGS information and the location of the genetic variant were consistent with previous findings, I proceeded with gene editing using CRISPR/Cas9. The single-guide RNA (sgRNA) was identified using the Benchling system and Merck CRISPR Design Tools (Figure 11B). In order to increase vector efficiency, I chose a method where both the sgRNA and Cas9 were combined into a single vector, rather than using separate vectors (Figure 10). This design was intended to improve the editing efficiency and reduce the possibility of incomplete editing.

To ensure efficient electroporation, I included puromycin as a selection marker and eGFP as an expression marker in the vector (Table 8, 9, Figure 10). This allowed for tracking the success of the CRISPR/Cas9 modification and the selection of successfully edited cells.

To facilitate homology-directed repair (HDR), I designed single-strand oligo deoxynucleotides (ssODN) using Merck CRISPR Tools to serve as the Donor template for the repair (Figure 11C). Electroporation was performed using the NEPA21 electroporation system, and two electroporation conditions were compared[86,87]: CCTEIp #2 (125V, 5 ms length, 50 ms interval, ± polarity) and CCTEIp #3 (150V, 5 ms length, 50 ms interval, ± polarity). Both conditions resulted in similar survival rates, but CCTEIp #2 showed higher eGFP expression and a better growth rate compared to CCTEIp #3 (Figure 12A-D).

After confirming eGFP expression, I treated the cells with puromycin for 3 days, which resulted in a significant difference in eGFP expression by the third day (Figure 12C-D), confirming the efficiency of the CRISPR/Cas9 editing. Following this, I cultured the cells for a week without puromycin to evaluate the stability of eGFP expression, and found that eGFP disappeared by day 7, confirming successful electroporation (Figure 12E).

Fluorescence Activated Cell Sorting (FACS) was performed on day 2, after electroporation, to isolate the successfully edited cells. Initially, I started with 2×10^6 cells and obtained 4×10^3 cells after sorting, resulting in a 500-fold loss. However, 99.4% of the sorted cells were eGFP-positive, indicating nearly complete CRISPR/Cas9 modification (Figure 13A-C). The remaining 0.6% of cells were further purified by puromycin selection for 2 days, after which I confirmed successful gene correction through Sanger sequencing (Figure 14A).

To minimize cell death during the gene editing process, I employed two compounds: pifithrin-alpha, a p53 inhibitor, and SCR7 pyrazine, an inhibitor of non-homologous end joining (NHEJ). I added 10 μM pifithrin-alpha for one day after editing to prevent p53-mediated apoptosis[88-94] (Figure 14B). Additionally, 1 μM SCR7 was added for 3 days to increase the efficiency of HDR and prevent unwanted DNA repair mechanisms such as NHEJ[95-98] (Figure 14B).

The entire gene editing process was successful, as confirmed by Sanger sequencing. Compared to the initial sequencing data, the desired mutation was accurately edited, and a silent mutation was introduced to prevent off-target effects (Figure 15).

Finally, to ensure that no off-target mutations occurred, I searched for potential off-target sites using Benchling and Cas-OFFinder. Sanger sequencing of the identified regions confirmed that no off-target mutations had occurred, verifying the specificity of the CRISPR/Cas9 editing (Table 9).

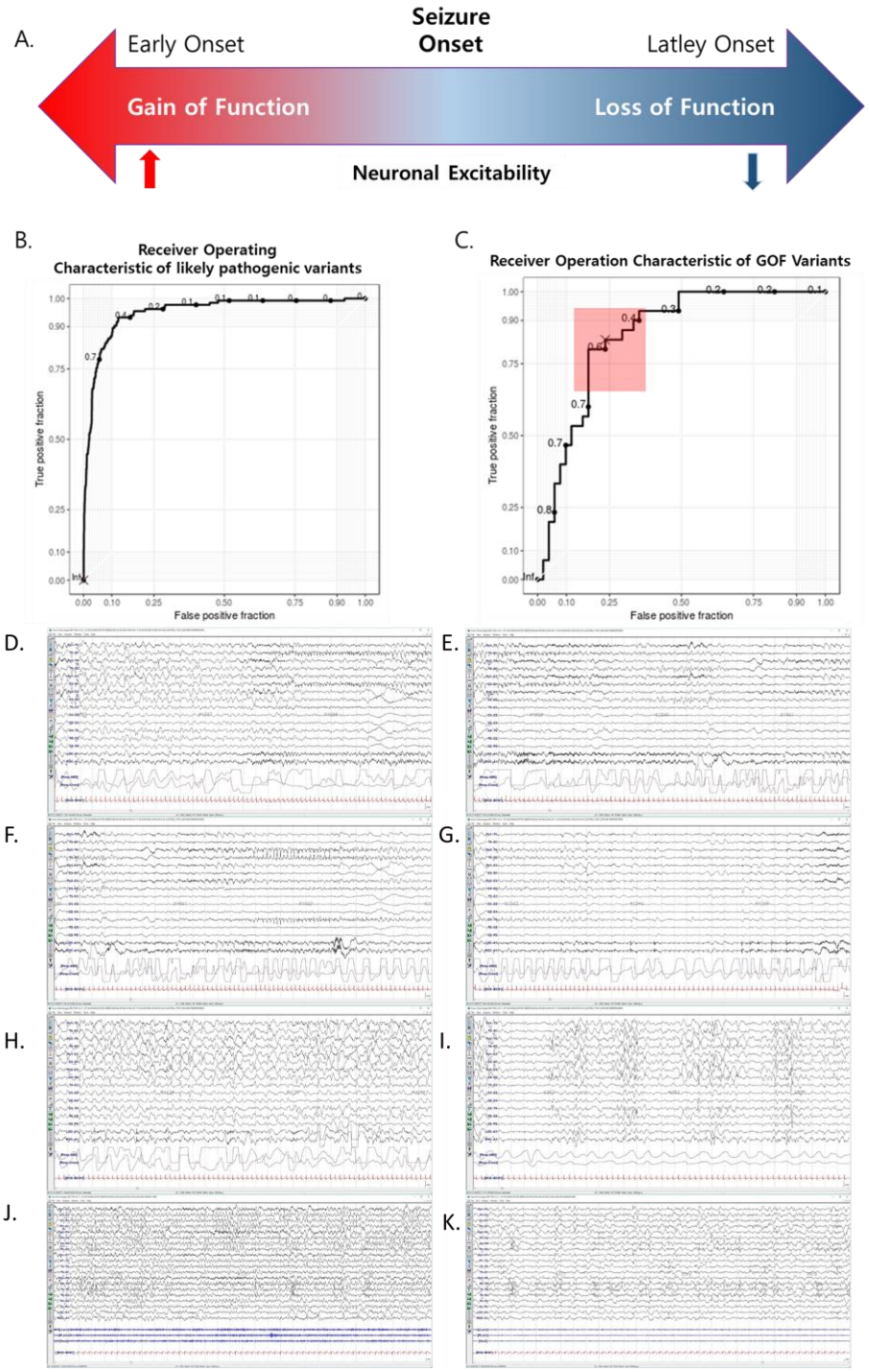

Figure 9. Measuring functional variability in patients. (A) Functional variability according to Seizure Onset (B) Operating Characteristic of likely pathogenic variants with ROC=0.95, Sensitivity=0.89, Specificity=0.9. (C) Receiver Operating Characteristic of GOF variants is ROC=0895, Sensitivity=0.83, Specificity=0.76. In this case, the value of Gain of Function is 0.55 with a likelihood of 0.55. (D) - (G) Electrographic seizure from Lt. Posterior Quadrant (Occipital dominancy) and Rt. Posterior Quadrant (Temporal dominancy). (D),(E) = Lt PQ, (F), (G) = Rt PQ. (H)-(I) slow and disorganized background with nearly contnuous multifocal sharp waves and multifocal polyspike activities, followed by brief generalized voltage attenuations, resembling burst-suppression pattern. (H) Slow and disorganized background with nearly contnuous multifocal sharp waves and multifocal polyspike activities. (I) Multifocal polyspike activities, followed by brief generalized voltage attenuations, resembling burst-suppression pattern. (J)-(K) slow and disorganized background and very frequent multifocal epileptiform discharges. (J) Awake, (K) Asleep.

Table 7. Vector Components

Name	Position	Size (bp)	Type	Description	Application notes
U6 promoter	1-249	249	Promoter	Human U6 small nuclear 1 promoter	Pol III promoter; drives expression of small RNAs.
(gRNA)	251-346	96	gRNA	[TCCGAGTGATCCTTCTTGCCGTTTTAGAGCTAGAAATAGCAAGTTAAAATAAGGCTAGTCCGTTATCAACTTGAAAAAGTGGCACCGAGTCGGTGC] *SCN2A* Patient Mutation location	None
Terminator	347-352	6	terminator	Pol III transcription terminator	Allows transcription termination of small RNA transcribed by Pol III RNA polymerase.
CBh promoter	366-1163	798	Promoter	CMV early enhancer fused to modified chicken β-actin promoter	Strong promoter.
hCas9	1176-5447	4272	CDS	Human codon-optimized CRISPR associated protein 9 from Streptococcus pyogenes (with 3xFLAG tag and nuclear localization signal), also known as SpCas9	Generates double-strand DNA breaks.
BGH pA	5478-5685	208	PolyA_signal	Bovine growth hormone polyadenylation signal	Allows transcription termination and polyadenylation of mRNA transcribed by Pol II RNA polymerase.
CMV promoter	5697-6284	588	Promoter	Human cytomegalovirus immediate early enhancer/promoter	Strong promoter; may have variable strength in some cell types.
EGFP/Puro	6316-7632	1317	CDS	EGFP fused with Puro	Allows cells to be visualized by green fluorescence and resistant to puromycin.
SV40 late pA	7636-7857	222	PolyA_signal	Simian virus 40 late polyadenylation signal	Allows transcription termination and polyadenylation of mRNA transcribed by Pol II RNA polymerase.
AmpiciIlin	8923-9783	861	CDS	AmpiciIlin resistance gene	Allows E. coli to be resistant to ampiciIlin.
pUC ori	9954-10542	589	Rep_origin	pUC origin of replication	Facilitates plasmid replication in E. coli; regulates high-copy plasmid number (500-700).

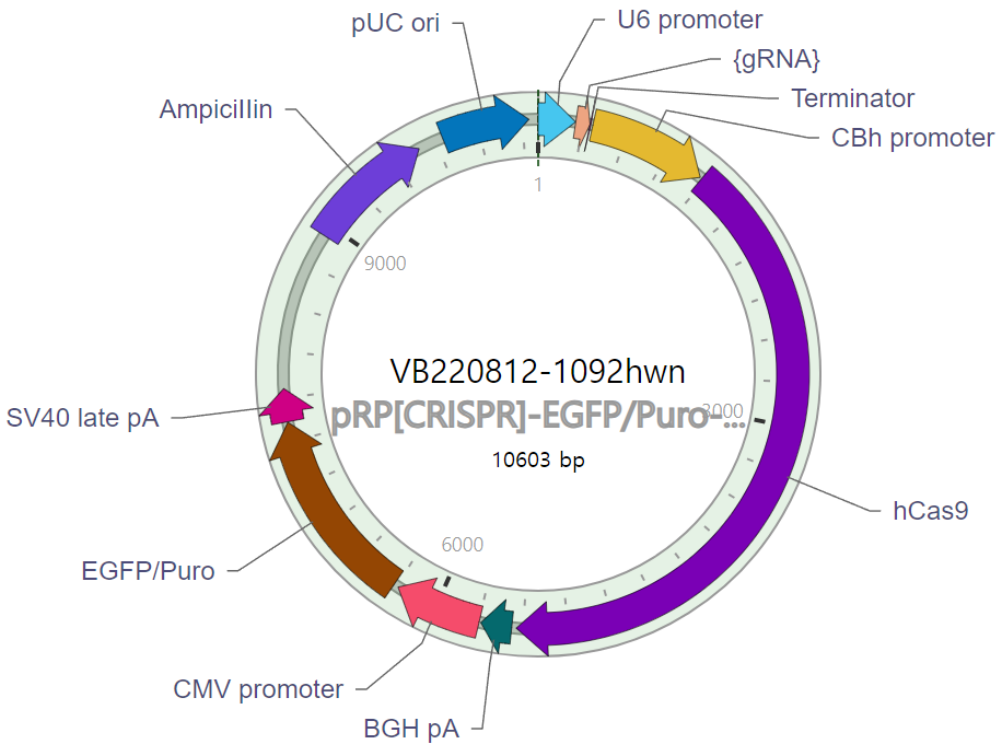

Figure 10. **CRISPR/CAS9 Vector Design.** gRNA and hCAS9 are attached and the selection marker is EGFP/Anti Puro. The total length is 10603 bp.

Table 8. Summary of CRISPR/CAS9 Vector Information

Title	Information
Vector ID:	VB220812-1092hwn
Vector Name:	pRP[CRISPR]-EGFP/Puro-hCas9-U6>(gRNA)
Vector Type:	Mammalian CRISPR Vector (Single gRNA) Guide
Vector Size:	10603 bp
gRNA:	(gRNA)
Guide Sequence:	TCCGAGTGATCCTTCTTGCC
Nuclease:	hCas9
Marker:	EGFP/Puro
Plasmid Copy Number:	High
Antibiotic Resistance:	Ampicillin

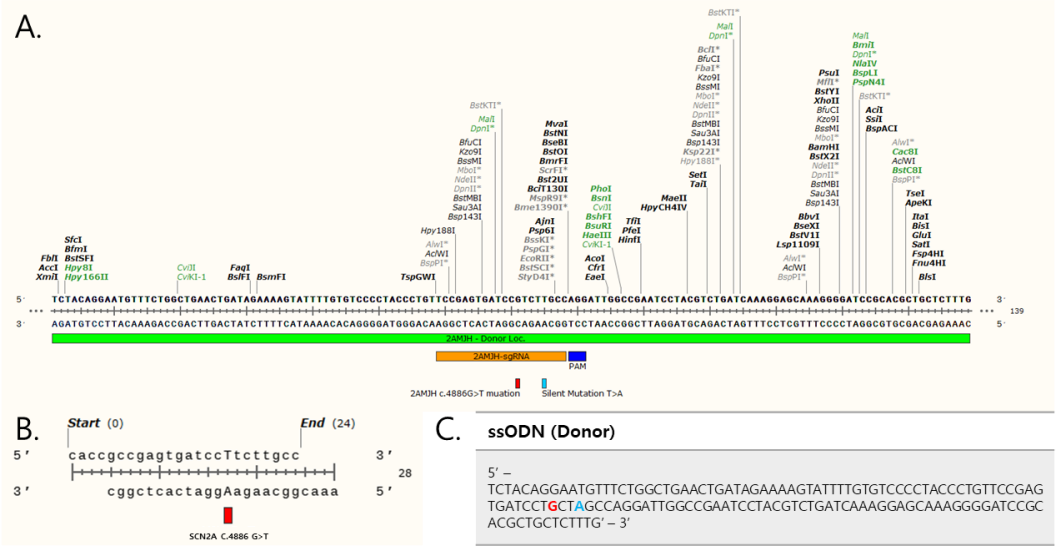

Figure 11. Gene Editing Design. (A) Gene editing total schematic of *SCN2A* patient (B) gudie RNA position (C) ssODN (Donor) position Sequencing.

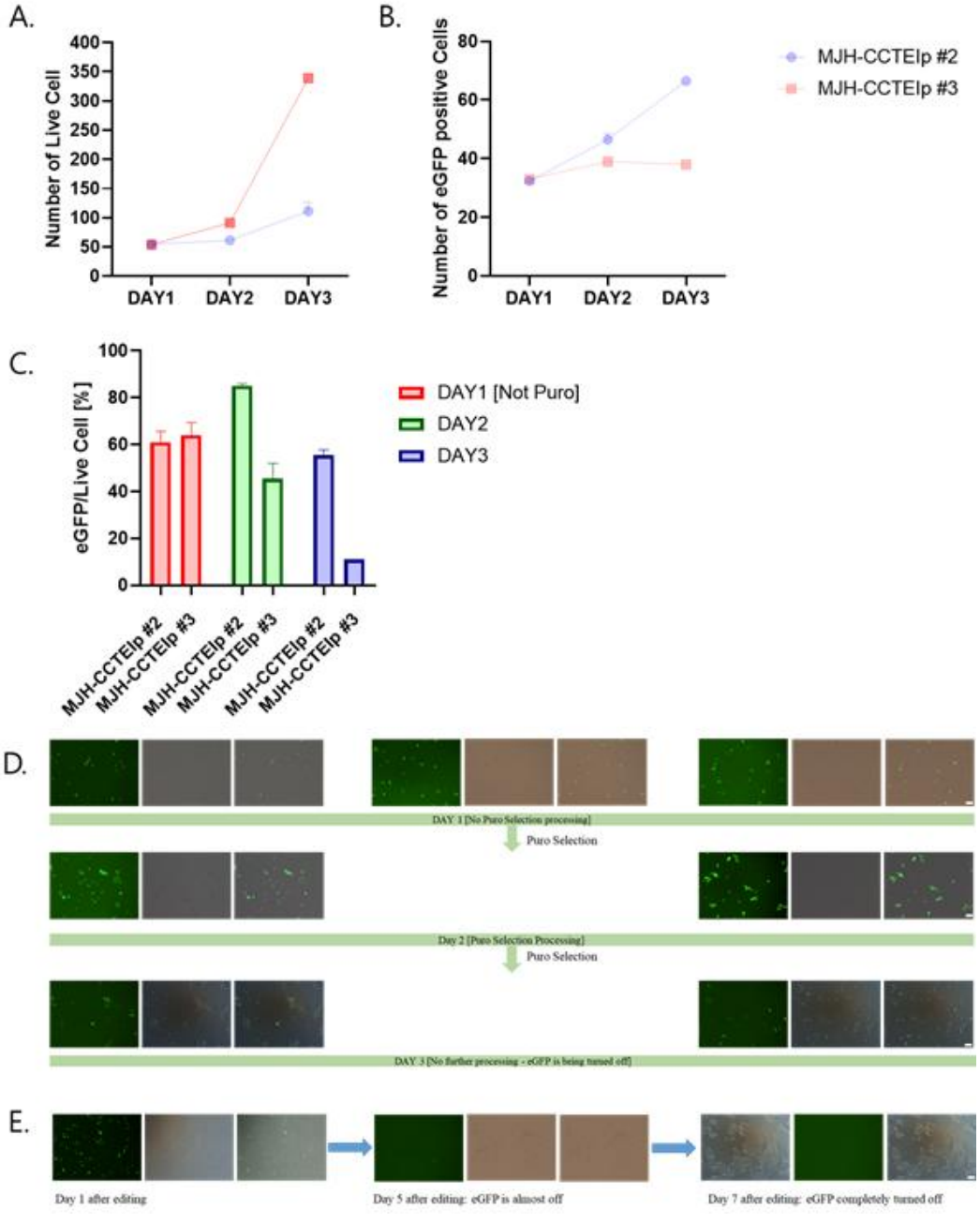

Figure 12. Gene Editing Efficacy Screening. (A) Change curve of Live Cells according to editing efficacy by duration. (B) Change curve of eGFP Positive cells according to editing efficacy by duration. (C) Comparison of efficacy according to voltage applied to electroporation. CCTEIp #2 and #3 were edited with different voltages. For CCTEIp #2, the following values were adopted: 125 Voltage, 5 Length, 50 Interval, 2 No. 10 Drate, +/- Polarity. CCTEIp#3 was evaluated with 150 Voltage, 5 Length, 50 Interval, 2 No. 10 Drate, +/- Polarity. The results were calculated from the results of A and B, and the % of Puro mycin in the amount of Positive eGFP generated by Live Cells was measured. (D) Cell growth rate was compared by measuring electroporation in two ways. The growth rate of the cells was measured by viewing them by brightfield microscopy. The expression of eGFP was measured by viewing with fluorescence microscopy. (Scale bar = 100 μm). (E) Check the end date of the operation after CRISPR/CAS9 treatment. Most of the cells were turned off at about day 5, so they were all turned off by 1 week. In conclusion, CRISPR/CAS9 was turned off after 1 week of operation.

A.

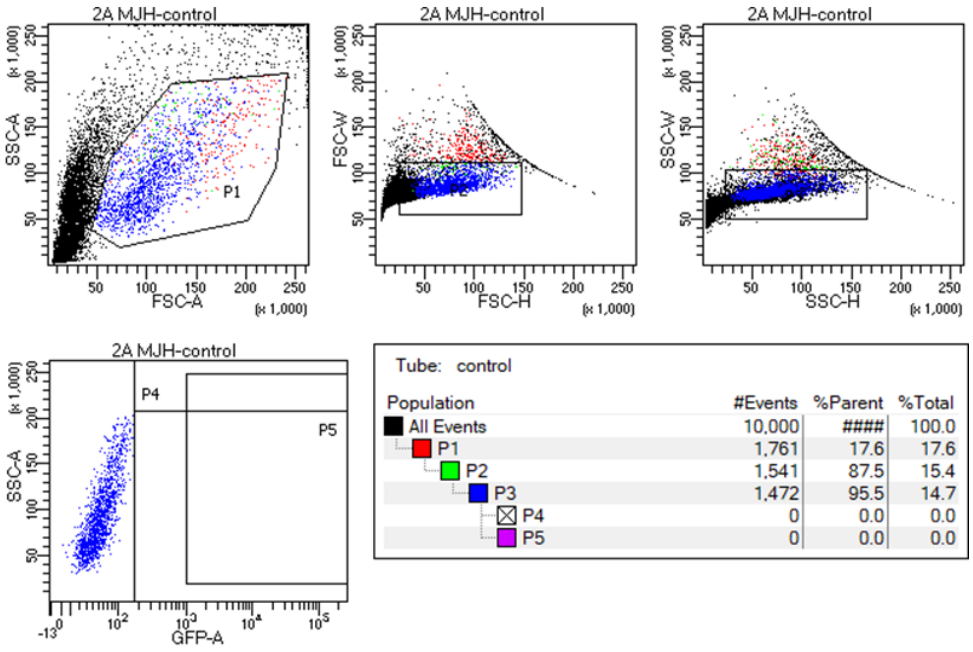

Tube: control

Population	#Events	%Parent	%Total
All Events	10,000	####	100.0
P1	1,761	17.6	17.6
P2	1,541	87.5	15.4
P3	1,472	95.5	14.7
P4	0	0.0	0.0
P5	0	0.0	0.0

B.

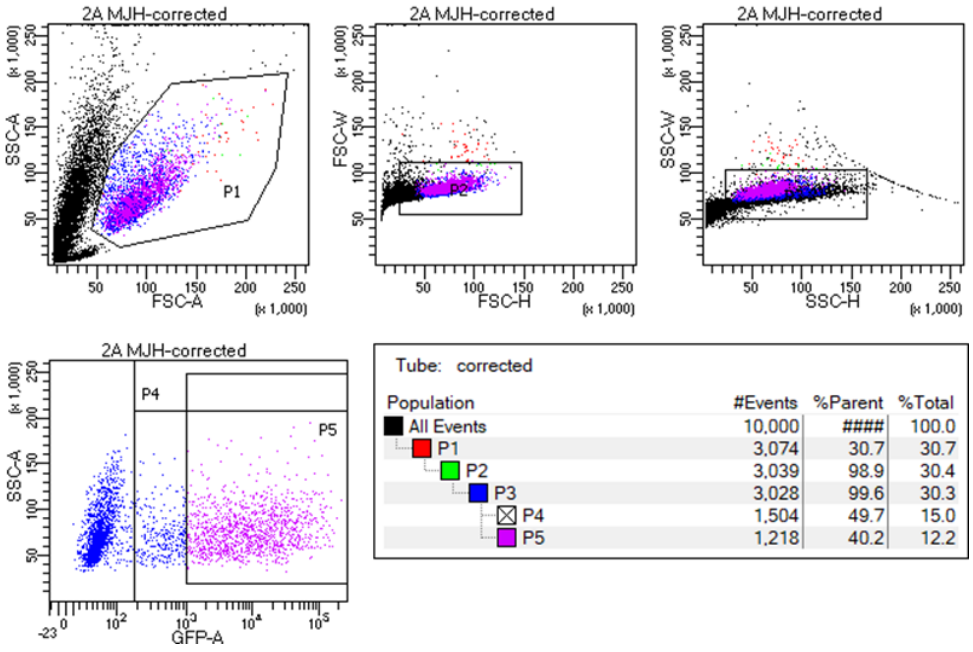

Tube: corrected

Population	#Events	%Parent	%Total
All Events	10,000	####	100.0
P1	3,074	30.7	30.7
P2	3,039	98.9	30.4
P3	3,028	99.6	30.3
P4	1,504	49.7	15.0
P5	1,218	40.2	12.2

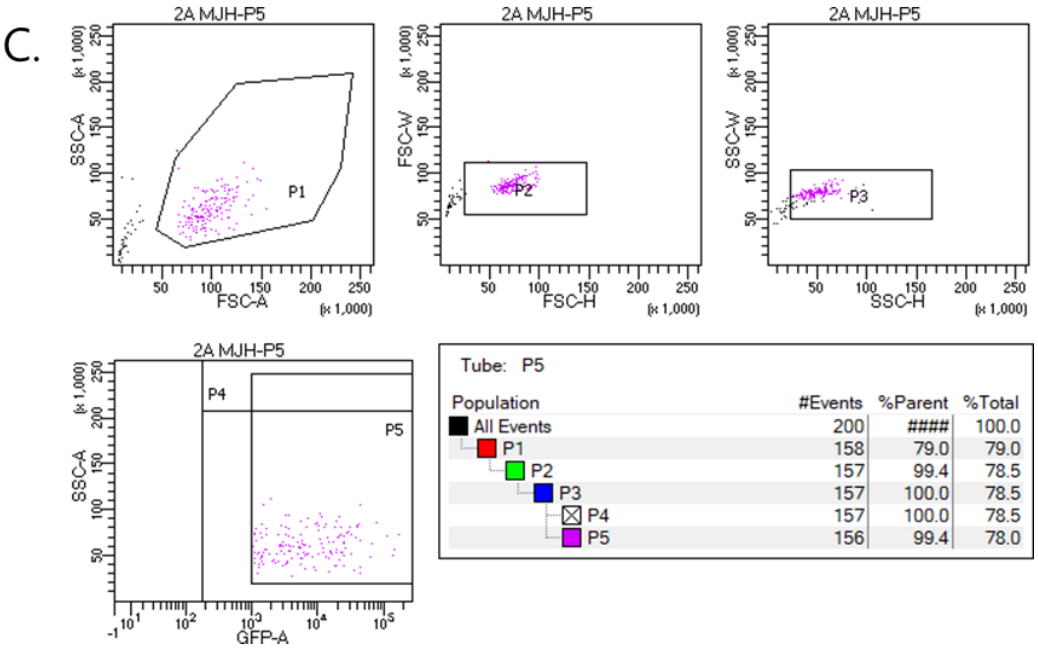

Figure 13 Calibrated cell sorting via Fluorescence Activated Cell Sorter (FACS). (A) Primary sorting was performed to categorize live cells compared to control cell lines. (B) Secondary sorting was performed to sort cells expressing eGFP. (C) Final sorting of cells.

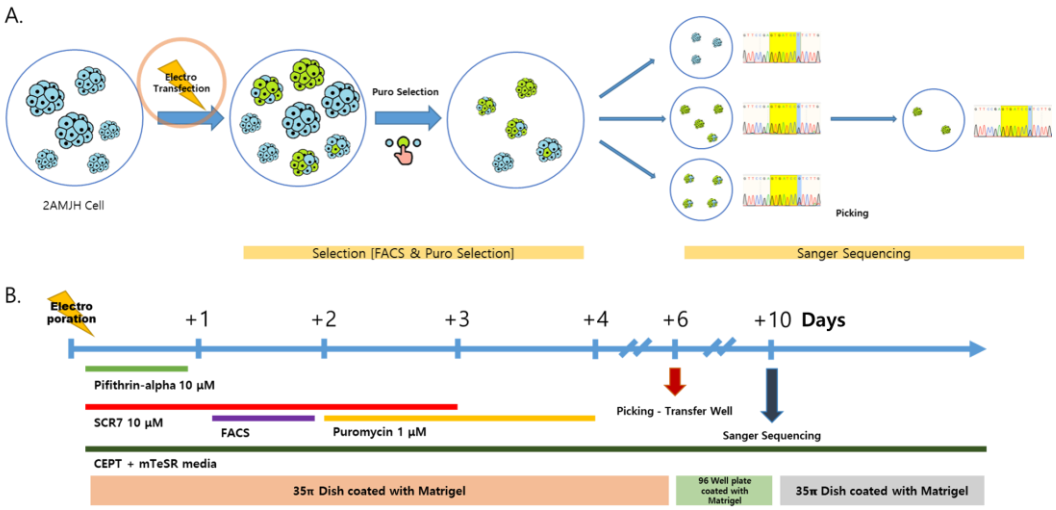

Figure 14 Schematic of the complete experiment method design using CRISPR/CAS9. (A) Schematic of the genetic editing using CRISPR/CAS9. (B) Time-Line of the total CRISPR/CAS9 research. Factors required for cell culture. Green line: Pifithirin-alpha 10μM used to prevent apoptosis of cells by p53, Red line: SCR7 10μM used to increase HDR efficiency, Purple line: FACS used area, Yellow line: Anti-puro used to finally select non-edited cells that were not selected in FACS. Orange and Gray Bars: Culture in 35π dish coated with Matrigel, Green Bar: Culture in 96Well plate coated with Matrigel. Red Arrow : Subculture by picking cells into Trans Wells. Navy Arrow: Sanger Sequencing Progress Date.

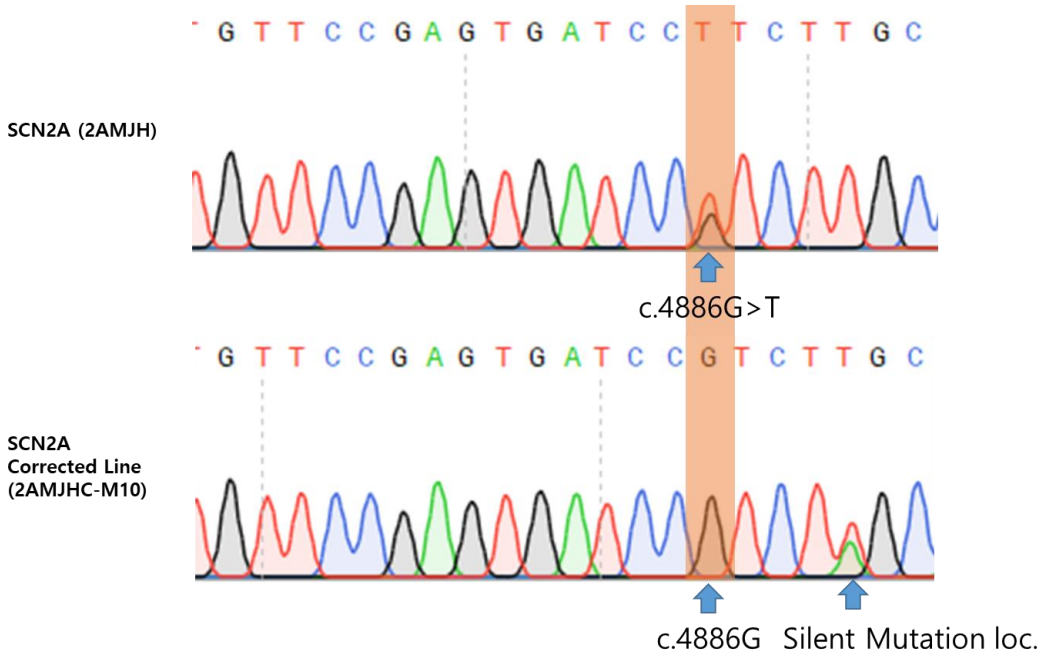

Figure 15. Sanger Sequencing results show that the gene editing was successful using CRISPR/CAS9. c.4886G>T was successfully corrected in the heterozygote line and a silent mutation occurred.

Table 9. Off-Target Location Check and Whole Genome Sequencing

Sequence	PAM	Score	Gene	Chromosome	Strand	Position	Mismatches	On-target
TCCGAGTGATCCGTCTTGCC	AGG	100	ENSG00000169432	chr2	-1	166199797	0	FALSE
TCCGAGTGATCCGTCTTGCC	AGG	100	ENSG00000136531	chr2	1	165388697	0	TRUE
TCCGAGTGATCCGTCTTGCC	AGG	100	ENSG00000153253	chr2	-1	165091278	0	FALSE
TCCGAGTGATCCGTCTTGCT	AGG	41.7	ENSG00000144285	chr2	-1	165992355	1	FALSE

> On-target position / sequence

Chromosome	Position	Sequence	Strand	Mismatches	Gene / Region
chr2	165,388,679	TCCGAGTGATCCgTCTTGCC(AGG)	+	1	SCN2A / exon

> Off-target position / sequence

Chromosome	Position	Sequence	Strand	Mismatches	Gene / Region
chr2	165,091,271	TCCGAGTGATCCgTCTTGCC(AGG)	-	1	SCN3A / exon
chr2	166,199,790	TCCGAGTGATCCgTCTTGCC(AGG)	-	1	SCN1A-AS1 / exon
chr2	165,992,348	TCCGAGTGATCCgTCTTGCt(AGG)	-	2	SCN1A-AS1 / exon
chr8	143,158,466	aCCGAGTGATCCTTCcTGCC(TGG)	+	2	LY6H / exon
chr7	47,666,501	gCCGAGTGAgCCTTCTTGCa(CGG)	+	3	- / intergenic
chr13	57,262,921	TCtGAGTGtTCCTTgTTGCC(AGG)	-	3	- / intergenic
chrX	27,505,584	TCCcAGTGATCCTTgTTtCC(TGG)	+	3	- / intergenic

Table 10. OFF-Target Locations by sgRNA Sequence [Primer seqeuce Information]

Name	Primer Seqeunce (5` → 3`)	Tm(℃)	Base Pair (bp)
2AMJH – OT3 - *SCN1A* - ENSG00000144285 - F	AGG ACT CTG AAC CTT ACC TTG G	57.1	465bp
2AMJH – OT3 - *SCN1A* - ENSG00000144285 - R	GTC GGG TGG CTT ACT GTT GA	58.6	
2AMJH – OT2 - *SCN3A* - ENSG00000153253 - F	GGC CCA TTT CTC TCT AAC TGA AG	56.1	547bp
2AMJH – OT2 - *SCN3A* - ENSG00000153253 - R	AAA CAA CGC AGG AAG GGA CA	58.2	
2AMJH – OT1 *SCN9A*-ENSG00000169492 –F	GTT TAG AGT CAT CAT TTC AGG TAG C	53.7	412bp
2AMJH – OT1 *SCN9A*-ENSG00000169492 –R	TGC TAG CAA TCC ATC CCA GC	58.9	

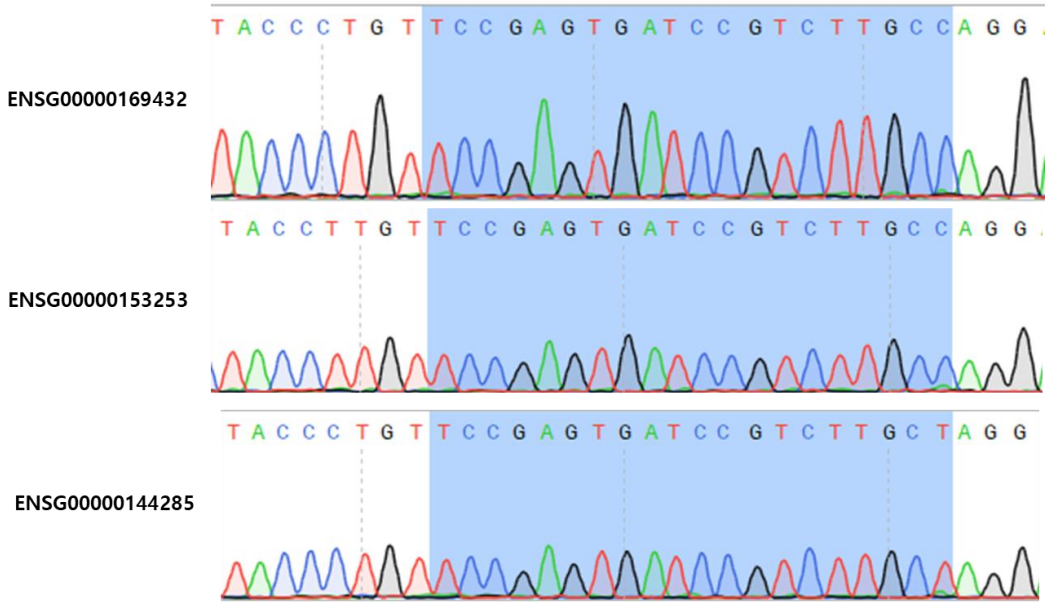

Figure 16. Identification of off-target positions similar to sgRNA sequences for genes. Sequences with less than 3 mismatches were checked according to the score. This means that OFF-Target did not exist.

3.3. Differentiation of Excitatory Neurons and Inhibitory Neurons in *SCN2A* Patients

One of the key features of *SCN2A* patients is their heightened susceptibility to epilepsy, which is why it is essential to study patient-derived neurons to better understand epilepsy. Induced pluripotent stem cells (iPSCs) provide a valuable tool in this research, as they can be differentiated into patient-specific neurons. While spontaneous differentiation can be induced by adjusting the culture conditions, this method often leads to a mix of neuron types, which is not ideal when specific neuronal populations need to be generated. Therefore, to achieve a more controlled differentiation process, I employed Lenti-Virus-based methods, as outlined in prominent studies in *Nature* and *Cell*[44-48] (Figure 17A, 17B).

To generate inhibitory GABAergic neurons, I used Lenti-Virus to overexpress ASCL1 and DLX2 transcription factors, known to drive the differentiation of iPSCs into inhibitory neurons[44,46,48] (Figure 17A, Table 11). Similarly, excitatory glutamatergic neurons were generated by overexpressing NGN2 using Lenti-Virus[45,47,48] (Figure 17B, Table 12, 13). However, this method involved the use of multiple viruses, which not only increased the viral titer but also posed challenges in terms of cell toxicity and efficiency due to the lack of selection markers. To address this, the Lenti-Virus system was redesigned by combining ASCL1 and DLX2 into a single vector, which significantly minimized cell damage caused by using multiple viruses and enhanced overall differentiation efficiency (Table 11, 12).

Additionally, the redesigned Lenti-Virus system allowed for the incorporation of fluorescent markers without separately adding them, solving the titer issue and increasing efficiency. By using a single virus, inhibitory neurons that previously required three viruses could now be differentiated efficiently with just one. This improvement reduced the need for individual selection markers like puromycin and hygromycin, which often damage cells during the selection process. These optimizations ensured a higher survival rate and effective differentiation into inhibitory neurons (Figure 17A, 17B, Table 11-14).

To further optimize the efficiency of viral infection, I used a Tet-On system, enabling precise control of viral expression using Doxycycline (DOX). Cells were treated with 2 μg/mL DOX and subsequently puromycin for three days to filter out uninfected cells. Additionally, to prevent the proliferation of non-neuronal cells such as fibroblasts and astrocytes, Cytarabine (ara-C) was introduced. Ara-C inhibits non-neuronal cell proliferation, ensuring a cleaner neuronal culture.

To support neuronal survival and growth, several factors were added to the culture environment. Brain-Derived Neurotrophic Factor (BDNF) and Glia-Derived Neurotrophic Factor (GDNF) were included to enhance neuronal maturation, and ascorbic acid was added to improve cellular activity.

To increase synaptic efficiency and intracellular cAMP levels, dibutyryl cyclic-AMP (dbcAMP) was introduced.[99-101] dbcAMP is a cell-permeable compound that activates cAMP pathways, but it often requires high concentrations for effective intracellular activity. To overcome this, Forskolin, a diterpene that directly activates adenylyl cyclase, was added to further increase intracellular cAMP levels. Forskolin enhances cAMP production, which is critical for activating protein kinase A (PKA) and improving neuronal differentiation efficiency[82,83] .

After 12 days of differentiation, the neurons were co-cultured with astrocytes to mimic the forebrain cortex environment, promoting neuronal maturation (Figure 18A). Astrocyte co-culture has been shown to enhance neuronal maturity more effectively than using Astrocyte Conditioned Media (ACM) alone. For electrophysiological analysis, I employed two methods: Micro Electrode Array (MEA). In the MEA setup, GABAergic and glutamatergic neurons were co-cultured at a 3:7 ratio, simulating the natural neuronal environment, while astrocytes were cultured with neurons at a 1:1 ratio to optimize cellular density (Figure 18B).

Neuronal maturation was observed over a period of 3 to 6 weeks.(Figure 19) Specific markers for GABAergic neurons, such as GAD67, and glutamatergic neurons, such as vGluT2, became detectable at around week 3. PCR and real-time PCR confirmed the presence and activity of these markers, indicating successful differentiation and maturation. These findings validated the functionality of the redesigned Lenti-Virus system and affirmed its effectiveness in generating both excitatory and inhibitory neurons from *SCN2A* patient-derived iPSCs (Figure 19B, Table 17). The histogram illustrates the distribution of Trough-Peak duration for putative inhibitory (red) and putative excitatory (green) neuron units. The red bars represent the inhibitory neurons (likely corresponding to FS units), which predominantly show shorter Trough-Peak durations (<0.5 ms). The green bars represent excitatory neurons (likely corresponding to RS units), which show longer Trough-Peak durations, typically exceeding 0.5 ms[102]. The bins are set at 0.1 ms intervals, allowing for a detailed representation of the duration distribution for each neuron type. (Figure 19C). Figure 19D shows the PCR products obtained using specific primers for each neuron type. The products correspond to GAPDH (194bp), GAD67 (301bp), and vGluT2 (130bp), which represent different gene markers used to identify distinct neuronal subtypes. (Table 17).

A

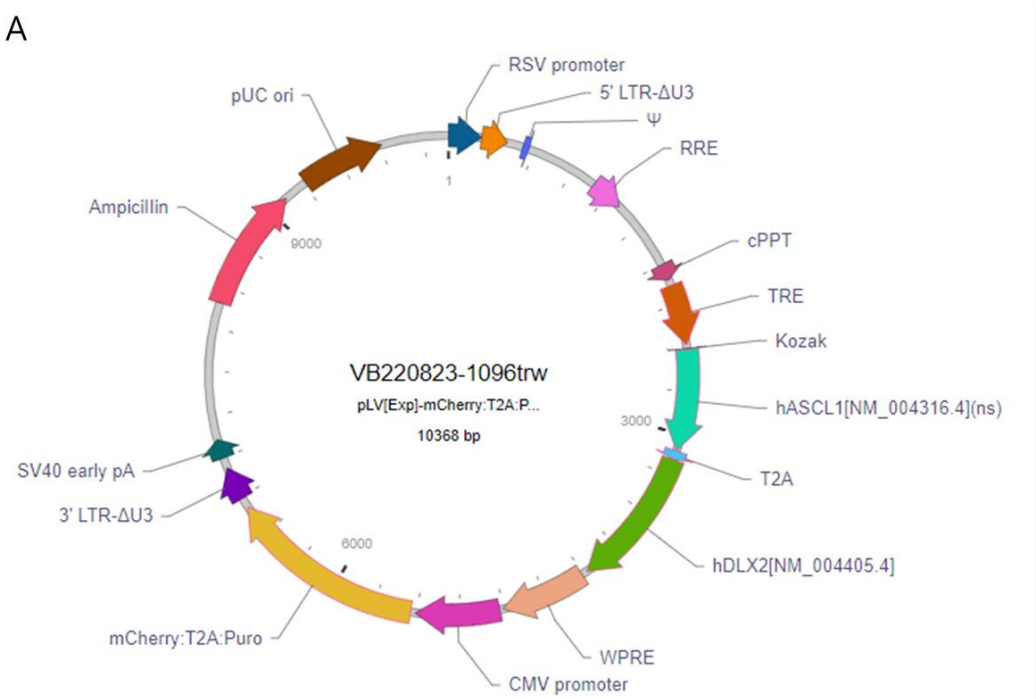

B

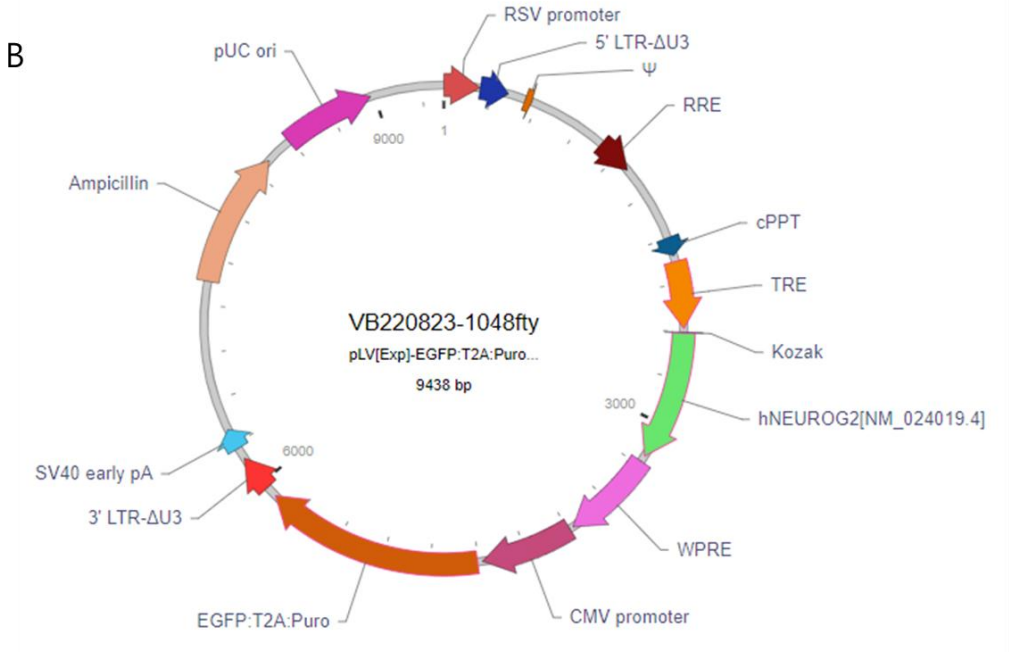

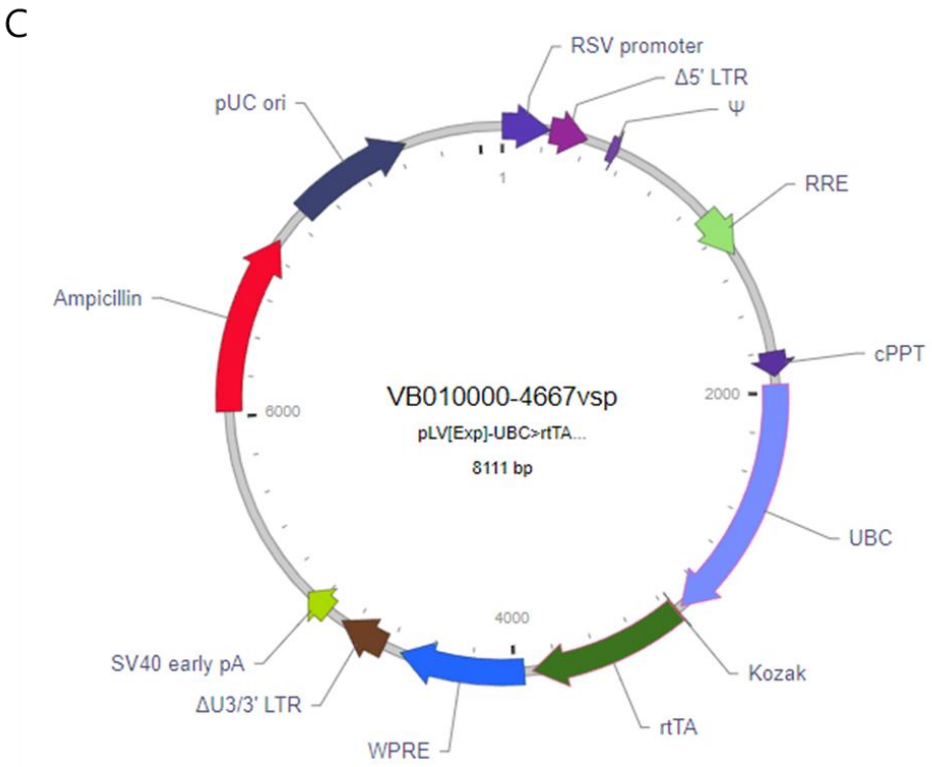

Figure 17 Lenti Virus design. (A) Tet-on-based Lenti-Virus is specialized to contain both hASCL1 and hDLX2. It is also featured by the inclusion of mCherry and Anti-Puro as selection markers. It is designed to increase the efficiency of Lenti Virus. Through this, differentiation into GABAergic Neuron is possible. (B) Tet-on-based Lenti-Virus is characterized by the inclusion of NGN and selection markers eGFP and Anti-Puro. It was designed to increase the efficiency of Lenti Virus. This allows differentiation into Glutamatergic Neuron. (C) In order to differentiate into GABAergic Neuron and Glutamatergic Neuron, (A) and (B) are Tet-On-based Lenti-Virus, so rtTA was redesigned to make the virus function.

Table 11. Information about Lenti-Virus (ASCL1+DLX2)

Name	Position	Size (bp)	Type	Description	Application notes
RSV promoter	1-229	229	Promoter	Rous sarcoma virus enhancer/promoter	Strong promoter; drives transcription of viral RNA in packaging cells.
Δ5' LTR	230-410	181	LTR	Truncated HIV-1 5' long terminal repeat	Allows transcription of viral RNA and its packaging into virus.
Ψ	521-565	45	Miscellaneous	HIV-1 packaging signal	Allows packaging of viral RNA into virus.
RRE	1075-1308	234	Miscellaneous	HIV-1 Rev response element	Rev protein binding site that allows Rev-dependent nuclear export of viral RNA during viral packaging.
cPPT	1803-1920	118	Miscellaneous	Central polypurine tract	Facilitates the nuclear import of HIV-1 cDNA through a central DNA flap.
EF1A	1959-3137	1179	Promoter	Human eukaryotic translation elongation factor 1 α1 promoter	Strong promoter.
Kozak	3162-3167	6	Miscellaneous	Kozak	Facilitates translation initiation.
mCherry	3168-3878	711	CDS	Variant of mRFP1 generated by mutagenesis	Commonly used red fluorescent protein; fast maturation compared to its predecessor, mRFP1.
WPRE	3917-4514	598	Miscellaneous	Woodchuck hepatitis virus posttranscriptional regulatory element	Enhances viral RNA stability in packaging cells, leading to higher titer of packaged virus.
CMV promoter	4536-5123	588	Promoter	Human cytomegalovirus immediate early enhancer/promoter	Strong promoter; may have variable strength in some cell types.
EGFP:T2A:Puro	5155-6534	1380	CDS	EGFP and Puro linked by T2A	Allows cells to be visualized by green fluorescence and resistant to puromycin.
ΔU3/3' LTR	6605-6839	235	LTR	Truncated HIV-1 3' long terminal repeat	Allows packaging of viral RNA into virus; self-inactivates the 5' LTR by a copying mechanism during viral genome integration; contains polyadenylation signal for transcription termination.
SV40 early pA	6912-7046	135	PolyA_signal	Simian virus 40 early polyadenylation signal	Allows transcription termination and polyadenylation of mRNA transcribed by Pol II RNA polymerase.
Ampicillin	8000-8860	861	CDS	Ampicillin resistance gene	Allows E. coli to be resistant to ampicillin.
pUC ori	9031-9619	589	Replication_origin	pUC origin of replication	Facilitates plasmid replication in E. coli; regulates high-copy plasmid number (500-700).

Table 12. Lenti-virus (ASCL1+DLX2) summary

Title	Information
Vector ID:	VB220823-1096trw
Vector Name:	pLV[Exp]-mCherry:T2A:Puro-TRE>hASCL1[NM_004316.4](ns):T2A:hDLX2[NM_004405.4]
Vector Type:	Mammalian Tet Inducible Gene Expression Lentiviral Vector
Vector Size:	10368 bp
Viral Genome Size:	6893 bp
Promotoer:	TRE
ORF:	hASCL1[NM_004316.4](ns), hDLX2[NM_004405.4]
Linker:	T2A
Marker:	mCherry:T2A:Puro
Plasmid Copy Number:	High
Antibiotic Resistance:	Ampicillin

Table 13. Information about Lenti-Virus (NGN2)

Name	Position	Size (bp)	Type	Description	Application notes
RSV promoter	1-229	229	Promoter	Rous sarcoma virus enhancer/promoter	Strong promoter; drives transcription of viral RNA in packaging cells.
5' LTR-ΔU3	230-410	181	LTR	Truncated HIV-1 5' long terminal repeat	Allows transcription of viral RNA and its packaging into virus.
Ψ	521-565	45	Miscellaneous	HIV-1 packaging signal	Allows packaging of viral RNA into virus.
RRE	1075-1308	234	Miscellaneous	HIV-1 Rev response element	Rev protein binding site that allows Rev-dependent nuclear export of viral RNA during viral packaging.
cPPT	1803-1920	118	Miscellaneous	Central polypurine tract	Facilitates the nuclear import of HIV-1 cDNA through a central DNA flap.
TRE	1959-2382	424	Promoter	Tetracycline-responsive element promoter (2nd generation)	Regulated by a class of transcription factors (e.g. tTA, rtTA and tTS) whose activities are dependent on tetracycline or its analogs (e.g. doxycycline).
Kozak	2407-2412	6	Miscellaneous	Kozak translation initiation sequence	Facilitates translation initiation of ATG start codon downstream of the Kozak sequence.
hNEUROG2[NM_024019.4]	2413-3231	819	CDS	*None*	*None*
WPRE	3270-3867	598	Miscellaneous	Woodchuck hepatitis virus posttranscriptional regulatory element	Enhances virus stability in packaging cells, leading to higher titer of packaged virus; enhances higher expression of transgenes.
CMV promoter	3889-4476	588	Promoter	Human cytomegalovirus immediate early enhancer/promoter.	Strong promoter; may have variable strength in some cell types.
EGFP:T2A:Puro	4508-5887	1380	CDS	EGFP and Puro linked by T2A	Allows cells to be visualized by green fluorescence and resistant to puromycin.
3' LTR-ΔU3	5958-6192	235	LTR	Truncated HIV-1 3' long terminal repeat	Allows packaging of viral RNA into virus; self-inactivates the 5' LTR by a copying mechanism during viral genome integration; contains polyadenylation signal for transcription termination.
SV40 early pA	6265-6399	135	PolyA_signal	Simian virus 40 early polyadenylation signal	Allows transcription termination and polyadenylation of mRNA transcribed by Pol II RNA polymerase.
AmpiciIIin	7353-8213	861	CDS	AmpiciIIin resistance gene	Allows E. coli to be resistant to ampiciIIin.
pUC ori	8384-8972	589	Rep_origin	pUC origin of replication	Facilitates plasmid replication in E. coli; regulates high-copy plasmid number (500-700).

Table 14. Lenti-virus (NGN2) summary

Title	Information
Vector ID:	VB220823-1048fty
Vector Name:	pLV[Exp]-EGFP:T2A:Puro-TRE >hNEUROG2[NM_024019.4]
Vector Type:	Mammalian Tet Inducible Gene Expression Lentiviral Vector
Vector Size:	9438 bp
Viral Genome Size:	5963 bp
Promotoer:	TRE
ORF:	hNEUROG2[NM_024019.4]
Marker:	EGFP:T2A:Puro
Plasmid Copy Number:	High
Antibiotic Resistance:	Ampicillin

Table 15. Information about Lenti-Virus (rtTA)

Name	Position	Size (bp)	Type	Description	Application notes
RSV promoter	1-229	229	Promoter	Rous sarcoma virus enhancer/promoter	Strong promoter; drives transcription of viral RNA in packaging cells.
Δ5' LTR	230-410	181	LTR	Truncated HIV-1 5' long terminal repeat	Allows transcription of viral RNA and its packaging into virus.
Ψ	521-565	45	Miscellaneous	HIV-1 packaging signal	Allows packaging of viral RNA into virus.
RRE	1075-1308	234	Miscellaneous	HIV-1 Rev response element	Rev protein binding site that allows Rev-dependent nuclear export of viral RNA during viral packaging.
cPPT	1803-1920	118	Miscellaneous	Central polypurine tract	Facilitates the nuclear import of HIV-1 cDNA through a central DNA flap.
UBC	1959-3136	1178	Promoter	Human ubiquitin C promoter	Weak promoter.
Kozak	3161-3166	6	Miscellaneous	Kozak translation initiation sequence	Facilitates translation initiation of ATG start codon downstream of the Kozak sequence.
rtTA	3167-3913	747	CDS	Reverse tetracycline responsive transcriptional activator M2 (2nd generation)	It binds to TRE promoter to activate gene transcription only in the presence of tetracycline or its analogs (e.g. doxycycline). It has higher sensitivity to the inducing drug and lower leaky activity in the absence of the drug compared to its predecessor, rtTA.
WPRE	3952-4549	598	Miscellaneous	Woodchuck hepatitis virus posttranscriptional regulatory element	Enhances virus stability in packaging cells, leading to higher titer of packaged virus; enhances higher expression of transgenes.
ΔU3/3' LTR	4631-4865	235	LTR	Truncated HIV-1 3' long terminal repeat	Allows packaging of viral RNA into virus; self-inactivates the 5' LTR by a copying mechanism during viral genome integration; contains polyadenylation signal for transcription termination.
SV40 early pA	4938-5072	135	PolyA_signal	Simian virus 40 early polyadenylation signal	Allows transcription termination and polyadenylation of mRNA transcribed by Pol II RNA polymerase.
Ampicillin	6026-6886	861	CDS	Ampicillin resistance gene	Allows E. coli to be resistant to ampicillin.
pUC ori	7057-7645	589	Rep_origin	pUC origin of replication	Facilitates plasmid replication in E. coli; regulates high-copy plasmid number (500-700).

Table 16. Lenti-virus (rtTA) summary

Title	Information
Vector ID:	VB010000-4667vsp
Vector Name:	pLV[Exp]-UBC>rtTA
Vector Type:	Tet Regulatory Protein Expression Lentiviral Vector
Vector Size:	8111 bp
Viral Genome Size:	4636 bp
Promotoer:	UBC
ORF:	rtTA
Plasmid Copy Number:	High
Antibiotic Resistance:	Ampicillin

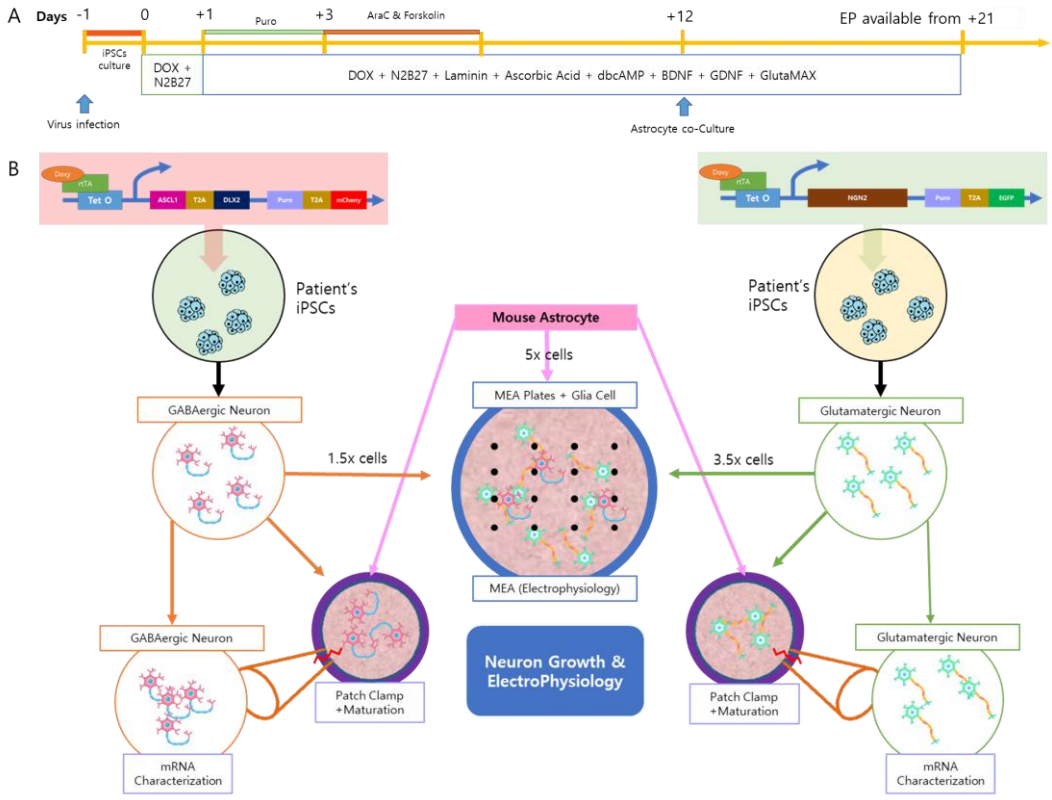

Figure 18. Illustration of neuronal differentiation time line and neuronal application scheme. (A) The process of differentiation of iPSCs into neurons. (B) Overall utilization and utilization plan using differentiated neurons.

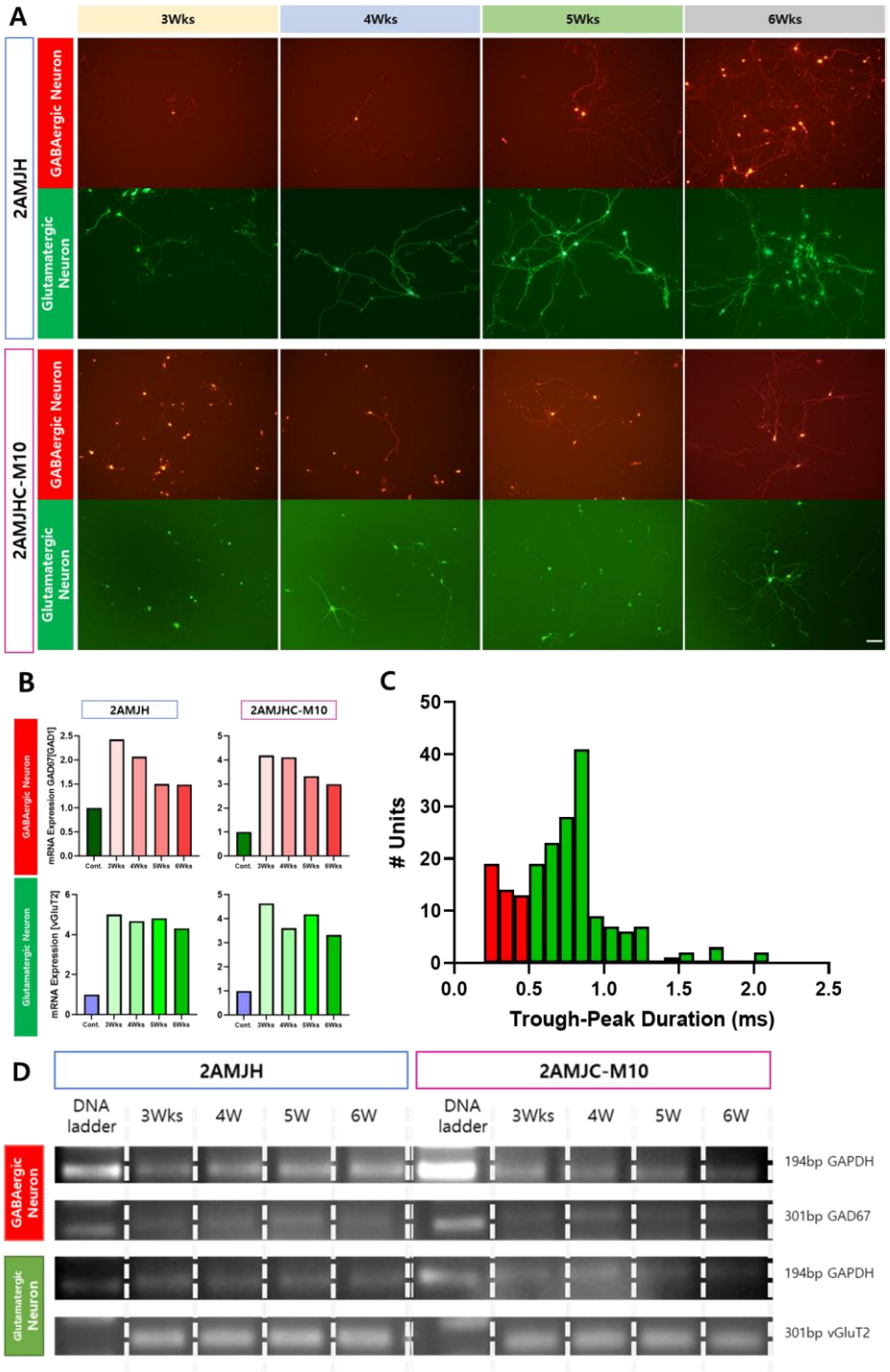

Figure 19 Post-differentiation neurons growth process and neurons proof process: (A) After virus infection, the growth process of 3 weeks, 4 weeks, 5 weeks, 6 weeks was photographed at the time of Doxycyclin treatment. . (Scale bar = 100 μm) (B) Each neurons growth process at 3, 4, 5, 6 weeks were isolated as single cells and then measured for mRNA expression by Real time PCR. [2AMJH - GABAergic Neuron [GAD67] : 3Wks - 2.43, 4Wks - 2.07, 5Wks - 1.50, 6Wks - 1.48, 7Wks - 1.45 / 2AMJHC - GABAergic Neuron [GAD67] : 3Wks - 4. 19, 4Wks - 4.11, 5Wks - 1.37, 6Wks - 2.99 / 2AMJH - Glutamatergic Neuron [vGluT2] : 3Wks - 5. 01, 4Wks - 4.68, 5Wks - 8.82, 6Wks - 4.31 / 2AMJHC - Glutamatergic Neuron [vGluT2] : 3Wks - 4.64, 4Wks - 3.61, 5Wks - 4.19, 6Wks - 3.33] (C) Histogram plots of the Trough-Peak duration (ms) : Putative-inhibitory Neuron (Red) and Putative-extatory Neuron (Green) units from all units. Bins = 0.1 ms. (D) The PCR product resulted from the specific primers of each neuron. [GAPDH: 194bp / GAD67: 301bp / vGluT2: 130bp]

Table 17. Neuron primer list targeting cDNAs

Name	Primer Seqeunce (5` → 3`)	Tm(℃)	Base Pair (bp)
GAPDH – F	GTA CAT GAC AAG GTG CGG CTC	60.3	194bp
GAPDH - R	CAC ATG GCC TCC AAG GAG TAA	58.2	
GAD67 – F	CTC CAA GGA TGC AAC CAG AT	55.4	301bp
GAD67 - R	CCC TGA GGC TTT GTG GAA TA	55.4	
vGluT2 - F	TGG TCG TTG GCT ATT CTC ATA C	55.1	130bp
vGluT2 - R	ATA CTG GCA TAT CTT GGA GCG	55.3	

3.4. Comparative Analysis of *SCN2A* Patient Neurons and Genetically Corrected Neurons

To further understand the effects of the *SCN2A* mutation on neuronal activity, I compared the differentiated neurons from *SCN2A* patients with those derived from genetically corrected iPSCs. Using the MEA system, I compared the electrophysiological properties of the two neuron types over a period of 3, 4, and 5 weeks. The comparison was initiated after the neurons had matured for 3 weeks (Figure 20-21). After culturing for three weeks, spontaneous neuronal network activity was recorded using MEA, and the differences between patient-derived and isogenic neurons became evident (Figure 20).

At week 3, patient-derived neurons exhibited significantly higher activity compared to isogenic neurons, as evidenced by heat map distributions and firing rates (Figure 21A1,B1,C1). The Mean Firing Rate (MFR) of patient neurons was approximately 10 times higher than that of isogenic neurons (SEM : -0.2237 ± 0.03284). By week 5, this difference increased, with patient neurons showing an MFR of 1.765 Hz, which was 2.5 times higher than that of isogenic neurons (-1.055 ± 0.3699, $p \leq 0.0065$). These findings indicate that neuronal excitability becomes increasingly divergent as the differentiation period extends (Figure 21C1).

I also analyzed Burst Metrics, including Burst Frequency, Burst Duration and Burst Percentage metrics. Burst Duration at week 3 did not show a significant difference, but by weeks 4 and 5, patient neurons exhibited longer and more frequent bursts compared to isogenic neurons (Figure 21A2-A4,21B2-B4,21C2-C4). Burst Percentage at week 5 was significantly different ($p<0.0001$), indicating altered firing regularity in patient-derived neurons. This suggests that *SCN2A* mutations lead to heightened excitability and prolonged neuronal activity, contributing to the epileptic phenotype.

Furthermore, Network Burst Metrics revealed significant differences in synchronization and burst coordination between patient and isogenic neurons. Network bursts were defined as synchronized bursts across multiple electrodes, with a threshold of 35% electrode participation (Figure 21A5,6,21B5,6,21C5,6). At week 3, the network burst frequency showed only minor differences, but by weeks 4 and 5, patient neurons exhibited markedly higher network burst frequencies and durations ($p \leq 0.0001$, Figure 21A5,B5,C5). This indicates increased synchronization among patient-derived neurons, which is a hallmark of epileptic network behavior.

Synchrony Metrics further confirmed these observations. Synchrony, calculated as the cross-correlation of spikes across electrodes, was significantly higher in patient neurons than in isogenic neurons, especially at week 5. This suggests that the *SCN2A* mutation leads to abnormal neuronal synchronization(Figure 21A7,B7,C7), contributing to network hyperexcitability.

These findings collectively demonstrate that *SCN2A* mutations significantly alter neuronal activity and network dynamics. The increased MFR, burst synchronization, and network burst coordination observed in patient-derived neurons provide critical insights into the pathophysiology of *SCN2A*-related epilepsy, underscoring the need for targeted therapeutic interventions.

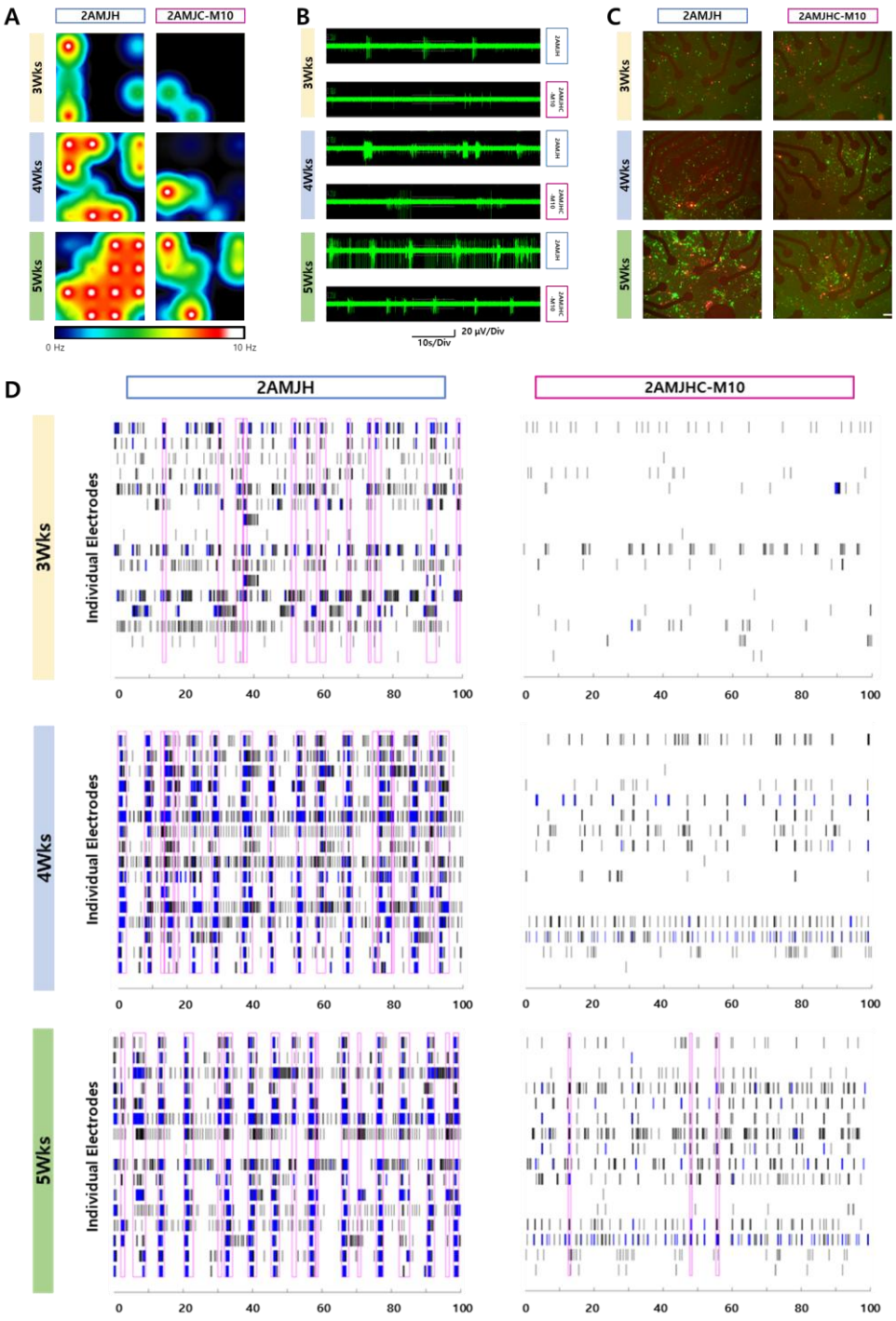

Figure 20. Increased network excitability revealed by MEA recordings of hiPSC-derived neurons harboring the c.4886G>T[p.Arg1629Leu] variant. (A) A heat map of neuron firing. The intensity of firing frequency is color-coded as follows. Warm colors (white, red, orange, yellow) represent high firing frequency and cool colors (green, blue) represent low firing frequency. Each color circle represents an active electrode. (B) Representative control and native spikes from neuron culture of the c.4886G>T [p.Arg1629Leu]. Each spike represents a spontaneous activity event. (C) Well-plated MEA with hiPSC-derived neurons. (Scale bar = 100 μm) (D) A representative spike raster plot that was generated for the isogenic control and p.Arg1629Leu cultures. Each row represents a spike recorded from one electrode for 100 seconds, with each tick representing a spontaneous event. The bursting events are shown as clusters of ticks in blue. Purple colored events show network bursts.

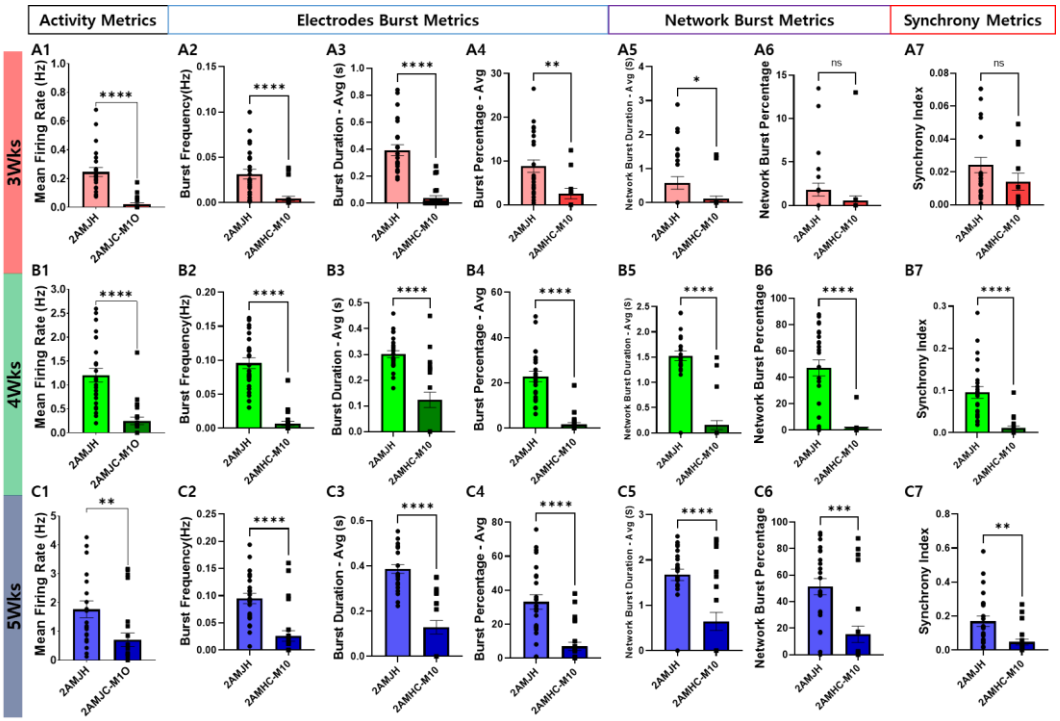

Figure 21. Differences in Activity Metrics Between *SCN2A* Patient-Derived Neurons (2AMJH) and Isogenic Neurons (2AMJHC-M10; 2AMJHC). (A1)-(A7) are measured at 3Weeks. (B1)-(B7) are measured at 4Weeks. (C1)-(C7) are measured at 5Weeks. (A1,B1,C1) Mean Firing Rate (Hz). (A2,B2,C2) Burst Frequency (Hz). (A3,B3,C3) Burst Duration – Avg(s). (A4,B4,C4) Burst Percentage - Avg. (A5,B5,C5) Network Burst Duration -Avg(s). (A6,B6,C6) Network Burst Percentage. (A7,B7,C7) Synchrony Index. N = 24, *:p≤0.05, **:p≤0.01, ***:p≤0.001, ****: p≤0.0001

3.5. Analysis of Extracellular Spike Waveforms

The analysis of neural spike data recorded from the Patient Line and Isogenic Line reveals significant differences in neural activity, emphasizing the functional impact of *SCN2A* mutations on neuronal dynamics. Neural spike data was processed using the Plexon Offline Sorter, which clustered waveforms based on distinctive features. Individual spike waveforms are illustrated as gray traces in Figures 22A and 22E, with the red line representing their mean waveforms. In the Patient Line, significant variability in spike width and irregular clustering patterns were observed, reflecting heterogeneous neuronal activity and network instability. Conversely, the Isogenic Line demonstrated more uniform spike width and consistent clustering, indicative of stable neuronal behavior. Clustered waveforms (Figures 22B and 22F) highlight these differences. In the Patient Line, broader spike widths and more dispersed clustering patterns were observed in the yellow cluster, suggesting heightened activity in specific neuronal populations. The green cluster exhibited slightly more stable but still irregular activity. In contrast, the Isogenic Line displayed minimal variability across all clusters, highlighting its uniform and stable behavior. Principal Component Analysis (PCA) revealed distinct clustering dynamics between the two lines. In the Patient Line, clusters were widely dispersed, highlighting irregular and heterogeneous neuronal activity. On the other hand, the Isogenic Line displayed tightly grouped clusters, indicative of consistent and stable baseline neuronal behavior. Histograms of spike occurrences provided further insights. The Patient Line exhibited concentrated spike occurrences within specific intervals in the yellow cluster, reflecting irregular and burst-like activity patterns, while the green cluster showed a more even distribution with occasional variability. In contrast, the Isogenic Line displayed uniform spike occurrence frequencies across both clusters, emphasizing stable and synchronized neuronal activity. The Patient Line displayed fundamentally altered neuronal dynamics characterized by irregular firing patterns, enhanced excitability, and disrupted burst synchronization. These abnormalities were particularly evident in the increased variability of mean firing rates, elevated burst frequencies, and irregular network burst patterns. Such changes are likely driven by *SCN2A* mutations, which impair normal neuronal regulation. This study highlights the pathological mechanisms underlying *SCN2A*-related disorders and provides a foundation for therapeutic development aimed at restoring stable neuronal activity.

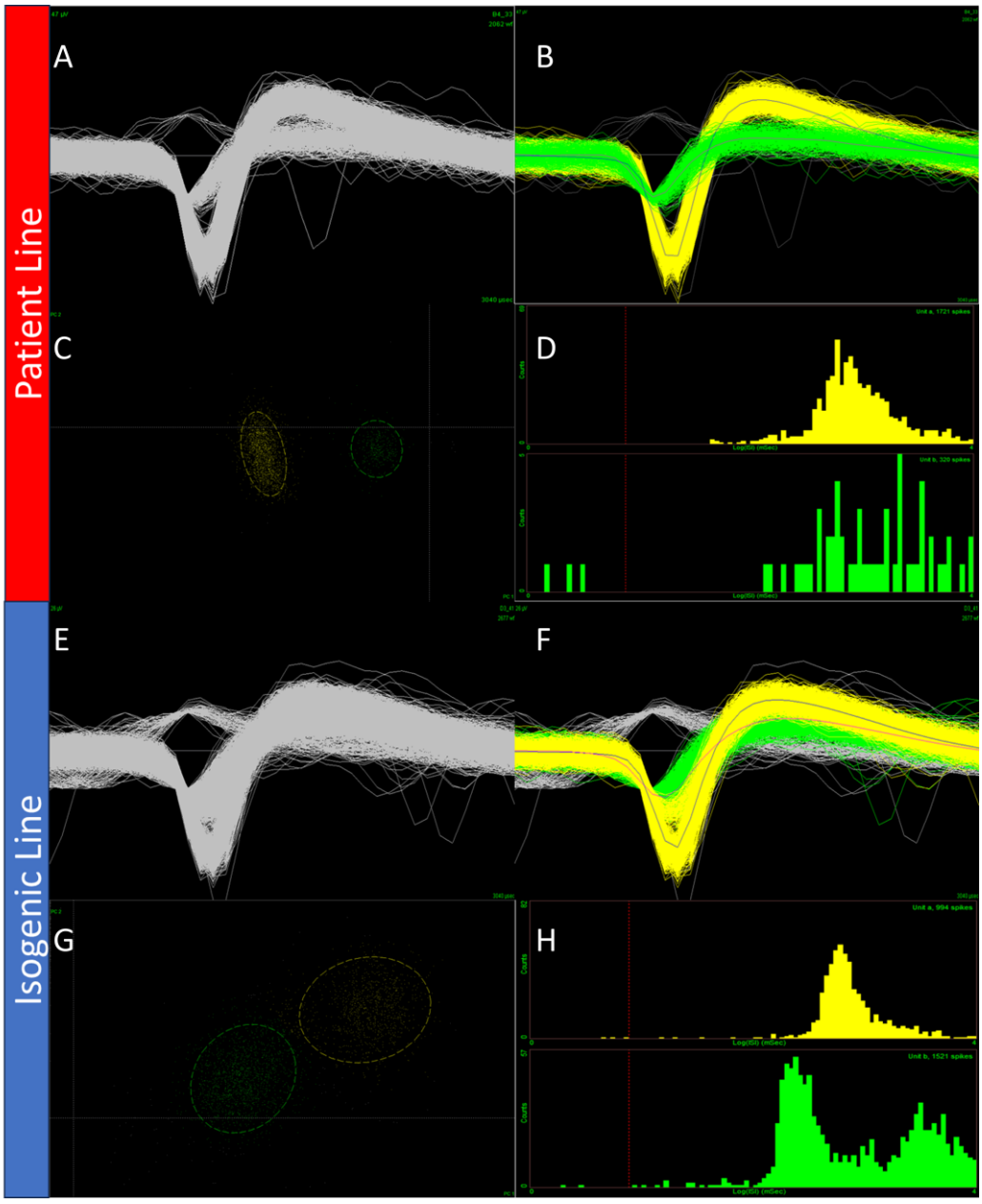

Figure 22 Spike waveform and clustering analysis for Patient Line(A-F) and Isogenic Line(G-H). (A, E) Individual spike waveforms (gray lines) recorded from the Patient Line and Isogenic Line, respectively. (B, F) Cluster-specific spike waveforms for the Patient Line and Isogenic Line. (C, G) Two-dimensional clustering of spikes using Principal Component Analysis (PCA). (D, H) Histograms of spike occurrence frequencies for each cluster.

3.6. Frequency-Based Well- and Probe-Level Analysis in *SCN2A* Patient Line

The analysis of neural activity recorded from the Patient Line focused on both Well-level and Probe-level frequency dynamics, providing insights into neuronal behavior and network properties. The data were processed to calculate key metrics, including Mean Firing Rate, Burst Frequency, and Network Burst Frequency, offering a detailed understanding of neural dynamics. For Well-level Frequency analysis, the Mean Firing Rate was calculated at approximately 5.2 Hz, with a standard deviation of 6.3 Hz, indicating high variability in spike occurrences. Burst Frequency averaged 0.18 Hz, suggesting that bursts occurred at a rate of approximately 0.18 per second across the well. Network Burst Frequency, summarizing burst events at the network level, was recorded at 0.16 Hz, reflecting low synchronization across the neural network. These results highlight the overall network activity and variability within each well, which is particularly relevant for understanding pathological conditions. In contrast, the Probe-level Frequency analysis focused on individual probes within the network. The Mean Firing Rate was lower at 2.9 Hz, with a standard deviation of 3.1 Hz, indicating less variability compared to the Well-level data. Burst Frequency was consistent at 0.17 Hz, revealing similar burst rates to those observed in the Well-level analysis. However, Network Burst Frequency was not measured at the Probe level, emphasizing that this metric is specific to network-wide activity recorded at the well level. Comparison of Well-level and Probe-level data revealed that Well-level analysis captures collective neural network behavior, leading to higher average values for firing and burst rates due to the inclusion of multiple probes. In contrast, Probe-level data offer a more granular perspective, focusing on localized activity patterns within specific regions of the network. These findings underscore the complementary nature of Well-level and Probe-level analyses in understanding neural dynamics. While Well-level data provide an overview of network-wide activity, Probe-level data enable detailed examination of localized neuronal behavior, offering critical insights into the impact of *SCN2A* mutations on neuronal activity and network synchronization. (Figure 23)

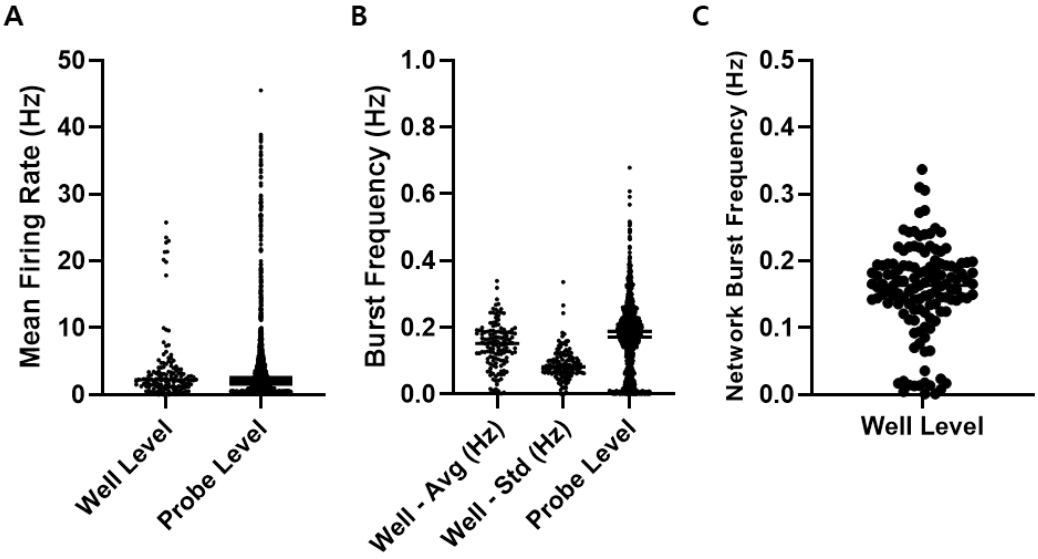

Figure 23. Well- and Probe-Level Frequency Analysis in Neural Activity (A) Mean Firing Rate (Hz): Comparison of Well-level (left) and Probe-level (right) spike rates per second, illustrating variability in neuronal excitability. (B) Burst Frequency (Hz): Average burst events per second for Well-level (left), Standard burst events per second for Well-level (middle) and Probe-level (right), highlighting differences in rhythmic activity across scales. (C) Network Burst Frequency (Hz): Well-level synchronized burst rates per second, indicating network-wide coordination, as this metric is not available for Probe-level analysis.

3.7. Discovering New Compounds

There are many existing drugs for epilepsy, but their significant side effects limit their applicability and effectiveness. Additionally, the diverse genetic mutations underlying epilepsy require distinct therapeutic approaches. Among these, *SCN2A*-related epilepsy is characterized by over-excitable neurons, making sodium channel blockers a common treatment strategy. In pursuit of new therapeutic compounds, I analyzed the tertiary structure of neurons derived from the 2AMJH model. The analysis focused on identifying binding site residues critical for pharmacological intervention. Using artificial intelligence-driven methodologies, five sodium channel blocker compounds were selected for further evaluation.(Table 18) These compounds are summarized in Table 18 and represent a targeted approach to addressing neuronal hyperexcitability.

The selected compounds underwent rigorous testing over a six-week period on 2AMJH-derived neurons. Phenytoin, a widely recognized sodium channel blocker, was included as a control to benchmark the efficacy of these novel compounds. To ensure experimental consistency, I employed dimethyl sulfoxide as a solvent, maintaining a baseline concentration of 0 μM. For each test condition, an equal volume of medium (1/1000 of the compound concentration) was used. Electrophysiological data were collected both pre- and post-treatment, with post-treatment data normalized to the baseline for clarity and comparison.

The analysis centered on four key metrics: activity metrics, electrode burst metrics, network burst metrics, and synchrony metrics. These metrics provide a comprehensive view of neuronal activity at both the cellular and network levels. Phenytoin demonstrated a significant, concentration-dependent reduction in neuronal excitability. The firing rate, expressed in hertz, showed a clear downward trend with increasing concentrations, as depicted in Figure 24A1. The statistical significance of these findings is supported by p-values of less than 0.0001 across all tested concentrations. Additionally, bursts—defined as simultaneous occurrences of five or more spikes—exhibited similar concentration-dependent reductions. The most important measure is the Burst Percentage, which quantifies the firing rate (Hz) and burst activity. We observed the effect starting at 500 nM, with a half-maximal inhibitory concentration (IC_{50}) of 10 μM. Analyzing the drug in terms of dose dependence provided further insights into the compound's effects on neuronal dynamics. The changes in these parameters underscore phenytoin's impact on temporal patterns of neuronal firing. At the network level, reductions in burst frequency and synchronization indices were observed. Synchrony metrics, illustrated in Figures 24A7, revealed a progressive decline in coordinated neuronal activity with increasing concentrations of phenytoin. This disruption of hyper-synchronized activity aligns with its therapeutic mechanism and highlights its potential to alleviate epileptic symptoms.

Among the tested compounds, 4456-3635 emerged as a particularly promising candidate, demonstrating effects comparable to those of phenytoin. This compound significantly reduced firing rates and spike counts, with p-values consistently below 0.0001. The effect was observed even at the lowest concentration (10 nM) and progressively strengthened with increasing concentrations. The graph demonstrates a dose-dependent response, showing a gradual decrease in firing rates as the concentration increases. The IC_{50} value was observed at approximately 18.74 μM, indicating that the firing rate was reduced by half at this concentration. Notably, more pronounced effects were observed at concentrations of 500 nM and 1 μM. Both burst frequency and burst percentage were effectively modulated, highlighting the compound's robust and consistent mechanism of action. (Figures 24B1-B7)

Compound 2786-4513 demonstrated remarkable inhibitory effects at higher concentrations, with spike activity nearly disappearing at 12.5 μM, showcasing its strong potential to suppress neuronal excitability. According to the graphs, this compound began to exhibit significant effects from 1 μM, with its impact intensifying sharply as the concentration increased. Both the firing rate and burst frequency decreased progressively with increasing concentrations, while the synchrony index also displayed a similar pattern of reduction. Notably, the IC_{50} value was observed at approximately 298 nM, where neuronal activity was reduced by half. This finding strongly suggests that the compound possesses a concentration-dependent inhibitory effect. The reduction in burst frequency and synchrony index indicates that the compound effectively suppresses hyperactivity at the network level, highlighting its potential suitability for regulating complex neuronal network dynamics. (Figures 24C1-C7)

Compound 4561-0590 demonstrated remarkable efficacy even at low concentrations, with significant reductions in firing rate observed starting at 10 nM. The graphs clearly show a dose-dependent effect, with both firing rate and spike activity significantly reduced as the concentration increases. The IC_{50} value was observed at approximately 1.04 μM, where neuronal activity was reduced by half, highlighting the compound's potency. In terms of burst metrics, including Burst Frequency and Network Burst levels, significant reductions were observed at concentrations as low as 10 nM, with effects becoming more pronounced at higher doses. Synchrony Index also exhibited a clear dose-dependent decrease, indicating effective disruption of hyper-synchronized neuronal activity, particularly from 100 nM onward. These findings suggest that Compound 4561-0590 has robust and consistent inhibitory effects across multiple metrics, with notable potential for treating hyperexcitability in neuronal networks. (Figures 24D1-D7)

Compound 4333-1696 demonstrated results similar to phenytoin, showing significant reductions in spike and burst metrics across all tested concentrations. The Firing Rate began to decrease significantly at a concentration of 50 nM and exhibited stronger inhibitory effects as the concentration increased. The IC_{50} value was observed at approximately 0.2319 μM, indicating that the firing rate was reduced by half at this concentration, highlighting the compound's dose-

dependent inhibitory effects. The Burst (at both burst and network burst levels) and the Synchrony Index also exhibited gradual reductions with increasing concentrations. Notably, the Burst Frequency showed significant decreases starting at 50 nM, with the effects becoming more pronounced at higher concentrations. The Synchrony Index displayed a marked decrease at concentrations above 250 nM, effectively suppressing excessive neuronal synchronization within the network. These results suggest that compound 4333-1696 has excellent potential to suppress neuronal excitability at the network level and mitigate excessive neuronal activity. This makes it a strong candidate for further drug development and research. (Figures 24E1-E7)

Compound 6466-0224 demonstrated high sensitivity, with effects observed even at an extremely low concentration of 1nM. The Firing Rate, Burst, and Synchrony Index showed a gradual decrease with increasing concentration, with the optimal efficacy in Burst levels observed at 20μM. This suggests that the compound has a strong, concentration-dependent inhibitory effect on neuronal excitability at higher concentrations. However, the IC_{50} value of 18.83μM presents a somewhat contradictory result, as inhibitory effects were already apparent at very low concentrations. This inconsistency implies that the compound may exhibit a complex mechanism of action within specific concentration ranges, warranting further research and analysis to clarify its pharmacological properties. At concentrations above 20μM, Burst activity was almost completely suppressed at the network level. However, Synchrony Index showed significant effects even at very low concentrations. These findings suggest that while the compound has the potential to effectively regulate hyperactivity in neuronal networks, additional studies are needed to fully understand its mechanisms and implications. (Figures 24F1-F7)

The network-level effects of the tested compounds provide critical insights into their therapeutic potential. The reductions in burst frequency and synchronization indices observed across several compounds highlight their efficacy in mitigating the hyper-synchronized neuronal activity characteristic of *SCN2A*-related epilepsy. For example, compound 4456-3635 significantly decreased network synchronization, showing effects similar to those of phenytoin. These results suggest that this compound may effectively alleviate the large-scale neuronal hyperactivity commonly observed in epileptic networks. Compounds 2786-4513 and 4333-1696 also demonstrated consistent decreases in synchronization indices, establishing their strong potential as therapeutic candidates. In particular, 2786-4513 exhibited pronounced inhibitory effects at higher concentrations, while 4333-1696 showed stable responses across a range of concentrations, indicating its robust ability to regulate neuronal networks. Meanwhile, compound 6466-0224 exhibited notable effects at specific concentrations but showed variable responses at others. This suggests that the compound may have a unique mechanism of action, requiring further research to fully understand its effects. Notably, 6466-0224 significantly reduced synchronization at certain concentrations, but its overall concentration-dependent pattern differed from that of other compounds. These findings indicate that each compound has strong potential to effectively modulate

hyperactivity in neuronal networks. Further detailed analysis of their mechanisms of action and concentration-specific responses is essential to fully explore their therapeutic applications.

The electrophysiological data collected in this study underscore the importance of dose optimization in drug development. For example, compound 2786-4513 exhibited a clear dose-response relationship, with its most pronounced effects observed at higher concentrations. This relationship highlights the need to carefully balance efficacy with potential side effects. Similarly, compound 4561-0590's exceptional potency at low concentrations presents both opportunities and challenges. While its low-dose efficacy minimizes the risk of side effects, the difficulty in testing at higher concentrations necessitates precise experimental control and further investigation.From a methodological standpoint, the use of DMSO as a solvent ensured consistency across experimental conditions, while the normalization of post-treatment data to baseline values facilitated clear comparisons between compounds. The focus on four key electrophysiological metrics provided a comprehensive assessment of each compound's impact on neuronal and network dynamics. By analyzing firing rates, burst patterns, and synchronization indices, this study offers a detailed view of how these compounds modulate neuronal activity. In addition to assessing the efficacy of individual compounds, this study highlights the broader implications of using artificial intelligence in drug discovery. The identification of sodium channel blocker compounds as potential treatments for *SCN2A*-related epilepsy underscores the power of AI-driven methodologies in streamlining the drug development process. By utilizing advanced computational techniques to analyze the tertiary structure of neurons and identify binding site residues, this approach enables the rapid identification of promising candidates for further investigation

Future research should focus on several key areas to advance the development of these compounds. First, long-term studies are needed to evaluate the sustainability of their effects and their impact on neuronal plasticity. Second, detailed pharmacokinetic and pharmacodynamic analyses are essential to understand the mechanisms underlying their actions. Third, exploring the molecular pathways affected by these compounds could provide valuable insights into their therapeutic potential and guide the development of next-generation treatments.

The results of this study also have important clinical implications. The observed reductions in neuronal excitability, burst activity, and synchronization suggest that these compounds could be effective in managing the symptoms of *SCN2A*-related epilepsy. By targeting the specific genetic and physiological characteristics of this condition, these compounds offer a more personalized approach to treatment. However, translating these findings into clinical practice will require rigorous testing in preclinical and clinical settings to ensure their safety and efficacy.

In conclusion, the five sodium channel blocker compounds investigated in this study represent promising candidates for the treatment of *SCN2A*-related epilepsy. Among these, compounds 4456-3635, 2786-4513, and 4333-1696 emerged as the most effective, demonstrating significant reductions in neuronal excitability, burst activity, and synchronization. These findings highlight their

potential to address the unique challenges associated with this condition. The incorporation of artificial intelligence in the drug discovery process has proven instrumental in identifying these candidates and underscores the importance of leveraging advanced technologies in biomedical research. As this work progresses, it holds the promise of offering new hope to individuals affected by *SCN2A*-related epilepsy, ultimately improving their quality of life and advancing the field of precision medicine.

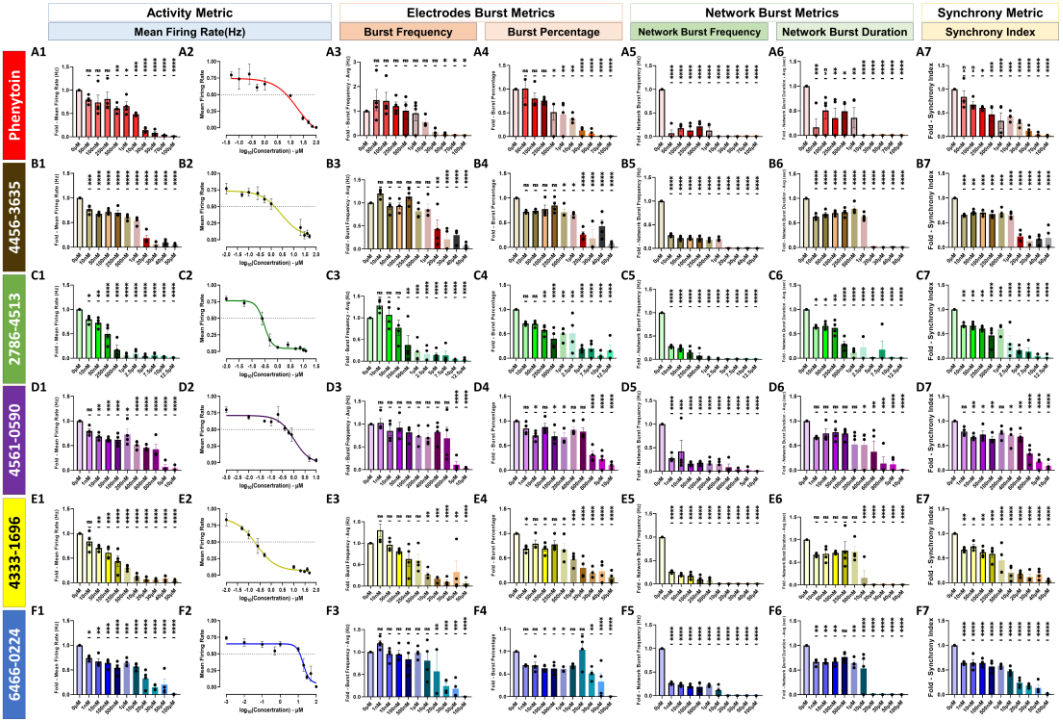

Figure 24. Confirmation of Drug Test Differences between *SCN2A* Patient-Derived Neurons (2AMJH) Treated with Phenytoin and five Compound

(A1-A7) Phenytoin, (B1-B7) 4456-3635, (C1-C7) 2786-4513, (D1-D7) 4561-0590, (E1-E7) 4333-1696, (F1-F7) 6466-0224, (A1,B1,C1,D1,E1,F1) Mean Firing Rate (Hz) – Bar Graph. (A2,B2,C2,D2,E2,F2) Mean Firing Rate – IC_{50}. (A3,B3,C3,D3,E3,F3) Burst Frequency - Avg (Hz). (A4,B4,C4,D4,E4,F4) Burst Percentage – Avg. (A5,B5,C5,D5,E5,F5) Network Burst Frequency (Hz). (A6,B6,C6,D6,E6,F6) Network Burst Duration - Avg (sec). (A7,B7,C7,D7,E7,F7) Synchrony Index. N = 4, *:p≤0.05, **:p≤0.01, ***:p≤0.001, ****: p≤0.0001

Table 18. Sodium Channel Blocker Drug Candidate

Data base ID	Binding affinity	Smiles	K-mean_ Clustering	Spectral_C lustering	Affinity_pr opagation	Tanimoto _similarity _Clustering
4456-3635	-11	Cc1c(C(=O)OCc2ccccc2)c2cc(ccc2o1)NS(c1ccc2c3c(cccc13)C(N2)=O)(=O)=O	2	1	6	88
2786-4513	-11.3	C1C(c2ccc3ccccc3c2)c2ccc3ccccc3c2NC1=O	1	2	3	91
4561-0590	-11.6	CCn1c2ccccc2c2cc(/C=N/c3ccc(cc3)S(Nc3c(C)cc(C)cc3C)(=O)=O)ccc12	2	3	1	93
4333-1696	-10.8	CC1=CCC(c2cc(C)c(c3ccccc3)nc2)N(C1c1ccccc1)S(c1ccc(C)cc1)(=O)=O	1	4	8	86
6466-0224	-10.9	CC1CC(C)N(C(C)C1)C(CSc1nc2c3ccccc3CCc2c(C(F)(F)F)n1)=O	1	5	7	87

4. DISCUSSION

The c.4886G>T (p.Arg1629Leu) mutation in the *SCN2A* gene encodes a subunit of the voltage-gated sodium channel alpha 1.2 and is closely associated with early-onset epileptic encephalopathy (EE). This disorder is characterized by severe seizure phenotypes, intellectual disabilities, and developmental delays. Through this study, I aimed to dissect the impact of this specific mutation on neuronal excitability and network dynamics using an advanced array of experimental approaches, including patient-derived induced pluripotent stem cells (iPSCs), CRISPR/Cas9-mediated gene editing, and electrophysiological analyses via micro-electrode arrays (MEA) techniques. The overarching goal was to identify the cellular and molecular underpinnings of *SCN2A*-related epilepsy and assess novel pharmacological strategies to mitigate its pathological effects. The study's first crucial step was the derivation of iPSCs from a patient harboring the *SCN2A* mutation. Peripheral blood mononuclear cells (PBMCs) were isolated and reprogrammed into iPSCs using a non-integrative episomal vector system. This process yielded high-quality pluripotent cells, which expressed markers such as NANOG, OCT4, SOX2, and SSEA-4, as confirmed through immunocytochemistry. The differentiation protocol was optimized to generate excitatory and inhibitory cortical neurons, reflective of the human forebrain environment. Transcription factors such as NGN2, ASCL1, and DLX2 were introduced via lentiviral vectors to induce directed differentiation. Importantly, co-culturing these neurons with astrocytes created a physiologically relevant microenvironment, mimicking the *in-vivo* dynamics of cortical networks. Electrophysiological profiling revealed significant differences between *SCN2A*-mutant neurons and their isogenic controls. Using MEA, I observed that mutant neurons exhibited hyperexcitability characterized by increased mean firing rates, burst frequencies, and synchronized network activity. These pathological hallmarks were consistent with the clinical phenotypes of *SCN2A*-related EE, particularly its gain-of-function mutations, which lead to persistent sodium channel activity and heightened neuronal excitability. Electrophysiology recordings provided further insights into cell activity, revealing increased spike densities at higher current injections in *SCN2A*-mutant neurons. Action potential dynamics, including prolonged depolarization phases, were also noted, indicating that the mutation directly impacts voltage-gated sodium channel function. The introduction of CRISPR/Cas9 technology was pivotal in generating isogenic control lines, where the c.4886G>T mutation was corrected. These genetically corrected neurons served as critical controls, displaying normal electrophysiological profiles that validated the mutation's specific contribution to hyperexcitability. The gene-editing process involved careful design and optimization of single-guide RNA (sgRNA) and homology-directed repair templates to ensure precise editing. The edited cells were confirmed via Sanger sequencing, and their phenotypes were assessed across multiple passages to ensure stability. The contrast between mutant and isogenic neurons underscored the mutation's direct role in altering neuronal excitability. Importantly, the isogenic lines demonstrated the feasibility of using CRISPR/Cas9 not only for disease modeling but also for potential therapeutic interventions. By normalizing the pathological activity observed in *SCN2A*-mutant neurons, these edited lines provide a promising platform for preclinical drug testing. To explore therapeutic avenues, I tested a set of novel sodium channel blocker-based compounds designed using artificial

intelligence-assisted methodologies. These compounds were selected based on their structural similarities to carbamazepine, a well-established anti-epileptic drug, and their predicted binding affinities to sodium channel subunits. Phenytoin, a classic sodium channel blocker, served as a benchmark for comparison. Electrophysiological data indicated that the tested compounds effectively reduced neuronal hyperexcitability in *SCN2A*-mutant neurons. Among the compounds, 4456-3635 emerged as the most potent, significantly decreasing firing rates and burst synchronization at low concentrations. This compound demonstrated dose-dependent efficacy without inducing cytotoxicity, making it a strong candidate for further investigation. The compounds' effects on network metrics, such as burst duration and synchronization indices, were particularly noteworthy. Hyper-synchronized activity, a hallmark of epileptic networks, was significantly attenuated following treatment with these compounds. Compound 2786-4513, for instance, showed a dual-phase response, with strong inhibitory effects on neuronal activity at higher concentrations. The detailed analysis of these pharmacological agents provided critical insights into their mechanisms of action and potential therapeutic windows. The reduction in synchronized burst activity and hyperexcitability metrics aligns with the broader goal of normalizing pathological network dynamics in *SCN2A*-related epilepsy.

The integration of MEA technology allowed for the simultaneous monitoring of network-level neuronal activity, providing a comprehensive view of how *SCN2A* mutations influence excitability and synchronization across cortical-like circuits. The increased mean firing rates observed in mutant neurons, alongside elevated burst frequencies and prolonged burst durations, reflect an underlying gain-of-function phenotype at the sodium channel level. These findings correlate with clinical observations of patients harboring *SCN2A* mutations, who often present with severe early-onset seizures and persistent cortical hyperexcitability. Burst synchronization, a critical feature of epileptogenic networks, was markedly heightened in mutant neurons, underscoring the mutation's role in network-level dysfunction. This pathological over-synchronization was effectively attenuated in isogenic neurons and further normalized upon treatment with the novel compounds, demonstrating their potential in mitigating epileptic activity.

The generation of isogenic controls through CRISPR/Cas9 gene editing not only validated the mutation's role but also established a robust disease model for preclinical testing. The precise correction of the c.4886G>T mutation allowed for direct comparisons between mutant and corrected neurons, isolating the mutation's effects from other genetic or environmental factors. This approach highlights the utility of CRISPR/Cas9 in both research and therapeutic contexts, offering a pathway toward personalized medicine for genetic epilepsies. The edited cells maintained stable phenotypes across multiple passages, and their differentiation potential was comparable to that of unedited cells, underscoring the technique's efficacy and safety.

The therapeutic potential of sodium channel blocker-based compounds was rigorously evaluated using MEA. The compounds were selected through an AI-driven drug discovery pipeline, which analyzed the tertiary structure of sodium channels and identified high-affinity binding sites. This approach facilitated the rapid identification of candidate molecules with optimized pharmacodynamic profiles. Among the tested compounds, 4456-3635 consistently outperformed others in reducing hyperexcitability metrics, including firing rates, burst frequencies, and

synchronization indices. The compound's effects were dose-dependent and achieved without observable cytotoxicity, highlighting its therapeutic promise.

Compound 2786-4513 displayed a unique dual-phase response, effectively suppressing neuronal activity at higher concentrations while modulating excitatory and inhibitory dynamics at lower doses. This biphasic action may reflect its interaction with specific sodium channel subtypes or auxiliary proteins, offering a nuanced approach to managing *SCN2A*-related epilepsy. The detailed analysis of synchronization metrics revealed that this compound significantly reduced network-level hyperactivity, suggesting its potential in addressing the large-scale cortical dysfunctions characteristic of this condition.

Phenytoin, used as a benchmark, demonstrated robust efficacy in reducing firing rates and burst synchronization, reaffirming its role as a first-line treatment for epilepsy. However, its broad-spectrum activity often results in side effects such as sedation and ataxia, which limit its utility in precision medicine. In contrast, the novel compounds, particularly 4561-0590 and 4333-1696, exhibited more selective actions, targeting hyperactive neurons while preserving overall network stability. This selectivity is crucial for minimizing off-target effects and improving patient outcomes.

The evaluation of burst metrics provided valuable insights into the compounds' mechanisms of action. Reductions in burst duration and inter-burst intervals indicate a normalization of neuronal firing patterns, while the attenuation of synchronized bursts aligns with the compounds' therapeutic goals. Synchrony metrics, including the Synchrony Index and Network Burst Frequency, further highlighted the compounds' ability to restore physiological network activity. Compound 6466-0224, despite its variable effects across concentrations, showed notable efficacy in reducing network synchronization at specific doses. This variability suggests a distinct mechanism of action, warranting further investigation to optimize its therapeutic application.

The integration of artificial intelligence in the drug discovery process represents a significant advancement in this study. By utilizing computational methods to predict binding site residues and analyze structural similarities, this approach streamlined the identification of high-potential candidates. The clustering of compounds based on spectral and Tanimoto similarity metrics ensured a diverse yet functionally relevant selection, enhancing the likelihood of discovering effective treatments for *SCN2A*-related epilepsy. This methodology not only accelerates the drug discovery process but also provides a blueprint for addressing other genetic disorders with complex molecular underpinnings.

The use of patient-derived iPSCs as a platform for preclinical drug testing underscores the relevance of this study to clinical applications. By modeling the specific genetic and physiological characteristics of *SCN2A*-related epilepsy, this research bridges the gap between bench and bedside, paving the way for personalized therapeutic strategies. The ability to assess compound efficacy in a patient-specific context ensures that the findings are directly translatable to clinical settings, offering new hope for individuals affected by this challenging condition.

The advanced methodologies employed in this study, particularly the integration of patient-derived iPSCs, CRISPR/Cas9 gene editing, and electrophysiological profiling, provide a robust framework

for investigating *SCN2A*-related epilepsy. By creating a physiologically relevant *in-vitro* model, this research highlights the nuanced interactions between genetic mutations and neuronal function. The differentiation of iPSCs into excitatory glutamatergic and inhibitory GABAergic neurons mimics the cellular composition of the human forebrain, providing insights into how *SCN2A* mutations disrupt the balance of excitation and inhibition. The inclusion of astrocytes in the co-culture system further enhances the model's physiological relevance, as astrocytes play a pivotal role in synaptic pruning, neurotransmitter recycling, and ion homeostasis. These interactions are particularly important in the context of *SCN2A*-related epilepsy, where cortical network imbalances drive the pathological phenotypes.

Electrophysiological analyses revealed that the hyperexcitability observed in *SCN2A*-mutant neurons extends beyond single-cell dynamics to influence broader network synchronization. The increased synchronization indices and network burst frequencies in mutant neurons mirror the clinical presentation of early-onset epileptic encephalopathy, characterized by large-scale cortical hyperactivity. These findings underscore the importance of targeting both cellular and network-level dysfunctions in therapeutic strategies. The normalization of these pathological metrics in isogenic controls and drug-treated neurons demonstrates the efficacy of the employed interventions, providing a foundation for future clinical applications.

The role of CRISPR/Cas9 gene editing in this study cannot be overstated. By correcting the c.4886G>T mutation, this approach not only validated the mutation's contribution to the observed phenotypes but also established a disease-free baseline for comparison. The precision of the gene-editing process, confirmed through Sanger sequencing and functional assays, underscores its potential as a therapeutic tool. The edited neurons exhibited normal electrophysiological properties, including firing rates and burst synchronization, aligning closely with the profiles of healthy neurons. This highlights the feasibility of using gene editing to address the root causes of genetic epilepsies, offering a potential pathway toward long-term disease modification.

The exploration of novel sodium channel blocker-based compounds represents a significant advancement in the therapeutic landscape of *SCN2A*-related epilepsy. These compounds were carefully selected using AI-driven methodologies, ensuring high binding affinities and targeted actions. Their effects were rigorously evaluated across multiple electrophysiological metrics, providing a comprehensive view of their therapeutic potential. Compound 4456-3635 emerged as a leading candidate, demonstrating consistent efficacy in reducing neuronal hyperexcitability and network synchronization. Its dose-dependent action and lack of cytotoxicity highlight its promise as a targeted therapeutic agent.

Compound 2786-4513 exhibited unique pharmacodynamic properties, with strong inhibitory effects at higher concentrations and a dual-phase response at lower doses. This compound's ability to modulate both excitatory and inhibitory dynamics suggests a nuanced mechanism of action, making it particularly suited for addressing the complex network dysfunctions seen in *SCN2A*-related epilepsy. Similarly, compound 4561-0590 showed exceptional potency at low concentrations, offering a potential therapeutic window with reduced risk of side effects. However, its limited impact on network-level synchronization indicates a more localized action, warranting further studies to optimize its use.

The comparison of these novel compounds with phenytoin, a well-established sodium channel blocker, provided valuable benchmarks for assessing their efficacy. While phenytoin effectively reduced firing rates and burst synchronization, its broad-spectrum activity often results in unwanted side effects, such as cognitive impairment and motor dysfunction. In contrast, the novel compounds demonstrated more selective actions, targeting hyperactive neurons while preserving overall network stability. This selectivity is critical in minimizing off-target effects and improving patient outcomes, particularly in the context of precision medicine.

The reduction in burst synchronization and hyperexcitability metrics observed in drug-treated *SCN2A*-mutant neurons reflects the compounds' ability to normalize pathological network activity. Synchrony metrics, including the Synchrony Index and Network Burst Duration, were significantly modulated by these compounds, indicating their potential to restore physiological neuronal dynamics. The detailed analysis of inter-burst intervals and firing rate variability provided additional insights into their mechanisms of action, highlighting their ability to disrupt the hyperactive bursts characteristic of epileptic circuits.

The use of computational methodologies in the drug discovery process represents a transformative approach to addressing complex genetic disorders. By analyzing neuronal tertiary structures and predicting binding site residues, AI-driven methodologies facilitated the rapid identification of high-potential candidates. The clustering of compounds based on structural and functional similarities ensured a diverse yet targeted selection, enhancing the likelihood of discovering effective treatments. This approach not only accelerates the drug discovery process but also sets a precedent for leveraging advanced technologies in biomedical research.

The findings from this study have profound implications for the treatment of *SCN2A*-related epilepsy and other genetic epilepsies. By addressing the root causes of hyperexcitability at both genetic and pharmacological levels, this research advances the field of precision medicine. The ability to model disease-specific phenotypes using patient-derived iPSCs and correct these phenotypes through gene editing represents a significant step forward in personalized therapeutic strategies. The identification of novel sodium channel blockers further enhances this approach, offering targeted interventions that address the unique challenges posed by *SCN2A* mutations.

The role of astrocytes in modulating neuronal activity and network synchronization was also highlighted in this study. The inclusion of astrocytes in the co-culture system significantly enhanced neuronal maturation and synaptic connectivity, providing a more accurate representation of cortical dynamics. Astrocytes play active roles in regulating neurotransmitter levels, maintaining ion gradients, and supporting synaptic function, making them integral to the study of neuronal disorders. Future research should explore the bidirectional interactions between neurons and astrocytes in greater detail, as these interactions may reveal novel therapeutic targets for *SCN2A*-related epilepsy.

This study not only advances our understanding of *SCN2A*-related epilepsy but also highlights the importance of integrating diverse methodologies to comprehensively address complex neurological disorders. The patient-derived iPSCs used in this research provided a unique platform to model disease-specific phenotypes, allowing for an in-depth exploration of how the c.4886G>T mutation impacts neuronal function. By differentiating these iPSCs into cortical neurons and using lentiviral

systems to generate excitatory and inhibitory subtypes, the study successfully recreated the cellular architecture of the human forebrain. This approach provided a robust context for investigating the functional consequences of *SCN2A* mutations, particularly the balance of excitation and inhibition within neuronal networks. The co-culture with astrocytes further enhanced the model's physiological relevance, as astrocytes play a critical role in synaptic pruning, ion homeostasis, and neurotrophic factor secretion, all of which are disrupted in epilepsy.

The hyperexcitability observed in *SCN2A*-mutant neurons underscores the mutation's gain-of-function effects, which alter sodium channel gating dynamics and lead to pathological overactivation. Electrophysiological recordings revealed significant increases in mean firing rates, burst frequencies, and synchronization indices, reflecting the heightened excitability of *SCN2A*-mutant neurons. These findings align with the clinical manifestations of *SCN2A*-related epileptic encephalopathy, where seizures are driven by large-scale cortical hyperactivity. The ability to capture these pathological features *in-vitro* demonstrates the strength of the employed methodologies, particularly the combination of MEA analyses. While MEA provided a broad view of network dynamics, electrophysiology recordings offered detailed insights into single-cell activity, enabling a comprehensive characterization of the mutation's impact.

CRISPR/Cas9-mediated gene editing was instrumental in validating the causal relationship between the *SCN2A* mutation and the observed phenotypes. By correcting the c.4886G>T mutation in patient-derived iPSCs, this study created isogenic controls that served as a disease-free baseline. These controls exhibited normal electrophysiological properties, including reduced firing rates and normalized burst synchronization, confirming that the mutation was responsible for the pathological activity. The precision of the gene-editing process, confirmed through sequencing and functional assays, underscores its potential as a therapeutic tool for genetic epilepsies. Moreover, the ability to create isogenic lines provides a platform for testing novel interventions and exploring the broader implications of *SCN2A* mutations.

The discovery and evaluation of sodium channel blocker-based compounds represent a significant contribution to the therapeutic landscape of *SCN2A*-related epilepsy. Using AI-driven methodologies, five novel compounds were identified and tested for their efficacy in reducing neuronal hyperexcitability. These compounds demonstrated varying degrees of success, with compound 4456-3635 emerging as the most effective. Its ability to reduce firing rates, burst frequencies, and synchronization indices highlights its potential as a targeted therapeutic agent. The compound's dose-dependent action and lack of cytotoxicity further support its suitability for clinical development. Compound 2786-4513 also showed promise, particularly at higher concentrations, where it effectively suppressed neuronal activity. Its dual-phase response, modulating both excitatory and inhibitory dynamics, suggests a nuanced mechanism of action that could address the complex network dysfunctions seen in *SCN2A*-related epilepsy.

The comparative analysis of phenytoin and novel compounds provided valuable insights into their mechanisms of action and therapeutic potential. While phenytoin effectively reduced neuronal hyperexcitability, its broad-spectrum activity often results in undesirable side effects. In contrast, the novel compounds demonstrated more selective actions, targeting hyperactive neurons without disrupting overall network stability. This selectivity is critical in the context of precision medicine,

where minimizing off-target effects is essential for improving patient outcomes. Compound 4561-0590, in particular, exhibited exceptional potency at low concentrations, offering a potential therapeutic window with reduced risk of side effects. However, its limited impact on network-level synchronization indicates a need for further studies to optimize its application.

The reduction in synchronization metrics observed in drug-treated neurons highlights the compounds' ability to normalize pathological network activity. Synchronization indices, network burst durations, and inter-burst intervals were significantly modulated, indicating a return to more physiologically normal dynamics. These findings underscore the importance of targeting both cellular and network-level dysfunctions in therapeutic strategies. The detailed analysis of burst patterns provided additional insights into the compounds' mechanisms of action, particularly their ability to disrupt the hyperactive bursts characteristic of epileptic circuits. This disruption is critical for mitigating the large-scale cortical hyperactivity seen in *SCN2A*-related epilepsy.

While this study provides valuable insights into the pathological and therapeutic landscape of *SCN2A*-related epilepsy, certain limitations highlight avenues for future research. Notably, the experiments were conducted exclusively *in-vitro*, and the absence of *in-vivo* validation limits the direct applicability of the findings to complex physiological systems. Animal models or humanized systems could provide critical insights into the mutation's effects within an intact neural environment and assess the translational potential of the identified therapeutic compounds.

Additionally, the use of 2D cell cultures in this study introduces inherent constraints. Neurons cultured on a flat surface may not fully recapitulate the three-dimensional architecture and microenvironment of the human brain, which are essential for modeling neuronal connectivity and network dynamics. Advanced 3D culture systems, such as brain organoids, could address this limitation by offering a more physiologically relevant model that mimics cortical organization and cell-cell interactions. Incorporating such systems in future studies would enhance the robustness of the findings and provide deeper insights into the mutation's impact on brain development and function.

These advancements would not only refine our understanding of *SCN2A*-related epilepsy but also strengthen the clinical relevance of therapeutic interventions, bridging the gap between *in-vitro* discoveries and *in-vivo* applications.

The integration of advanced computational methodologies in the drug discovery process represents a transformative approach, streamlining the identification of high-potential candidates and accelerating their evaluation. By utilizing computational algorithms to analyze neuronal tertiary structures and predict binding site residues, this study identified compounds with high binding affinities and targeted actions. The clustering of compounds based on structural and functional similarities ensured a diverse yet focused selection, enhancing the likelihood of discovering effective treatments. This approach not only reduces the time and cost associated with traditional drug discovery but also sets a precedent for using advanced technologies in biomedical research.

The implications of this research extend beyond *SCN2A*-related epilepsy, offering a framework for investigating other genetic epilepsies and neurological disorders. The methodologies employed,

including patient-derived iPSCs, CRISPR/Cas9 gene editing, and electrophysiological profiling, provide a versatile platform for exploring disease mechanisms and evaluating potential therapies. The ability to model disease-specific phenotypes *in-vitro* and correct these phenotypes through gene editing represents a significant advancement in precision medicine. Furthermore, the identification of novel therapeutic compounds highlights the potential for targeted interventions that address the unique challenges posed by specific genetic mutations.

This study also emphasizes the importance of a multidisciplinary approach in addressing complex neurological disorders. The integration of advanced genetic editing tools, high-throughput electrophysiological analyses, and AI-driven drug discovery exemplifies the collaborative *nature* of modern neuroscience research. Each methodology contributes unique insights, collectively advancing our understanding of *SCN2A*-related epilepsy and its potential treatments. The focus on patient-derived models ensures that the findings are directly relevant to clinical applications, bridging the gap between bench and bedside. By recreating the specific genetic and physiological characteristics of *SCN2A*-mutant neurons, this research offers a tangible path toward personalized medicine.

5. CONCLUSION

The research undertaken on the *SCN2A* c.4886G>T (p.Arg1629Leu) mutation represents a significant leap forward in our understanding of *SCN2A*-related epileptic encephalopathies and their associated pathophysiological mechanisms. By leveraging patient-derived induced pluripotent stem cells (iPSCs) and CRISPR/Cas9-based gene editing, this study meticulously elucidates the functional implications of this specific mutation on neuronal excitability, network synchronization, and cellular dynamics. The ability to produce isogenic controls alongside mutant lines further strengthens the validity and specificity of the findings, allowing for a direct comparison of electrophysiological behaviors and pharmacological responses between normal and mutated neurons.

At the core of this study is the successful modeling of *SCN2A*-related epilepsy *in-vitro*. The *SCN2A* gene, which encodes a critical subunit of the voltage-gated sodium channel, plays a central role in neuronal activity, including the generation and propagation of action potentials. The identified c.4886G>T mutation, which substitutes arginine with leucine at position 1629, has been classified as likely pathogenic due to its disruption of sodium channel function. By inducing iPSCs derived from a patient's peripheral blood mononuclear cells to differentiate into cortical neurons, the study provides a direct window into the neuronal and network-level abnormalities caused by this mutation. Moreover, the use of advanced electrophysiological tools such as micro-electrode array (MEA) have facilitated a detailed characterization of neuronal excitability and firing dynamics in these patient-derived neurons.

One of the most striking findings of this study is the confirmation of hyperexcitability in neurons harboring the *SCN2A* mutation. These neurons displayed significantly increased mean firing rates, burst frequencies, and network synchronization compared to their isogenic controls, indicating a gain-of-function effect consistent with previous literature. The elevated burst activity observed in *SCN2A*-mutant neurons, coupled with increased synchrony metrics, aligns with the hyperactive neuronal states commonly associated with epilepsy.

In addition to characterizing the pathological features of the *SCN2A* mutation, this study also explored therapeutic avenues, focusing on sodium channel blockers as potential treatments. Phenytoin, a widely recognized sodium channel blocker, was used as a benchmark, against which five novel compounds were evaluated. Among these, compound 4456-3635 emerged as the most promising candidate, demonstrating significant efficacy in reducing firing rates, burst activity, and synchronization in *SCN2A*-mutant neurons. The ability of this compound to modulate hyperexcitability without inducing cytotoxicity underscores its potential as a targeted therapeutic agent. Other compounds, such as 2786-4513 and 4561-0590, also showed potent effects, with dose-dependent reductions in neuronal excitability and bursts. These findings not only expand the

therapeutic landscape for *SCN2A*-related epilepsy but also highlight the importance of personalized medicine in addressing the diverse genetic underpinnings of epilepsy.

The use of artificial intelligence-assisted drug discovery methodologies in this study represents a novel and highly impactful approach to therapeutic development. By analyzing neuronal tertiary structures and identifying critical binding site residues, advanced computational algorithms facilitated the rapid identification of carbamazepine-based compounds with high binding affinities. This innovative integration of computational technologies and neuroscience underscores the potential of advanced tools to accelerate drug discovery and optimize treatment strategies for complex genetic disorders.

Furthermore, the incorporation of astrocyte co-culture systems added a critical layer of physiological relevance to the *in-vitro* disease model. Astrocytes, known for their roles in synaptic pruning, neurotransmitter regulation, and neurotrophic support, significantly enhanced neuronal maturation and synaptic connectivity. This supportive microenvironment allowed for more accurate modeling of cortical neuronal networks and their pathological disruptions in *SCN2A*-related epilepsy. The bidirectional interactions between neurons and astrocytes observed in this study suggest additional avenues for therapeutic exploration, particularly in targeting astrocytic dysfunctions that may exacerbate neuronal hyperexcitability.

The study's use of CRISPR/Cas9 gene editing to create isogenic controls was instrumental in isolating the specific effects of the *SCN2A* mutation. The successful correction of the c.4886G>T mutation in patient-derived neurons validated the mutation's role in driving the observed pathological features, while also demonstrating the feasibility of gene-editing approaches as a potential therapeutic strategy. These findings highlight the dual importance of genetic and pharmacological interventions in treating *SCN2A*-related epilepsy. While sodium channel blockers address the symptoms of hyperexcitability, gene editing holds the promise of correcting the underlying genetic defect, offering a more definitive solution to the disorder.

Despite its strengths, the study also raises important questions that warrant further investigation. The mechanisms underlying the mutation's gain-of-function effect on sodium channel gating require deeper exploration, particularly in the context of its impact on subthreshold neuronal activity and synaptic integration. Additionally, the variability in responses observed among the tested compounds emphasizes the need for comprehensive pharmacokinetic and pharmacodynamic studies to optimize dosing regimens and minimize potential side effects. The long-term effects of these compounds on neuronal plasticity and network stability also remain to be elucidated, particularly in the context of chronic epilepsy management.

The broader implications of this research extend beyond *SCN2A*-related epilepsy, offering a robust framework for investigating other genetic epilepsies and neurological disorders. The methodologies employed, including patient-derived iPSCs, CRISPR/Cas9 gene editing, and

advanced electrophysiological analyses, provide a versatile platform for modeling disease-specific phenotypes and evaluating targeted interventions. The successful differentiation of iPSCs into cortical neurons further underscores the potential of stem cell technologies in translational neuroscience, paving the way for personalized medicine approaches to a wide range of neurological and neurodevelopmental disorders.

In summary, this study bridges the gap between basic research and clinical application, combining state-of-the-art genetic, pharmacological, and computational tools to address a pressing medical challenge. The insights gained from this research not only deepen our understanding of *SCN2A*-related epilepsy but also lay the groundwork for future advancements in precision medicine, offering hope to individuals affected by this debilitating condition.

References

1 Fisher, R. S. *et al.* ILAE official report: a practical clinical definition of epilepsy. *Epilepsia* **55**, 475-482 (2014).
2 Kwan, P. & Brodie, M. J. Early identification of refractory epilepsy. *New England Journal of Medicine* **342**, 314-319 (2000).
3 Engel Jr, J. ILAE classification of epilepsy syndromes. *Epilepsy Res.* **70**, 5-10 (2006).
4 Falco-Walter, J. J., Scheffer, I. E. & Fisher, R. S. The new definition and classification of seizures and epilepsy. *Epilepsy Res.* **139**, 73-79 (2018).
5 Scheffer, I. E. *et al.* ILAE classification of the epilepsies: Position paper of the ILAE Commission for Classification and Terminology. *Epilepsia* **58**, 512-521 (2017).
6 Fisher, R. S. *et al.* Epileptic seizures and epilepsy: definitions proposed by the International League Against Epilepsy (ILAE) and the International Bureau for Epilepsy (IBE). *Epilepsia* **46**, 470-472 (2005).
7 Fisher, R. S. *et al.* Operational classification of seizure types by the International League Against Epilepsy: Position Paper of the ILAE Commission for Classification and Terminology. *Epilepsia* **58**, 522-530 (2017).
8 Fisher, R. S. *et al.* Instruction manual for the ILAE 2017 operational classification of seizure types. *Epilepsia* **58**, 531-542 (2017).
9 Ong, M. S., Kohane, I. S., Cai, T., Gorman, M. P. & Mandl, K. D. Population-level evidence for an autoimmune etiology of epilepsy. *JAMA Neurol* **71**, 569-574 (2014).
10 Jung, J. *et al.* The economic burden of epilepsy in Korea, 2010. *Journal of Preventive Medicine and Public Health* **46**, 293 (2013).
11 De Boer, H. M., Mula, M. & Sander, J. W. The global burden and stigma of epilepsy. *Epilepsy Behav.* **12**, 540-546 (2008).
12 Berkovic, S. F., Mulley, J. C., Scheffer, I. E. & Petrou, S. Human epilepsies: interaction of genetic and acquired factors. *Trends Neurosci.* **29**, 391-397 (2006).
13 Thijs, R. D., Surges, R., O'Brien, T. J. & Sander, J. W. Epilepsy in adults. *The lancet* **393**, 689-701 (2019).
14 Shorvon, S. D. The etiologic classification of epilepsy. *Epilepsia* **52**, 1052-1057 (2011).
15 Liu, L. *et al.* Comparison of next-generation sequencing systems. *BioMed research international* **2012**, 251364 (2012).
16 Van Dijk, E. L., Auger, H., Jaszczyszyn, Y. & Thermes, C. Ten years of next-generation sequencing technology. *Trends Genet.* **30**, 418-426 (2014).
17 Schuster, S. C. Next-generation sequencing transforms today's biology. *Nat. Methods* **5**, 16-18 (2008).
18 Weiss, L. *et al.* Sodium channels SCN1A, *SCN2A* and SCN3A in familial autism. *Mol. Psychiatry* **8**, 186-194 (2003).
19 Nakamura, K. *et al.* Clinical spectrum of *SCN2A* mutations expanding to Ohtahara syndrome. *Neurology* **81**, 992-998 (2013).
20 Reynolds, C., King, M. D. & Gorman, K. M. The phenotypic spectrum of *SCN2A*-related epilepsy. *Eur. J. Paediatr. Neurol.* **24**, 117-122 (2020).
21 Wolff, M. *et al.* Genetic and phenotypic heterogeneity suggest therapeutic implications in *SCN2A*-related disorders. *Brain* **140**, 1316-1336 (2017).
22 Fukuma, G. *et al.* Mutations of neuronal voltage-gated Na+ channel α1 subunit gene

SCN1A in core severe myoclonic epilepsy in infancy (SMEI) and in borderline SMEI (SMEB). *Epilepsia* **45**, 140-148 (2004).
23 Goldin, A. L. Diversity of mammalian voltage-gated sodium channels. *Ann. N. Y. Acad. Sci.* **868**, 38-50 (1999).
24 Sugawara, T. *et al.* A missense mutation of the Na+ channel αII subunit gene Na v 1.2 in a patient with febrile and afebrile seizures causes channel dysfunction. *Proceedings of the National Academy of Sciences* **98**, 6384-6389 (2001).
25 Heron, S. E. *et al.* Sodium-channel defects in benign familial neonatal-infantile seizures. *The Lancet* **360**, 851-852 (2002).
26 Allen, N. M. *et al.* Unexplained early onset epileptic encephalopathy: exome screening and phenotype expansion. *Epilepsia* **57**, e12-e17 (2016).
27 Howell, K. B. *et al. SCN2A* encephalopathy: a major cause of epilepsy of infancy with migrating focal seizures. *Neurology* **85**, 958-966 (2015).
28 Ogiwara, I. *et al.* De novo mutations of voltage-gated sodium channel αII gene *SCN2A* in intractable epilepsies. *Neurology* **73**, 1046-1053 (2009).
29 Wong, V. C., Fung, C. & Kwong, A. K. *SCN2A* mutation in a Chinese boy with infantile spasm-response to Modified Atkins Diet. *Brain Dev.* **37**, 729-732 (2015).
30 De novo mutations in epileptic encephalopathies. *Nature* **501**, 217-221 (2013).
31 Sanders, S. J. *et al.* De novo mutations revealed by whole-exome sequencing are strongly associated with autism. *Nature* **485**, 237-241 (2012).
32 Sanders, S. J. *et al.* Progress in understanding and treating *SCN2A*-mediated disorders. *Trends Neurosci.* **41**, 442-456 (2018).
33 Ben-Shalom, R. *et al.* Opposing effects on NaV1. 2 function underlie differences between *SCN2A* variants observed in individuals with autism spectrum disorder or infantile seizures. *Biol. Psychiatry* **82**, 224-232 (2017).
34 Kobayashi, Y. *et al.* High prevalence of genetic alterations in early-onset epileptic encephalopathies associated with infantile movement disorders. *Brain Dev.* **38**, 285-292 (2016).
35 Liao, Y. *et al. SCN2A* mutation associated with neonatal epilepsy, late-onset episodic ataxia, myoclonus, and pain. *Neurology* **75**, 1454-1458 (2010).
36 Schwarz, N. *et al.* Mutations in the sodium channel gene *SCN2A* cause neonatal epilepsy with late-onset episodic ataxia. *J. Neurol.* **263**, 334-343 (2016).
37 Fromer, M. *et al.* De novo mutations in schizophrenia implicate synaptic networks. *Nature* **506**, 179-184 (2014).
38 Carroll, L. S. *et al.* Mutation screening of *SCN2A* in schizophrenia and identification of a novel loss-of-function mutation. *Psychiatr. Genet.* **26**, 60-65 (2016).
39 Li, J. *et al.* Genes with de novo mutations are shared by four neuropsychiatric disorders discovered from NPdenovo database. *Mol. Psychiatry* **21**, 290-297 (2016).
40 Takahashi, K. *et al.* Induction of pluripotent stem cells from adult human fibroblasts by defined factors. *Cell* **131**, 861-872 (2007).
41 Takahashi, K. & Yamanaka, S. Induction of pluripotent stem cells from mouse embryonic and adult fibroblast cultures by defined factors. *Cell* **126**, 663-676 (2006).
42 Liu, Y. *et al.* Directed differentiation of forebrain GABA interneurons from human pluripotent stem cells. *Nat. Protoc.* **8**, 1670-1679 (2013).
43 Zhang, Y. *et al.* Rapid single-step induction of functional neurons from human pluripotent stem cells. *Neuron* **78**, 785-798 (2013).
44 Yang, N. *et al.* Generation of pure GABAergic neurons by transcription factor

programming. *Nat. Methods* **14**, 621-628 (2017).
45 Rhee, H. J. *et al.* An autaptic culture system for standardized analyses of iPSC-derived human neurons. *Cell Rep.* **27**, 2212-2228. e2217 (2019).
46 Meijer, M. *et al.* A single-cell model for synaptic transmission and plasticity in human iPSC-derived neurons. *Cell Rep.* **27**, 2199-2211. e2196 (2019).
47 Ho, S. M. *et al.* Rapid Ngn2-induction of excitatory neurons from hiPSC-derived neural progenitor cells. *Methods* **101**, 113-124 (2016).
48 Song, S. *et al.* Efficient derivation of excitatory and inhibitory neurons from human pluripotent stem cells stably expressing direct reprogramming factors. *Current protocols* **1**, e141 (2021).
49 Misra, S. N., Kahlig, K. M. & George Jr, A. L. Impaired NaV1. 2 function and reduced cell surface expression in benign familial neonatal-infantile seizures. *Epilepsia* **49**, 1535-1545 (2008).
50 Tian, G.-F. *et al.* An astrocytic basis of epilepsy. *Nat. Med.* **11**, 973-981 (2005).
51 Gazina, E. V. *et al.* 'Neonatal'Nav1. 2 reduces neuronal excitability and affects seizure susceptibility and behaviour. *Human molecular genetics* **24**, 1457-1468 (2015).
52 Boiko, T. *et al.* Functional specialization of the axon initial segment by isoform-specific sodium channel targeting. *J. Neurosci.* **23**, 2306-2313 (2003).
53 Bender, K. J. & Trussell, L. O. The physiology of the axon initial segment. *Annu. Rev. Neurosci.* **35**, 249-265 (2012).
54 Kole, M. H. *et al.* Action potential generation requires a high sodium channel density in the axon initial segment. *Nat. Neurosci.* **11**, 178-186 (2008).
55 Catterall, W. A., Kalume, F. & Oakley, J. C. NaV1. 1 channels and epilepsy. *The Journal of physiology* **588**, 1849-1859 (2010).
56 Ogiwara, I. *et al.* Nav1. 1 localizes to axons of parvalbumin-positive inhibitory interneurons: a circuit basis for epileptic seizures in mice carrying an Scn1a gene mutation. *J. Neurosci.* **27**, 5903-5914 (2007).
57 Kim, H. W. *et al.* Differential effects on sodium current impairments by distinct SCN1A mutations in GABAergic neurons derived from Dravet syndrome patients. *Brain Dev.* **40**, 287-298 (2018).
58 Bak, R. O., Gomez-Ospina, N. & Porteus, M. H. Gene editing on center stage. *Trends Genet.* **34**, 600-611 (2018).
59 Barrangou, R. & Doudna, J. A. Applications of CRISPR technologies in research and beyond. *Nat. Biotechnol.* **34**, 933-941 (2016).
60 Malzahn, A., Lowder, L. & Qi, Y. Plant genome editing with TALEN and CRISPR. *Cell Biosci.* **7**, 1-18 (2017).
61 Ran, F. *et al.* Genome engineering using the CRISPR-Cas9 system. *Nat. Protoc.* **8**, 2281-2308 (2013).
62 Hendriks, D., Clevers, H. & Artegiani, B. CRISPR-Cas tools and their application in genetic engineering of human stem cells and organoids. *Cell stem cell* **27**, 705-731 (2020).
63 Ben Jehuda, R., Shemer, Y. & Binah, O. Genome editing in induced pluripotent stem cells using CRISPR/Cas9. *Stem Cell Reviews and Reports* **14**, 323-336 (2018).
64 Grobarczyk, B., Franco, B., Hanon, K. & Malgrange, B. Generation of isogenic human iPS cell line precisely corrected by genome editing using the CRISPR/Cas9 system. *Stem Cell Reviews and Reports* **11**, 774-787 (2015).
65 Bassett, A. R. Editing the genome of hiPSC with CRISPR/Cas9: disease models. *Mamm. Genome* **28**, 348-364 (2017).

66 Sherwood, C. C. *et al.* Evolution of increased glia–neuron ratios in the human frontal cortex. *Proceedings of the National Academy of Sciences* **103**, 13606-13611 (2006).
67 Azevedo, F. A. *et al.* Equal numbers of neuronal and nonneuronal cells make the human brain an isometrically scaled-up primate brain. *J. Comp. Neurol.* **513**, 532-541 (2009).
68 Von Bartheld, C. S., Bahney, J. & Herculano-Houzel, S. The search for true numbers of neurons and glial cells in the human brain: A review of 150 years of cell counting. *J. Comp. Neurol.* **524**, 3865-3895 (2016).
69 Mossink, B. *et al.* Cadherin-13 is a critical regulator of GABAergic modulation in human stem-cell-derived neuronal networks. *Mol. Psychiatry* **27**, 1-18 (2022).
70 Hämmerle, H., Egert, U., Mohr, A. & Nisch, W. Extracellular recording in neuronal networks with substrate integrated microelectrode arrays. *Biosensors and Bioelectronics* **9**, 691-696 (1994).
71 Stuart, G., Dodt, H. & Sakmann, B. Patch-clamp recordings from the soma and dendrites of neurons in brain slices using infrared video microscopy. *Pflügers Archiv* **423**, 511-518 (1993).
72 Kitamura, K., Judkewitz, B., Kano, M., Denk, W. & Häusser, M. Targeted patch-clamp recordings and single-cell electroporation of unlabeled neurons in vivo. *Nat. Methods* **5**, 61-67 (2008).
73 Margrie, T. W., Brecht, M. & Sakmann, B. In vivo, low-resistance, whole-cell recordings from neurons in the anaesthetized and awake mammalian brain. *Pflügers Archiv* **444**, 491-498 (2002).
74 Brecht, M., Schneider, M., Sakmann, B. & Margrie, T. W. Whisker movements evoked by stimulation of single pyramidal cells in rat motor cortex. *Nature* **427**, 704-710 (2004).
75 Dittgen, T. *et al.* Lentivirus-based genetic manipulations of cortical neurons and their optical and electrophysiological monitoring in vivo. *Proceedings of the National Academy of Sciences* **101**, 18206-18211 (2004).
76 Dilena, R. *et al.* Efficacy of sodium channel blockers in *SCN2A* early infantile epileptic encephalopathy. *Brain Dev.* **39**, 345-348 (2017).
77 Reynolds, E., Chadwick, D. & Galbraith, A. One drug (phenytoin) in the treatment of epilepsy. *The lancet* **307**, 923-926 (1976).
78 Ko, A. *et al.* Targeted gene panel and genotype-phenotype correlation in children with developmental and epileptic encephalopathy. *Epilepsy Res.* **141**, 48-55 (2018).
79 Chen, Y. *et al.* A versatile polypharmacology platform promotes cytoprotection and viability of human pluripotent and differentiated cells. *Nat. Methods* **18**, 528-541 (2021).
80 Sa, S., Nguyen, D. T., Pegan, J. D., Khine, M. & McCloskey, K. E. Round-bottomed Honeycomb Microwells: Embryoid body shape correlates with stem cell fate. *J. Dev. Biol. Tissue Eng* **4**, 12-22 (2012).
81 T Das, A., Tenenbaum, L. & Berkhout, B. Tet-on systems for doxycycline-inducible gene expression. *Curr. Gene Ther.* **16**, 156-167 (2016).
82 Seamon, K. & Daly, J. Forskolin: a unique diterpene activator of cyclic AMP-generating systems. *J. Cyclic Nucleotide Res.* **7**, 201-224 (1981).
83 Seamon, K. B., Padgett, W. & Daly, J. W. Forskolin: unique diterpene activator of adenylate cyclase in membranes and in intact cells. *Proceedings of the National Academy of Sciences* **78**, 3363-3367 (1981).
84 Schildge, S., Bohrer, C., Beck, K. & Schachtrup, C. Isolation and culture of mouse cortical astrocytes. *Journal of visualized experiments: JoVE* (2013).
85 Dahlmann, J. *et al.* The use of agarose microwells for scalable embryoid body formation

and cardiac differentiation of human and murine pluripotent stem cells. *Biomaterials* **34**, 2463-2471 (2013).

86 Lee, M. *et al.* Efficient exogenous DNA-free reprogramming with suicide gene vectors. *Exp. Mol. Med.* **51**, 1-12 (2019).

87 Fujii, M., Matano, M., Nanki, K. & Sato, T. Efficient genetic engineering of human intestinal organoids using electroporation. *Nat. Protoc.* **10**, 1474-1485 (2015).

88 Fridman, J. S. & Lowe, S. W. Control of apoptosis by p53. *Oncogene* **22**, 9030-9040 (2003).

89 Enache, O. M. *et al.* Cas9 activates the p53 pathway and selects for p53-inactivating mutations. *Nat. Genet.* **52**, 662-668 (2020).

90 Haapaniemi, E., Botla, S., Persson, J., Schmierer, B. & Taipale, J. CRISPR–Cas9 genome editing induces a p53-mediated DNA damage response. *Nat. Med.* **24**, 927-930 (2018).

91 Ihry, R. J. *et al.* p53 inhibits CRISPR–Cas9 engineering in human pluripotent stem cells. *Nat. Med.* **24**, 939-946 (2018).

92 Sohn, D. *et al.* Pifithrin-α protects against DNA damage-induced apoptosis downstream of mitochondria independent of p53. *Cell Death Differ.* **16**, 869-878 (2009).

93 Geisinger, J. M. & Stearns, T. CRISPR/Cas9 treatment causes extended TP53-dependent cell cycle arrest in human cells. *Nucleic Acids Res.* **48**, 9067-9081 (2020).

94 Jiang, L. *et al.* CRISPR/Cas9-induced DNA damage enriches for mutations in a p53-linked interactome: implications for CRISPR-based therapies. *Cancer Res.* **82**, 36-45 (2022).

95 Hu, Z. *et al.* Ligase IV inhibitor SCR7 enhances gene editing directed by CRISPR–Cas9 and ssODN in human cancer cells. *Cell Biosci.* **8**, 1-15 (2018).

96 Maruyama, T. *et al.* Increasing the efficiency of precise genome editing with CRISPR-Cas9 by inhibition of nonhomologous end joining. *Nat. Biotechnol.* **33**, 538-542 (2015).

97 Killian, T. *et al.* Disruption of diphthamide synthesis genes and resulting toxin resistance as a robust technology for quantifying and optimizing CRISPR/Cas9-mediated gene editing. *Sci. Rep.* **7**, 15480 (2017).

98 Ma, Y. *et al.* Increasing the efficiency of CRISPR/Cas9-mediated precise genome editing in rats by inhibiting NHEJ and using Cas9 protein. *RNA Biol.* **13**, 605-612 (2016).

99 Lepski, G., Jannes, C. E., Nikkhah, G. & Bischofberger, J. cAMP promotes the differentiation of neural progenitor cells in vitro via modulation of voltage-gated calcium channels. *Front. Cell. Neurosci.* **7**, 155 (2013).

100 Kim, H., Zahir, T., Tator, C. H. & Shoichet, M. S. Effects of dibutyryl cyclic-AMP on survival and neuronal differentiation of neural stem/progenitor cells transplanted into spinal cord injured rats. *PLoS One* **6**, e21744 (2011).

101 Deng, W., Obrocka, M., Fischer, I. & Prockop, D. J. In vitro differentiation of human marrow stromal cells into early progenitors of neural cells by conditions that increase intracellular cyclic AMP. *Biochemical and biophysical research communications* **282**, 148-152 (2001).

102 Jung, Y. J. *et al.* Characterization of extracellular spike waveforms recorded in wallaby primary visual cortex. *Front. Neurosci.* **17**, 1244952 (2023).

Abstract in Korean

SCN2A 관련 뇌전증에서 약물 탐색을 위한 환자 유래 유도 만능줄기세포 모델

SCN2A 관련 뇌전증은 *SCN2A* 유전자 돌연변이로 인해 발생하는 심각한 신경학적 질환으로, NaV1.2 전압 개폐 나트륨 채널을 암호화하는 *SCN2A* 유전자의 돌연변이가 신경세포의 과흥분성을 초래한다. 이로 인해 뇌전증, 지적 장애, 자폐 스펙트럼 장애를 포함한 다양한 신경발달 장애가 발생할 수 있다. *SCN2A* 관련 뇌전증의 병리학적 메커니즘을 이해하는 것은 표적 치료법 개발에 매우 중요하다. 본 연구에서는 환자 유래 유도 다능성 줄기세포(iPSCs)를 말초단핵 세포(PBMCs)로부터 생성하여 *SCN2A* 관련 뇌전증을 모델링하고 세포 및 분자적 특성을 조사하였다. 또한 CRISPR/Cas9 유전자 편집 기술을 활용해 *SCN2A* 돌연변이를 교정하여 돌연변이 신경세포와 교정된 신경세포 간의 생리학적 및 분자적 특성을 직접 비교할 수 있었다.

마이크로 전극 배열(MEA) 기록을 포함한 전기생리학적 분석 결과, *SCN2A* 돌연변이가 신경세포의 발사율을 유의미하게 증가시키고 네트워크 동기화에 심각한 이상을 초래한다는 것을 확인하였다. 이러한 이상은 신경세포 과흥분성의 주요 원인으로 작용한다. 환자 특이적 신경세포를 대상으로 고속 약물 스크리닝을 수행하여 나트륨 채널 차단제를 중심으로 잠재적 치료제를 탐색하였다. 실험된 화합물 중, 널리 사용되는 나트륨 채널 차단제인 페니토인(Phenytoin)이 모델을 검증하며 용량 의존적으로 과흥분성을 감소시키는 효과를 보였다. 추가적으로 평가된 5 개의 후보 화합물 중 일부는 낮은 농도에서 페니토인보다 더 우수한 효능을 나타냈다.

본 연구는 환자 유래 iPSC 모델, CRISPR/Cas9 유전자 편집, 전기생리학적 기술을 통합하여 *SCN2A* 관련 뇌전증을 연구하기 위한 강력한 플랫폼을 제시한다. 또한, 약물 스크리닝을 통하여 *SCN2A* 돌연변이에 의한 분자적 메커니즘을 표적하는 맞춤형 치료법 개발의 가능성을 확인하였다. 이러한 결과는 *SCN2A* 관련 뇌전증의 병리생리학적 이해를 심화시키는 동시에, 전임상 및 임상 환경에서의 화합물 검증을 통해 약물 내성 뇌전증에 대한 정밀 의학 발전을 촉진할 수 있는 기초를 제공한다.

핵심되는 말 : *SCN2A* 돌연변이, 뇌전증, 신경발달 장애, 유도 다능성 줄기세포 (iPSCs), CRISPR/Cas9, 유전자 편집, 나트륨 채널 차단제, 전기생리학, 약물 스크리닝, 정밀 의학